INFLUENCE OF DISCHARGE PRODUCT FORMATION ON LITHIUM-OXYGEN BATTERY PERFORMANCE

A Dissertation

Presented to the Faculty of the Graduate School

of Cornell University

in Partial Fulfillment of the Requirements for the Degree of

Doctor of Philosophy

by

Sampson Lau

May 2016

INFLUENCE OF DISCHARGE PRODUCT FORMATION ON LITHIUM-OXYGEN BATTERY PERFORMANCE

Sampson Lau, Ph.D.

Cornell University 2016

The Li–O_2 battery is a promising electrochemical energy storage platform for transportation applications due to its high theoretical specific energy of 3260 W h kg^{-1}. However, several problems must be solved before it can be developed commercially. We identify the Li–O_2 cell's most pertinent problems as those that are the direct result of the discharge product, Li_2O_2. In particular, Li_2O_2 deposits as an electrically insulating solid in the cathode, which can limit the transport of oxygen and electrons, both of which are essential for the cell's operation.

By using a combined experimental and theoretical approach, we find that oxygen transport limitations are insignificant compared to electron transport limitations. Furthermore, electron transport limitations are manifested in a complex manner, as demonstrated through a model in which Li_2O_2 nucleate and grow as discrete particles on the cathode surface. The potential drop at the end of discharge coincides with the complete coverage of the cathode surface, indicating that the overpotential gained during discharge is the kinetic overpotential of the oxygen reduction reaction rather than an ohmic overpotential through the Li_2O_2 bulk. Increasing the current density is shown to decrease the capacity by increasing the nucleation rate, leading to faster crowding of the cathode surface.

An improved understanding of Li_2O_2 formation can instruct effective strategies for improving the capacity and rechargeability of the Li–O_2 cell. Methods to improve capacity are proposed based on the general strategy of reducing the nucleation rate. With a molecular dynamics simulation, we show that solvents that coordinate with Li^+, such

as tetraglyme, can form a steric barrier against the deposition of O_2^-, the precursor to Li_2O_2. An open-structure cathode material, vapor grown carbon fiber (VGCF), is demonstrated to exhibit a high discharge capacity despite its low surface area, as indicated by the formation of Li_2O_2 particles up to 4 μm in diameter. By coupling a diffusion model to the Li_2O_2 nucleation and growth model, we show that VGCF can provide access to a greater volume of electrolyte for LiO_2 to diffuse in, which effectively reduces the rate of nucleation by reducing the rate at which the nucleating species accumulates near the surface.

The formation of Li_2O_2 particles also provides clues to the origins of capacity fade during cycling. Large Li_2O_2 particles can electronically isolate carbon particles from the cathode, thus reducing their surface area. We use electrochemical impedance spectroscopy to show that the effective capacitance of the cathode, which is proportional to its surface area, decreases as a function of the number of cycles passed. VGCF is able to resist electronic isolation, achieving both a stable reversible capacity of 630 $mAh\,g^{-1}$ and a stable capacitance value after 35 cycles. To address the rechargeability of Li_2O_2 particles that are larger than the electron transport length, we study the use of soluble redox mediators. Preliminary experiments show that the depletion of redox activity over time is a challenge that must be overcome to make redox mediators work in a practical Li–O_2 cell.

BIOGRAPHICAL SKETCH

Sampson Lau grew up in the Bronx, NY and attended The Bronx High School of Science. From 2007 to 2011, he attended The Cooper Union for the Advancement of Science and Art for undergraduate study, graduating *summa cum laude* with a bachelor's degree in Chemical Engineering. He attended the Robert Frederick Smith School of Chemical and Biomolecular Engineering at Cornell University from 2011 to 2016, and received the National Defense Science and Engineering Graduate Fellowship from the United States Department of Defense from 2012 to 2015 to support his research.

For my fellow dancers and dreamers.

ACKNOWLEDGEMENTS

First and foremost, I would like to thank my advisor, Lynden Archer, for his mentorship throughout my Ph.D. studies. When I first joined his research group, it was primarily a polymers group that had only just begun to delve into the field of batteries. Taking me as a Ph.D. student to pursue a project on lithium-air batteries, which the group had little experience in, was a risky endeavor. His confidence in my ability to figure things out on my own was what enabled this project to take shape. Despite being the only Ph.D. student in his group to work on lithium-air batteries, I was expected to keep up with other research groups that have teams of five or more working on a project at a time. Thanks to his advice—which is always strongly grounded in scientific first principles—I was able to navigate through the maze that is the lithium-air battery field and take ownership of something I can call my Ph.D. project.

Thanks to my thesis committee members, Yong Lak Joo and Jin Suntivich, for not only their guidance and feedback, but also for teaching me the foundational concepts that I use throughout my research. Most of the tools I use in the theoretical modeling part of my research can be traced back to Prof. Joo's course on mathematical methods. His feedback also offered valuable perspective, drawing his own group's experience in battery materials. Jin's course on electrochemistry provided the very building blocks for my research; without it, my Ph.D. project literally would not be the same. The nucleation and growth model had its origins as a course project, and it is thanks to Jin's advice and constructive criticisms that I was able to evolve it into a well-grounded part of my thesis.

I am grateful for the many members of the Archer group that have helped me both directly and indirectly throughout my four years here. Thanks to Shyamal Das for pioneering the metal-air battery work in the group and passing on his knowledge. Thanks to Jennifer Schaeffer for helping me get started in the lab, yet reminding me to always use my own judgment and never take lab techniques for granted. Thanks to my mentees,

Gagan Kangovi, Michelle Chen, and Charles Wan, for their assistance in the lab and for exploring avenues of this project that would otherwise be too much for one person to tackle. Gagan experimented with grafting redox-active compounds to the cathode to improve rechargeability. Michelle experimented with many aspects of the Li–O_2 cell, including redox mediators, anode protection, cathode seeding, and eventually performed the VGCF experiments that inspired the open cathode structure model and the capacity fading study. Charles revisited the concept of redox mediators and will be continuing this aspect of the project in the following year. A second opinion is always helpful in ensuring the robustness of one's research. Thus, I would like to thank everyone in the lab who helped shape some aspect of my research, either by asking me questions or answering some of my own. Special thanks goes out to my office mate, Lin Ma, who probably asked me the most questions out of anyone in the group and helped me learn much about the lithium-sulfur battery as well.

There are many others within the School of Chemical and Biomolecular Engineering who have helped with my research in some way or another. Thanks to Paulette Clancy and Jonathan Saathoff for teaching a course in molecular dynamics, which I initially took just out of curiosity, but actually enabled me to explore an unexpected part of my thesis research. The course also encouraged me to learn Python, which quickly became my new go-to programming language for developing models and analyzing experimental data. Thanks also to the members of Prof. Joo's group, who occasionally lent us coin cell parts and chemicals when we ran out.

The characterization experiments in this thesis would not be possible without the equipment and the help of the staff at the Cornell Center for Materials Research (CCMR) and the Center for Nanomaterials Engineering & Technology (CNET, formerly KAUST-CU). I would like to thank Jon Shu, Mick Thomas, and Brenda Fisher for their training and assistance. CCMR is supported through the NSF MRSEC program (DMR–1120296).

I gratefully acknowledge the U.S. Department of Defense for their financial support via the National Defense Science and Engineering Graduate (NDSEG) Fellowship. This fellowship has enabled me to independently pursue the research that I find most interesting without being dictated by a specific grant. The lithium-air battery field changes so quickly, with new problems arising and old problems becoming obsolete, that the freedom offered by this fellowship was invaluable in avoiding dead ends by carving out a unique path.

My experience at Cornell would not be complete without all the people who have made it enjoyable. First, I'd like to thank my fellow ChemEs. Much has changed since those late night homework sessions (which sometimes turn into impromptu runs to Buffalo Wild Wings) during our first semester, but despite how different our research topics are, we still manage to share struggles and triumphs in our academic journey. Thanks to those involved in ChEGSA for bringing us out of our labs once in a while to have some fun. Thanks to my ChemE Haus business partner, James Stevenson, and my fellow Hausmates for making our place the unofficial official gathering spot for ChemEs that want to chill.

I am grateful for Absolute Zero, which became much more to me than just a breakdance club. From starting as a trainee to being appointed as president, I grew more than I would've imagined as a b-boy and as a person. To the alumni and the members that came before me, thanks for helping me develop my skills. To the members I've shared my time at Cornell with, thanks for all the fun times during practice, battles, and performances, and thanks for trusting me with my leadership. A shout out also goes to the rest of the dance community at Cornell and in Ithaca. In particular, Impact, BreakFree, BASE, Greatest Common Factor, and Ground Up Crew, thanks for making these past few years as enjoyable as they have been. Thanks also to the upstate New York hip hop community; we may be spread out across a couple hundred miles, but that doesn't mean we can't still jam.

One of the great things about the Cornell experience is its unpredictability. I want to

acknowledge the groups that I spontaneously (relatively speaking) became involved in. Thanks to the Cornell Dragon Boat Club for the real-world application of fluid dynamics. Thanks to SAAGA for making me aware of the issues that affect our communities, and of course, the fun times. Thanks to the Engineering Graduate School Association; it was great working with all of you to bring the engineering graduate student community together, one free food event at a time. Thanks to the OpenLoop Alliance for reminding me why I chose my research topic in the first place. We all dream of a future with fast, clean transportation; building a Hyperloop is almost as crazy as trying to make a practical Li–O_2 battery, but every futuristic technology starts with a few people crazy enough to take an early swing at it.

Last but not least, I would like to thank my family for their unconditional love and support. Thanks to mom and dad for raising me to value my education as much as they did, yet letting me write my own definition for success. Thanks to my paternal grandmother, who always reminds me to eat well even in the midst of the most stressful parts of my studies. Thanks to my maternal grandmother (rest in power), who planted my family's roots in the great city of New York. Thanks to my brother, Vincent, for sharing your enthusiasm for science and blazing the trail just two years ahead of me through most of my educational life until high school. Thank you for lighting the way, Doctor* Lau (*the kind that helps people).

TABLE OF CONTENTS

LIST OF TABLES

LIST OF FIGURES

CHAPTER 1

INTRODUCTION

1.1 The Demand for Lightweight Energy Storage

Carbon dioxide emissions will continue to impart adverse long-term climate changes if efforts are not made to curb fossil fuel consumption.[1] However, shifting from an energy infrastructure based on fossil fuels to one based on renewable sources requires robust ways to store energy. Renewable sources, such as solar and wind, are intermittent by nature and require large-capacity energy storage in order to ensure the consistent delivery of electricity to meet demand. In addition, the utility of renewable sources in the transportation sector depends on the energy storage medium used on the vehicle itself. The continued dominance of internal combustion engine (ICE) vehicles over electric vehicles (EVs) is due mostly to the lack of an electrochemical storage system that can match the energy density of gasoline. The large share of petroleum-based energy consumed by the transportation sector in the United States, as shown in Figure 1.1, easily justifies the need for a competitively lightweight energy storage solution. Transitioning to EVs can lead to a major reduction in global CO_2 emissions, as the transportation sector accounts for 23% of it.[3] Current state of the art EVs use lithium-ion (Li-ion) batteries, which are also the dominant energy storage platform used in consumer electronic devices. At best, Li-ion batteries deliver a theoretical specific energy of approximately 500 W h kg^{-1}.[4,5] This dwarfs in comparison to the specific energy of gasoline, which is at least 25 times higher at 12 000 W h kg^{-1}.[6] Although Li-ion-based EVs are currently being produced at a modest rate, they have limited market penetration because they tend to be heavier and more expensive than their closest ICE counterparts. In particular, the weight and cost of the battery places a practical limitation on the driving range of the vehicle. Whereas nearly

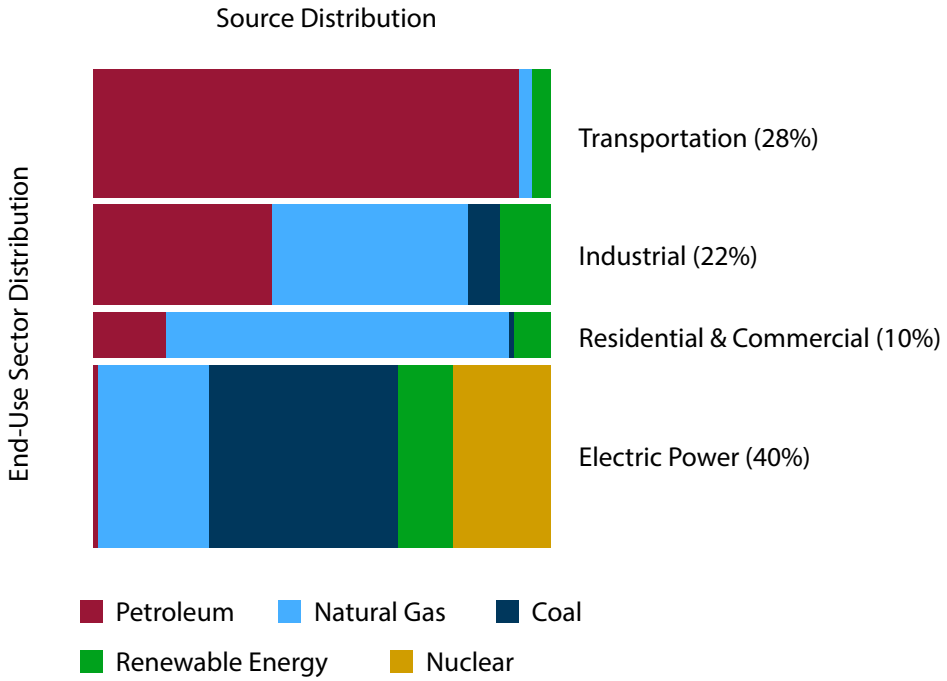

Figure 1.1: Distribution of energy usage by sector, along with the distribution of sources within each sector. The area of each rectangle relative to the whole chart represents the fraction of the total energy produced by a given source and consumed in a given sector. Data from the U.S. Energy Information Administration for the year 2012.[2]

all ICE vehicles can travel between 300 and 400 miles on a tank of gasoline, one would need to pay nearly 100,000 USD for an EV that will travel 265 miles.[7] Considering that the majority of consumers would only consider buying an electric car if it can deliver a similar range at the same price,[8] widespread adoption of EVs appear problematic without a better battery.

Recently, research groups worldwide have made it a priority to engineer practical successors to the Li-ion battery. Two decades of active research have already enabled Li-ion batteries to achieve capacities close to those theoretically allowed by the active materials.[5] To achieve higher specific energy, many research groups looked towards batteries whose chemistry is fundamentally different from that of Li-ion batteries. Traditional Li-ion batteries use intercalation electrodes which are typically LiC_6 in the anode and a transition metal oxide in the cathode. Such batteries are heavy because most of the atoms act as scaffolds that remain in place during discharge and charge. Batteries that use elemental electrodes can provide significant weight savings because all of the atoms are theoretically able to participate in the electrochemical conversion reaction. Of these batteries, only a few exhibit rechargeability, which is a trait highly desired for batteries used in EVs and consumer electronics. Figure 1.2 compares the theoretical specific energies of several rechargeable battery chemistries that have higher capacities than Li-ion. Of these chemistries, Li–O_2 (also known as lithium-air) offers the highest theoretical specific energy (3622 W h kg^{-1}) by virtue of the low atomic masses of lithium and oxygen. In fact, if one considers that electric motors are far more efficient, at ∼93%,[14,15] than internal combustion engines, at ∼30%,[16] the effective specific capacity is almost as high as that of gasoline (3260 W h kg^{-1} vs 3600 W h kg^{-1}). Having a rechargeable energy storage system competitive with gasoline opens the possibility of financially accessible EVs, which are necessary to replace the ICE vehicles that account for a substantial fraction of CO_2 emissions.

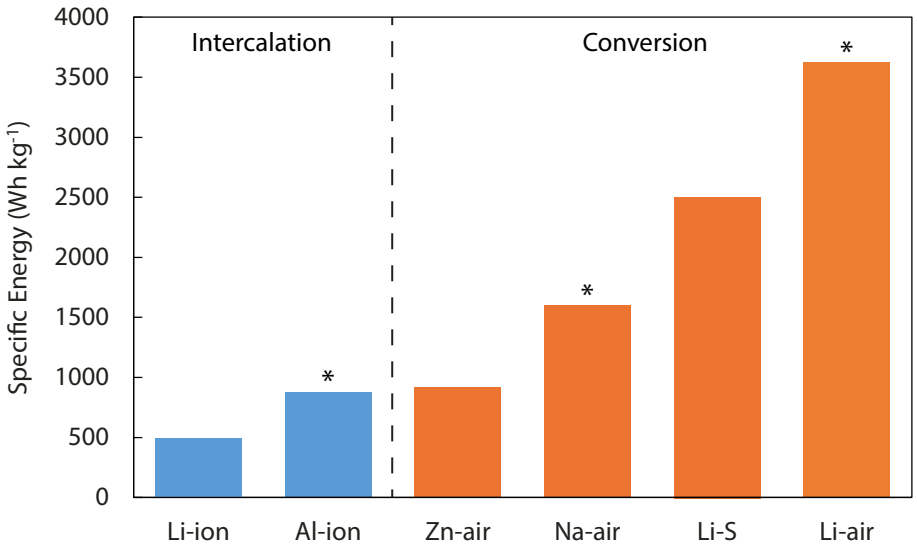

Figure 1.2: Theoretical specific energies for rechargeable battery chemistries under active research. Asterisk (*) indicates that most of the research activity is at the fundamental level. Specific energy calculated based on weight of active materials and equilibrium cell potentials from literature sources.[9–13]

1.2 State of Knowledge of Li–O_2 Batteries

Compared to other emerging battery technologies, Li–O_2 batteries are still at a relatively early stage in research. New findings on the battery's fundamental workings continue to be reported. This section intends to review the current state of knowledge of the Li–O_2 battery and lay the foundation for the work in this dissertation.

The high specific capacity of the Li–O_2 cell is mainly attributed to the simplicity of the reactants involved. The anode is composed of pure lithium metal, which ionizes during discharge to release Li^+ ions into the electrolyte.

$$Li \rightarrow Li^+ + e^- \tag{1.1}$$

The Li^+ ion travels through the electrolyte to the cathode while the electrons flow through the external circuit to power the device in use. In an aprotic electrolyte, two Li^+ ions combine with two electrons and an oxygen molecule in the cathode to form lithium peroxide (Li_2O_2), which precipitates as a solid.

$$2\,Li^+ + O_2 + 2\,e^- \rightarrow Li_2O_2 \tag{1.2}$$

A cell that operates by this chemistry is known as an aprotic Li–O_2 cell and has a theoretical potential of 3.10 V [13], enabling a specific capacity of 3622 W h kg^{-1}. Figure 1.3a shows a schematic of the aprotic cell.

If the cell contained an aqueous electrolyte instead, the water molecules act as a proton source for a different cathodic reaction, producing water-soluble lithium hydroxide (LiOH) instead.

$$4\,Li^+ + 2\,H_2O + O_2 + 4\,e^- \rightarrow LiOH \tag{1.3}$$

An aqueous Li–O_2 cell has a theoretical potential of 3.44 V,[17] enabling a specific capacity of 3850 W h kg^{-1}. Figure 1.3b shows a schematic of the aqueous cell.

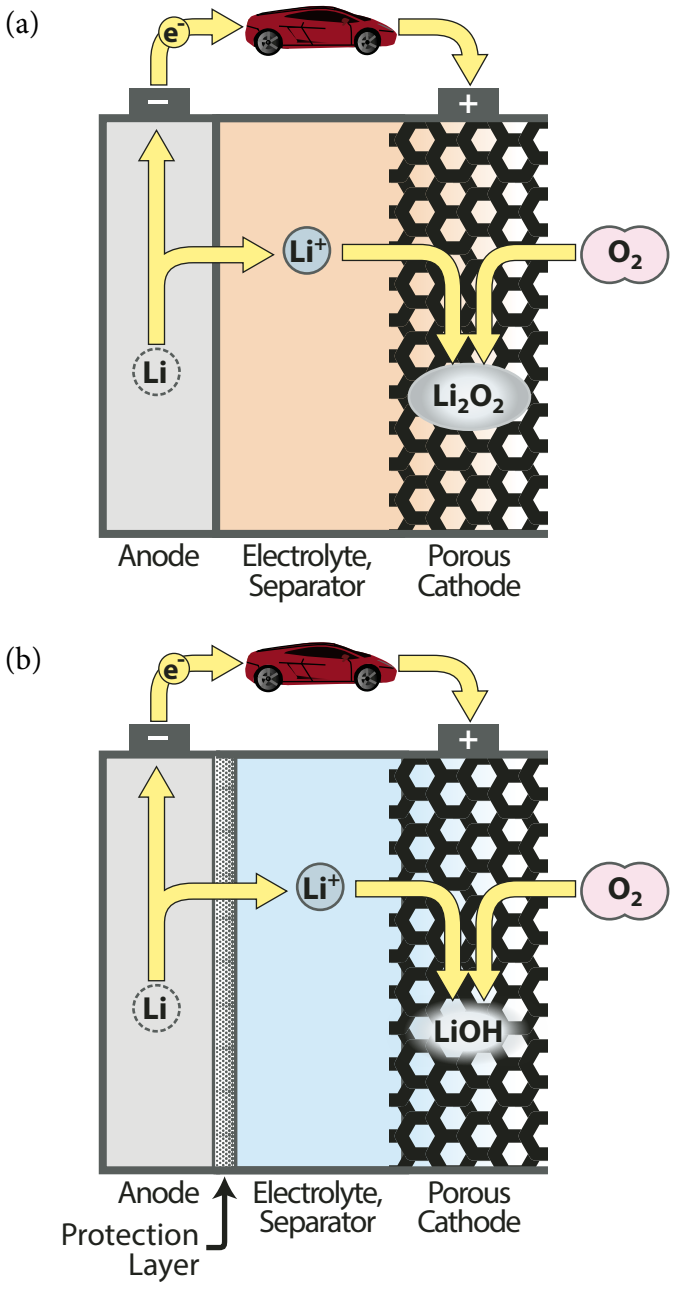

Figure 1.3: Schematics of the (a) aprotic and (b) aqueous Li–O_2 cell.

The main technical problems associated with the aqueous Li–O_2 cell are different from those associated with the aprotic Li–O_2 cell. In particular, lithium metal reacts violently with water unless it is separated by a Li+-ion conducting barrier that is impermeable to water. For this reason, most research efforts on the aqueous Li–O_2 cell are focused on developing suitable ceramic or polymer membranes for protecting the anode. Aqueous electrolytes also tend to dry quickly in systems that are open to the atmosphere, limiting the aqueous Li–O_2 cell to closed systems. These problems are not present in the aprotic cell, which allowed researchers to address the problems of reaction kinetics and cycling life more directly. Thus, the vast majority of studies on Li–O_2 cells focus on batteries of the aprotic variety. Unless otherwise indicated, the research described in this dissertation concerns the aprotic Li–O_2 cell.

The cathode reaction has been proposed to follow a few possible mechanisms that involve an oxygen reduction reaction (ORR) to superoxide radical (O_2^-) or lithium superoxide (LiO_2) as an intermediate. Two most commonly cited mechanisms in the Li–O_2 battery literature are successive reduction,[18]

$$Li^+ + e^- + O_2 \rightarrow LiO_2 \tag{1.4a}$$

$$LiO_2 + e^- + Li^+ \rightarrow Li_2O_2 \tag{1.4b}$$

and disproportionation of the superoxide,[19,20]

$$O_2 + e^- \rightarrow O_2^- \tag{1.5a}$$

$$O_2^- + Li^+ \rightarrow LiO_2 \tag{1.5b}$$

$$2\,LiO_2 \rightarrow Li_2O_2 + O_2 \tag{1.5c}$$

When the cell is recharged, Li_2O_2 decomposes back to lithium ions and oxygen by a more direct mechanism:[20]

$$Li_2O_2 \rightarrow O_2 + 2\,Li^+ + 2\,e^- \tag{1.6}$$

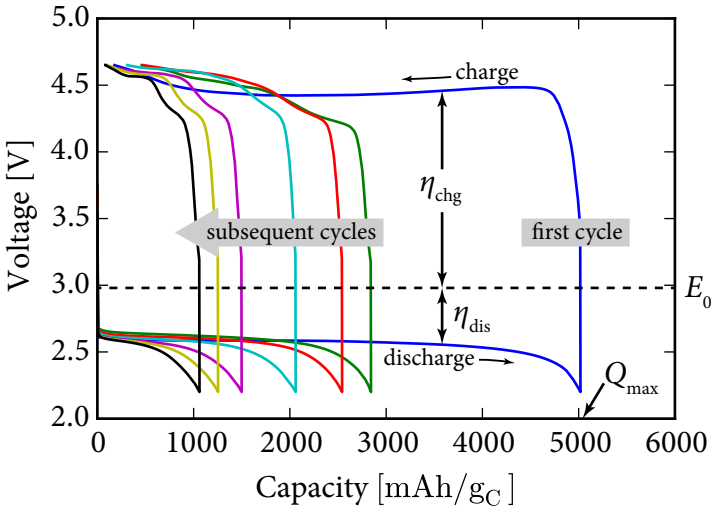

Figure 1.4: Example galvanostatic cycling curves of a Li–O_2 cell. Features to note are the equilibrium potential (E_0), the discharge overpotential (η_{dis}), the charge overpotential (η_{chg}), the discharge capacity (Q_{max}), and the capacity fade over subsequent cycles. The details of this particular test are described in Chapter 5.

Abraham and Jiang demonstrated the first rechargeable aprotic Li–O_2 battery in 1996,[13] identifying the production and decomposition of Li_2O_2 with a combination of Raman spectroscopy and a chemical assay. Since then, additional research has been sparse and were mostly focused on exploring the operating characteristics of the cell. Similar to other batteries, the cell's performance can be characterized by measuring its voltage while subjecting it to galvanostatic (constant-current) discharge and charge. The resulting plots of voltage as a function of capacity show essential performance characteristics, such as reaction voltage plateaus, overpotentials, and ability to retain capacity over multiple cycles. Figure 1.4 shows example voltage curves from a galvanostatic cycling test of a Li–O_2 cell. In a typical Li–O_2 cell with a porous carbon cathode and without any catalysts or additives, the most common issues seen are large overpotentials, a capacity that fades rapidly with cycle number, and limited current density capability.

Each component of the Li–O_2 cell plays a role in the problems that must be addressed before the Li–O_2 cell may be considered commercially viable. As with all lithium metal batteries, the anode susceptible to formation of dendrites, which are tree-like deposits of lithium that can bridge the electrodes after repeated cycling and short circuit the cell.[21] In the Li–O_2 cell in particular, oxygen can also react with the anode and create localized regions with higher interfacial resistance, which provides a mechanism for dendrite formation.[22] The electrolyte must satisfy several requirements as well. Like all batteries, the electrolyte must have a high ionic conductivity and be electrochemically stable within the cell's voltage range. However, the Li–O_2 cell also requires that the electrolyte has a high O_2 solubility and is stable against nucleophilic attack, which is a consequence of the specific mechanism by which the discharge product is formed. Most studies on the Li–O_2 battery until 2011 used carbonate-based electrolytes, which were adopted because they were commonly used in Li-ion batteries. However, subsequent work have shown that the apparent rechargeability seen in Li–O_2 cells made with carbonate-based electrolytes

was merely an artifact of electrolyte decomposition.[23–26] This is because O_2^-, formed as an intermediate species, is a strong nucleophile that can attack carbonate solvents.[25] Although this finding renders the majority of the prior literature questionable, it highlights the importance of fundamental electrochemical research on the Li–O_2 battery.

The cathode is often considered home to problems that are unique to the Li–O_2 battery because it is where Li_2O_2 formation occurs. Besides being electrochemically stable in the voltage range of the cell, the cathode must also be chemically stable towards Li_2O_2 and its superoxide precursors. In addition to having a high surface area for the ORR, the cathode must also have an open pore structure to facilitate the transport of oxygen. In most implementations of the Li–O_2 cell, the cathode is a packing of graphitic carbon particles held together by a small amount of polymer binder. The high surface area and conductivity of these carbons, combined with their low weight and cost, make them attractive as an electrode material. However, O_2^- was found to react with graphitic carbon, particularly at oxygenated defect sites,[27] and with polyvinylidene fluoride (PVDF),[28] which is a commonly-used binder. These side reactions degrade the cathode and can reduce the ability of the Li–O_2 cell to cycle.

The similarity of Li–O_2 batteries to fuel cells has encouraged the use of catalysts in the cathode. Early studies with α-MnO_2 and Co_3O_4 show that it is possible to improve the cell's discharge capacity and capacity retention over multiple cycles.[29,30] However, neither material appear to reduce the overpotential of the discharge process, which calls into question whether these compounds act as traditional electrochemical catalysts. Au was found to decrease the discharge overpotential, whereas Pt was found to decrease the charging overpotential, suggesting that Au and Pt act as ORR and OER catalysts, respectively.[31,32] Lowering overpotentials has been an active area of study because the Li–O_2 cell by itself has a poor round-trip efficiency, usually calculated as proportional to

the ratio of the discharge potential to the charge potential, meaning that the usable energy during discharge is a relatively small fraction of the energy spent during charge. The use of a combined Au and Pt catalyst, for example, was shown to improve round-trip efficiency from ~50% to ~77%.[33] However, studies employing differential electrochemical mass spectrometry (DEMS), which analyzes evolved gases *in situ*, found that certain catalysts—especially Pt—increase the production of CO_2 during charging, which could not have come from the oxidation of Li_2O_2.[34] The apparent rechargeability gained through the use of these catalysts therefore likely appears to be another result of electrolyte decomposition.

Despite the wide variety of problems mentioned thus far, the most urgent problems with Li–O_2 cells are intrinsic to the fundamental reactions of the Li–O_2 cell. In particular, Li_2O_2 forms as a solid and electronically insulating layer on the surface of the cathode. As illustrated in Figure 1.5 this can lead to two problems: (a) Li_2O_2 fills the void space within the pores, thus stopping the transport of oxygen, and (b) the electronic resistance of the Li_2O_2 layer inhibits the transport of electrons to the reaction sites at the cathode-electrolyte interface. Even if perfect materials exist to eliminate any possible side reactions, the problems intrinsic to Li_2O_2 properties still need to be addressed because Li_2O_2 is a necessary reaction product in the Li–O_2 cell.

1.3 Motivation and Scope

The motivation for the research discussed in this dissertation stems from the need for more in-depth understanding on the intrinsic problems of the Li–O_2 cell. Most of the literature on Li–O_2 batteries report on new materials and methods, or combinations of such that improve the battery's performance, but do not address how they reduce the limitations brought about by the physical properties of Li_2O_2. For example, the vast

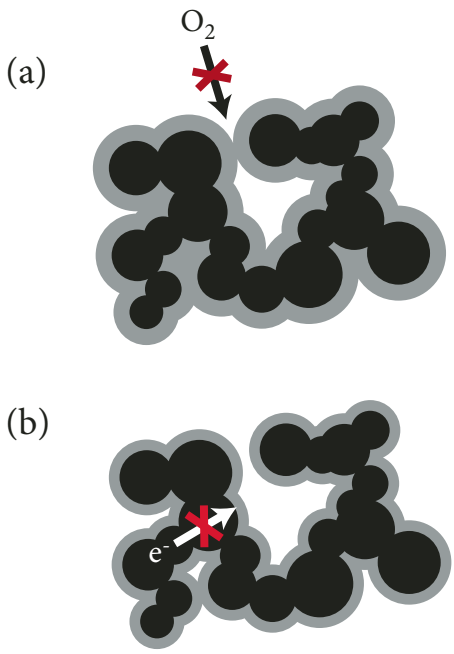

Figure 1.5: The two intrinsic problems related to the fundamental properties of Li_2O_2: (a) filling of void space can stop oxygen transport and (b) Li_2O_2 resistance can prevent oxygen transport

majority of recent studies employ a "capacity cutoff" technique, in which the Li–O_2 cell is discharged to a fixed capacity on each cycle,[35–39] because this technique was found to enable cells to operate for many more charge/discharge cycles before failure. This technique was first demonstrated by Débart et al. in 2008, who suggested that the deep polarization at the end of a traditional voltage-limited discharge is a possible indicator of the origins of capacity fade.[29] Jung et al. later popularized this technique in 2012 by demonstrating up to 100 cycles without the use of a catalyst.[37] However, this technique is neither a technological solution to the capacity fade problem nor a scientific approach to finding one. First, limiting the capacity (usually to ~50%) reduces or eliminates the primary advantage that Li–O_2 battery has over other lithium metal chemistries, such as Li–S. Second, stopping the discharge early does not allow voltage–capacity profiles to be measured at the end of each cycle, which are valuable for quantifying the rate of failure of a Li–O_2 cell. Finally, this technique prevents direct and objective comparisons of new Li–O_2 battery materials because cell testing parameters are usually chosen through trial and error to elicit the best performance out of a particular combination of materials. Despite the widespread popularity of the capacity cutoff technique, the reason behind its performance gains remains largely unexplained.

Rather than taking a trial and error approach, it is more efficient to investigate physical mechanisms to advise better design decisions for the Li–O_2 cell. Hypotheses that are often assumed to be true in the literature will need to be challenged with models that describe observable trends in better quantitative detail. For instance, oxygen transport and electronic resistance are both cited as possible causes for the rapid polarization that prevents further discharge, but it is still unclear which mechanism is dominant in the Li–O_2 cell. Furthermore, a model capable of predicting experimentally observable trends, such as voltage profiles and discharge capacities as a function of current density, has yet to be established based on one of these mechanisms. Thus, a combined modeling

and experimental approach was pursued, with a focus on relating the physical processes happening in the Li–O_2 cell to experimentally measurable trends. The goals of the present research are to (a) identify the dominant mechanism, (b) develop a model that predicts how this mechanism leads to the observed behavior, and (c) investigate strategies informed by this model to improve capacity and cycleability.

This dissertation is organized roughly in the chronology of the aforementioned goals. Since the literature most frequently cites oxygen transport as the Li–O_2 cell's capacity-limiting mechanism, the effects of oxygen transport were first examined. The experiments described in chapter 2 show that oxygen transport has a minimal effect on Li–O_2 cell capacity and voltage, and is insignificant compared to Li_2O_2 resistivity under the conditions investigated. Chapter 3 examines how Li_2O_2 resistivity limits capacity if Li_2O_2 grew nonuniformly as particles on the cathode surface. To establish this relationship, a mathematical model was developed to simulate the nucleation and growth of Li_2O_2 on the cathode. The key findings established by this model are that the growth of Li_2O_2 covers the active surface area on the cathode and that higher current density drives a higher nucleation rate that leads to quicker surface coverage. Chapter 4 applies the findings from the nucleation and growth model to explore two strategies to improve capacity. The first is selecting solvents that chelate with adsorbed lithium ions on the cathode surface to slow down nucleation, and the second is the use of an open cathode structure to reduce supersaturation of superoxide. Chapter 5 studies rechargeability and possible ways to improve it based on knowledge of Li_2O_2 growth, including the use of structurally resilient high aspect ratio cathode materials and redox mediators.

CHAPTER 2

EVALUATING OXYGEN TRANSPORT LIMITATIONS

A defining feature of the aprotic Li–O_2 cell is the overall cathodic reaction. Regardless of specific materials used in the cell, Li^+ and O_2 must be electrochemically reduced to form Li_2O_2. Since Li_2O_2 precipitates as an electronically insulating solid in aprotic electrolytes, its presence brings about intrinsic problems that limit the capacity of the cell and possibly its cycleability as well. The two most important problems are oxygen transport and electron transport, owing to the solid and electrically insulating properties of Li_2O_2, respectively. Both are commonly hypothesized as the cause of the voltage drop seen at the end of a typical discharge curve.[40–43] However, it is unclear which of the proposed capacity-limiting mechanisms is dominant due to the lack of critical experiments or theoretical studies. Historically, oxygen transport was assumed to be the dominant mechanism.[40] This chapter presents experiments designed specifically to evaluate the degree at which oxygen transport affects the performance of the Li–O_2 cell.

2.1 Background

Oxygen transport has been proposed as the primary capacity-limiting mechanism ever since a pioneering study by J. Read compared the appearance of undischarged and discharged cathodes under the scanning electron microscope (SEM).[40] The discharge product transitions from a particle-like appearance to a film-like appearance as the discharge current density increased, which suggests that the depth of penetration of oxygen may be reduced at higher current density. A follow-up theoretical study demonstrated that a significant oxygen concentration gradient can indeed develop in a cell with a 800 μm thick cathode and carbonate electrolyte.[44] However, the specific mechanism in which growth of Li_2O_2 eventually limits oxygen transport has yet to be defined. This inspired the

development of numerous models where the generation of discharge product reduces the porosity of the cathode.[41,43,45,46] Although each of these models differ in the details of their implementation, they all work on the principle that the effective diffusivity of O_2 through the porous cathode is the product of the porosity (ε) and the diffusion coefficient of O_2 dissolved in the electrolyte. In some embodiments, the tortuosity (τ) is also considered, which increases the effective diffusion length.

$$D_{O_2}^{\text{eff}} = \frac{\varepsilon D_{O_2}}{\tau} \tag{2.1}$$

The growth of Li_2O_2 can be directly mapped to the change in porosity by the molecular weight and density of Li_2O_2. In addition, every unit of O_2 corresponds stoichiometrically to one unit of Li_2O_2 produced, which allows the following relation to be derived:

$$\frac{\partial \varepsilon}{\partial t} = -\frac{R_{O_2} M_{Li_2O_2}}{V_{\max} \rho_{Li_2O_2}} \tag{2.2}$$

where R_{O_2} is the rate of generation of O_2 (negative for depletion). As the porosity approaches 0, the rate of diffusion can no longer sustain the rate at which O_2 is being electrochemically depleted. Thus, the surface concentration of O_2 decreases. This results in a decrease in the cell potential consistent with the Nernst equation:

$$E = E^0 + \frac{RT}{zF} \ln\left(\frac{c_s}{c^0}\right) \tag{2.3}$$

The reference state E^0 corresponds to the open-circuit voltage at rest, when the concentration of O_2 in the electrolyte, c_s, is constant throughout at c^0, which serves as an initial condition. During discharge, the concentration of oxygen at the electrolyte-gas interface is held constant at c^0, serving as a boundary condition.

Despite the numerous implementations of variable-porosity models in the literature, their agreement with experimental results is qualitative at best. In particular, the models tend to approximate the general shape of the experimental discharge curve, including the sudden drop in voltage at the end of discharge, but they can only be fit to discharge curves

from one or two current densities for a given set of parameters.[45,46] Furthermore, it is debatable whether the operating conditions where oxygen transport becomes a limiting factor are representative of most experiments in the literature. The models reviewed assume cathode thicknesses in the range of 700 µm to 1200 µm, but the cathode rarely exceeds 250 µm in thickness, including the thickness of the stainless steel mesh or carbon paper current collector.[47,48] The significance of oxygen transport limitations can be estimated by the Damköhler number:[45]

$$Da = \frac{j/zF}{D_{O_2}^{\text{eff}} c^0 / L} \tag{2.4}$$

which is a dimensionless ratio of O_2 depletion by the electrochemical reaction to the diffusion rate of O_2 within the electrode. A value of unity suggests that these rates are approximately equal; thus, oxygen transport limitations become significant at Damköhler numbers greater than one. The coin cell experiments described in this dissertation use an active layer thickness of 10 µm, where a geometric discharge current density of 0.1 mA cm^{-2} corresponds to a Damköhler number 0.11. (Damköhler number calculated using $D_{O2} = 2.17 \times 10^{-6}$ cm^2 s^{-1} and a Bunsen coefficient of 0.0993, which corresponds to $c^0 = 4.37$ mol m^{-3}.[44,49]) Even at low current densities, using thin electrodes there is still a significant inverse relationship between current density and discharge capacity.[50] The effects of oxygen transport, therefore, require critical evaluation in well-represented experimental conditions.

The experiments described in this chapter are motivated by discrepancies between the models and experiments in the literature. Rather than attempting to fit an oxygen transport model to experimental discharge curves, the experiments were designed such that oxygen transport properties can be derived from the voltage profiles. The first experiment directly assesses the effect of oxygen transport on the discharge capacity by introducing periodic rest periods to alleviate the limitation, if any. The second experiment essentially uses the Li–O_2 cell as an electrochemical oxygen sensor to compare the rate of diffusion of oxygen

between an undischarged and discharged cathode.

2.2 Effect of Oxygen Transport on Capacity

If oxygen transport limitations are significant in limiting the discharge capacity of the Li–O_2 cell, it would be possible to modify the operating conditions such that this limitation is reduced or eliminated. One way to do this without requiring a specially designed Li–O_2 cell is to introduce rest periods throughout the discharge process. During the rest periods, $j = 0$, $Da \to 0$, and the consumption of O_2 ceases. In the rest period, the concentration of O_2 can therefore be thought of as being given enough time to replinish.

Detailed Li–O_2 coin cell preparation protocols are described in appendix A.1-A.4; a brief summary follows. Carbon cathodes consisted of 90% Super P (Imerys Graphite & Carbon) and 10% PVDF on carbon paper (Toray TGP–030), and electrolyte consisted of 1 M $LiCF_3SO_3$ in tetraethylene glycol dimethyl ether (TEGDME). CR2032 form factor coin cells were assembled in an argon glovebox using 100 µL of electrolyte in and a Whatman GF/D glass fiber separator. All testing was performed in a custom-built oxygen-filled test chamber, maintained at a pressure of 35 kPa above atmospheric, connected to a Neware BTS–5V1mA battery tester.

The cells were allowed to rest for 6 h prior to the start of discharge to equilibrate. The cells were then discharged following a pulsed discharge scheme, where they were discharged at constant current for a period of τ_{on} and then held at open circuit for a period of τ_{off}. Figure 2.1 illustrates this discharge scheme. The cell voltage was measured during both the discharge and open-circuit periods. τ_{on} was kept at 1 min while values of 0 min (continuous discharge) to 4 min were used for τ_{off}. 4 min was considered sufficient for O_2 recovery, corresponding to $6L^2/D_{O2}$ in the event that the entire current collector thickness

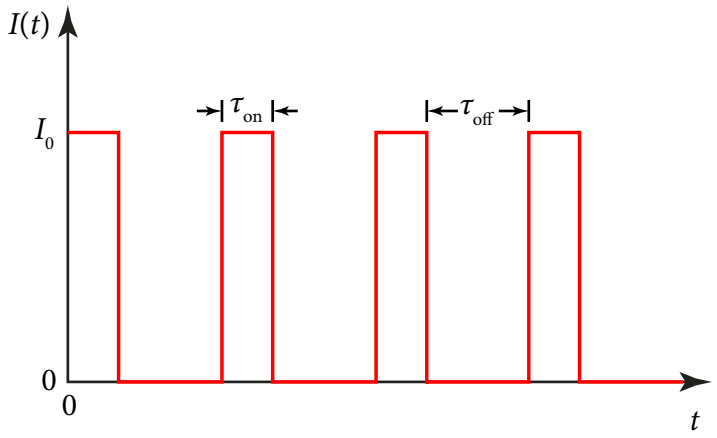

Figure 2.1: Illustration of pulsed discharge scheme. The cell discharges at I_0 for a period of τ_{on}, then rests at open circuit for a period of τ_{off}.

($L = 100\,\mu m$) is used for diffusion.

If oxygen depletion is a limiting factor and the diffusion of oxygen is significant in the time scale of τ_{off}, then this limitation should be at least partially alleviated by the introduction of rest periods. Thus, one would expect an improvement in discharge capacity and a lowered overpotential with increasing τ_{off}. However, this was not the case. Figure 2.2 shows the discharge curves obtained by splicing together the voltage measurements from the τ_{on} pulses. No significant difference in the discharge capacity was found by varying the rest time, τ_{off}. For the cells discharged at $0.025\,mA\,cm^{-2}$, the voltage curve of the continuously discharged cell is nearly identical to that of the pulse-discharged cell with $\tau_{off} = 2\,min$, and has a marginally higher capacity than the cell pulse-discharged with $\tau_{off} = 1\,min$. When the discharge current is increased to $0.1\,mA\,cm^{-2}$, the variation in discharge capacity increased, but no discernable trend is attained. Surprisingly, the continuously discharged cell produced the highest capacity, followed by τ_{off} of 2 min, 1 min, then 4 min, all within a 23% range. Considering the lack of a clear trend, it is likely that cathode loading variations ($\pm 10\%$ error by mass) are responsible for any differences in capacity.

The pulsed discharge scheme allows the resting voltage of the cell to be monitored throughout the discharge process by recording the voltage at the end of each rest period. The resting potential remains steady throughout discharge with only a slight downward slope, which indicates that the voltage polarization is able to quickly recover within the time scale of the rest period. However, increasing τ_{off} results in a systematic increase in the resting voltage, suggesting that dissolved oxygen or electrolyte ions are still in the process of equilibrating 1 min to 4 min after the discharge pulse has ended. This signals an opportunity for a more detailed and controlled study of transport in the cathode. Specifically, it is desirable to isolate the effect of oxygen diffusion on cell potential from other

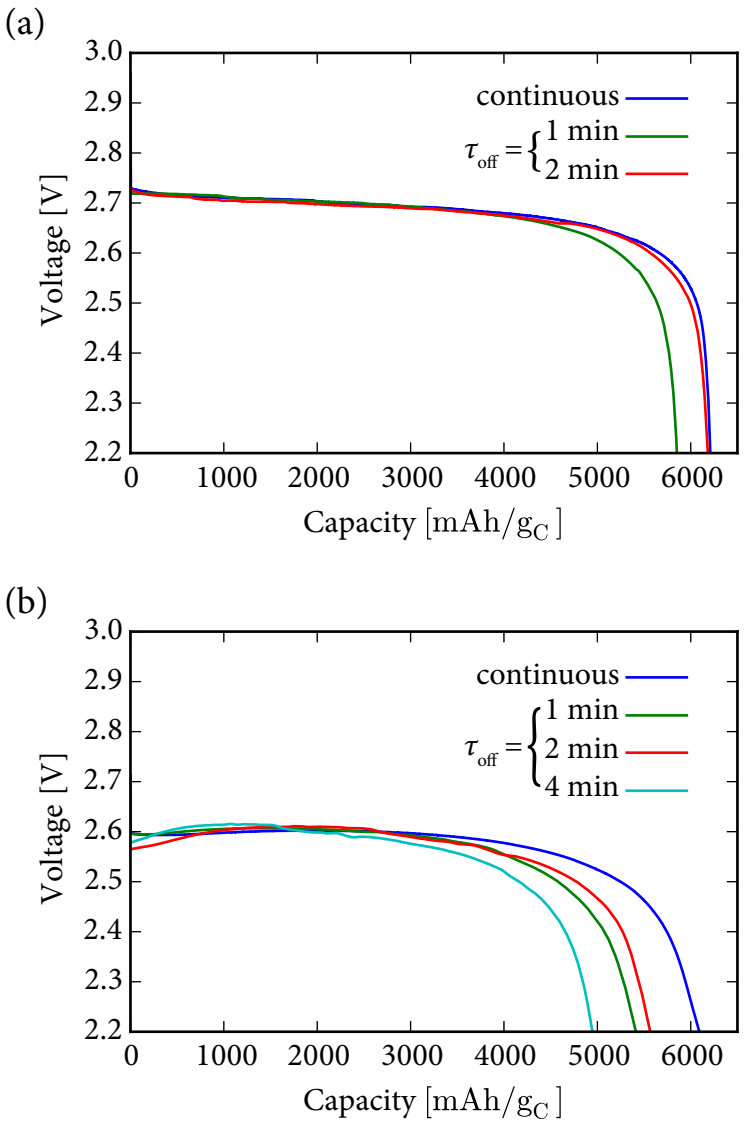

Figure 2.2: Discharge voltage curves obtained from pulsed discharged scheme, using discharge current densities of (a) 0.025 mA cm^{-2} and (b) 0.1 mA cm^{-2}.

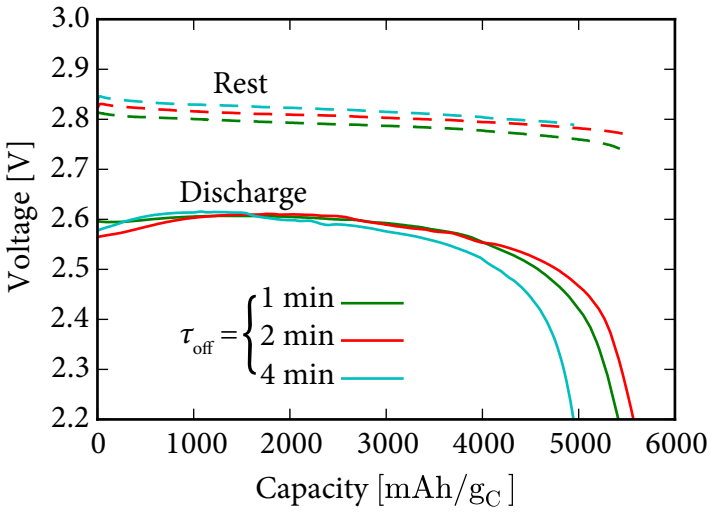

Figure 2.3: Discharge voltage (solid lines) and resting voltage (dashed lines) for different durations of rest periods.

sources such as ionic and electronic polarization, which is the premise of the following experiment described in section 2.3

2.3 Quantifying Oxygen Diffusion

The theory behind the pulsed discharge experiment is that the dissolved O_2 concentration is allowed to replenish during the resting periods. However, it is difficult to separate the effect of O_2 concentration from the effects of ionic and electronic polarization if the cell has not yet fully equilibrated from the preceding discharge step. Alternatively, the rate of oxygen diffusion could be measured with a Li–O_2 cell if it were used as an electrochemical sensor. This takes advantage of Nernst equation (eq 2.3), where the open circuit voltage would change as a function of the concentration of dissolved O_2 in the cathode. This allows the rate of oxygen diffusion to be measured independently of other transient processes, and for it to be compared between its undischarged state and its discharged state.

Coin cells used in this experiment were prepared in a manner identical to those used in the pulsed discharge experiment. The test chamber was purged with O_2, and the cells were allowed to equilibrate for 6 h. Then, the chamber was evacuated for 15 min and the cells were transferred to an argon-filled glovebox for three days in order to degas the electrolyte of dissolved O_2. The cells were returned to the testing chamber, where they were discharged to 2.2 V in an argon environment to confirm complete degassing of the cells. No measurable capacity was recorded, indicating that the remaining O_2 concentration was negligible. The chamber was then filled with O_2, and the open-circuit voltage was recorded as a function of time, which was used to derive the oxygen diffusion rate for an undischarged cell.

The same cell was then discharged to 2.2 V in an O_2 environment. The discharged

cells were degassed and returned to an argon-filled test chamber, where it was discharged at 0.1 mA cm^{-2} to 2.2 V. Once again, no measurable capacity was recorded. The chamber was then filled with O_2, and the open-circuit voltage was recorded as a function of time, which was used to derive the oxygen diffusion rate for a discharged cell.

Figure 2.4 shows the cell resting voltage, both prior to discharge and after discharge, as a function of time after the introduction of O_2 into the test chamber. Both voltages asymptotically approach equilibrium within minutes, but the discharged cell responds slightly slower, possibly due to the Li_2O_2 deposits reducing the effective diffusivity of O_2 into the cell. To quantify this difference, the voltage curves will need to be converted into oxygen concentration curves, which could be fit to a diffusion model to extract transport parameters.

For the sake of simplicity, the porous cathode will be modeled as a straight channel, similar to the model implemented by Sandhu et al.[41] When the cell is at rest, the transport of oxygen is governed simply by the diffusion equation, where the diffusivity is scaled by the porosity:

$$\frac{\partial c}{\partial t} = \varepsilon D_{O_2} \frac{\partial^2 c}{\partial x^2} \tag{2.5}$$

Two boundary conditions are implemented. At the gas-electrolyte interface ($x = L$), the concentration is held constant at c^0, while at the cathode surface ($x = 0$), a no-flux boundary applies.

$$\left.\frac{\partial c}{\partial x}\right|_{x=0} = 0 \tag{2.6}$$

$$c|_{x=L} = c^0 \tag{2.7}$$

$t = 0$ is defined as the moment at which oxygen is introduced into the test chamber. Since the cells are degassed prior to $t = 0$, the initial concentration of dissolved oxygen is zero

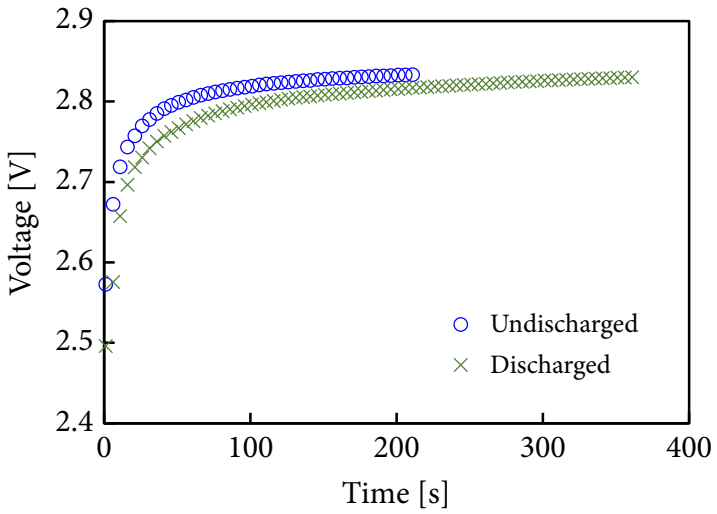

Figure 2.4: Comparison of cell potential for undischarged and discharged cell as a function of time after O_2 introduction.

throughout.

$$c|_{t=0} = 0 \tag{2.8}$$

To aid in solving for the concentration profile, eqs 2.5-2.8 were non-dimensionalized by letting

$$\tilde{c} = c/c^0 \qquad \tilde{x} = x/L \qquad \tilde{t} = t/t_c \tag{2.9}$$

where

$$t_c = L^2/(\varepsilon D_{O_2}) \tag{2.10}$$

such that the non-dimensionalized diffusion equation becomes

$$\frac{\partial \tilde{c}}{\partial \tilde{t}} = \frac{\partial^2 \tilde{c}}{\partial \tilde{x}^2} \tag{2.11}$$

with initial and boundary conditions

$$\tilde{c}|_{\tilde{t}=0} = 0 \qquad \left.\frac{\partial \tilde{c}}{\partial \tilde{x}}\right|_{\tilde{x}=0} = 0 \qquad \tilde{c}|_{\tilde{x}=1} = 1 \tag{2.12}$$

Eq 2.11 can be solved by separation of variables, leading to the following Fourier series solution:

$$\tilde{c}(\tilde{x},\tilde{t}) = -\sum_{n=1}^{\infty} \frac{2((-1)^n - 1)}{n\pi} \sin\left(n\pi\left(\frac{x}{2} + \frac{1}{2}\right)\right) \exp\left(-(n\pi)^2\tilde{t}\right) \tag{2.13}$$

Since the concentration of interest is the concentration at the cathode surface, eq 2.13 is simply evaluated at $\tilde{x} = 0$ to obtain the dimensionless surface concentration, $\tilde{c}_s$ as a function of time.

$$\tilde{c}_s(\tilde{t}) = -\sum_{n=1}^{\infty} \frac{2((-1)^n - 1)}{n\pi} \sin\left(\frac{n\pi}{2}\right) \exp\left(-(n\pi)^2\tilde{t}\right) \tag{2.14}$$

The experimental oxygen concentration at the cathode surface can be calculated from the voltage measurements in Figure 2.4 by manipulating the Nernst equation in eq 2.3, keeping in mind $\tilde{c}_s = c_s/c^0$.

$$\tilde{c}_s = \exp\left(\frac{zF}{RT}(E - E^0)\right) \tag{2.15}$$

A value of $z = 1$ was used to reflect the fact that the elementary ORR is most likely a one-electron reaction (either eq 1.4a or eq 1.5a). The equilibrium voltage, E^0, was measured as 2.84 V. The characteristic time, t_c, was optimized using the Levenberg-Marquardt algorithm (as implemented in SciPy v0.15.1) to obtain a best fit of eq 2.14 to the experimentally calculated concentrations.

Figure 2.5 shows the experimentally calculated surface concentrations as a function of time for both the undischarged and discharged case, along with the best fit curves of the diffusion model. Despite the relative simplicity of the model, it fairly captures the surface O_2 concentration transients estimated from the voltage measurements. The characteristic times were 19.6 min and 45.6 min for the undischarged and discharged case, respectively. Since the only variable in eq 2.10 that would change by discharging the cell is ε, the ratio of the characteristic times gives the relative void fraction remaining after discharge. Thus, the void fraction filled by Li_2O_2 is given by

$$\varepsilon_{\text{fill}} = 1 - \frac{\varepsilon_{\text{undischarged}}}{\varepsilon_{\text{discharged}}} = 1 - \frac{t_{c,\text{undischarged}}}{t_{c,\text{discharged}}} \tag{2.16}$$

which is estimated to be 0.57. This is markedly less than those predicted by transport-limited Li–O_2 cell models in the literature. For example, models by Sandhu et al. and Sahapatsombut et al. both predict a fill fraction of 0.93 when completely discharged at 0.1 mA cm^{-2}.[41,45] Based on the densities of Li_2O_2, bulk Super P, and graphite, the fill fraction can be independently estimated from the discharge capacity. For a cell discharged to 5.5 mAh, 2.0 µL of the available 5.2 µL is occupied, corresponding to a fill fraction of 0.39. Other reports of discharge product fill fractions also suggest that the cathode void

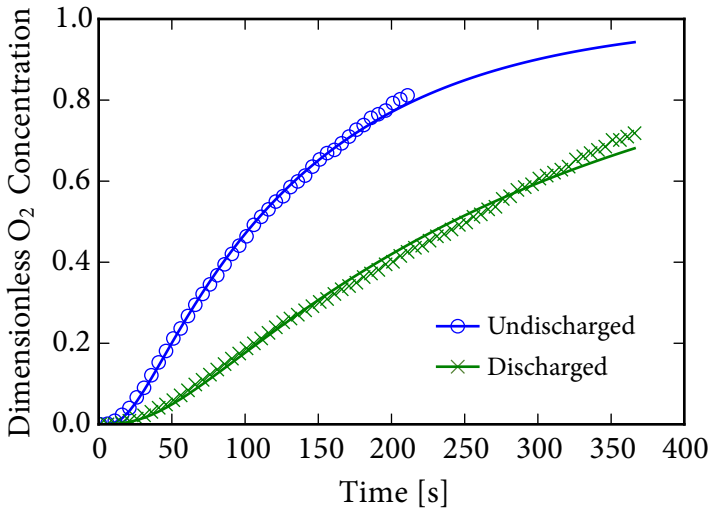

Figure 2.5: Fit of diffusion model to oxygen surface concentration calculated from cell voltage. The rate of oxygen infiltration is moderately decreased after discharge.

volume is not fully utilized as an oxygen transport-limited model would suggest. For meso- and macroporous carbon nanofoam cathodes, Li_2O_2 fill fractions range from 0.26 to 0.36, as measured with Barrett-Joyner-Halenda (BJH) analysis,[51] and for cells using carbonate electrolytes, which likely produce Li_2CO_3 instead, the fill fraction is only 0.024.[43]

Given that much of the cathode void volume is still open, additional tests can be performed to check whether oxygen transport is in fact the primary capacity-limiting mechanism. First, one can attempt to breach the supposed limiting current imposed by oxygen diffusion. Since the cathode porosity is reduced to 43% of its original value based on the oxygen infiltration experiment, the effective diffusivity (and thus the limiting current density) has been reduced by the same amount by the end of discharge. Thus, the supposed limiting current density at the start of discharge is $1/0.43$ of the original value, or $0.23\,\mathrm{mA\,cm^{-2}}$, after which the transport overpotential should reduce the cell voltage below the cutoff of 2.2 V almost instantaneously. However, a current density of $0.4\,\mathrm{mA\,cm^{-2}}$ can still produce a discharge plateau of substantial capacity above the cutoff voltage, as shown in Figure 2.6, indicating that oxygen diffusion is capable of supporting a higher current density than anticipated. Second, if the cathode pores are not completely sealed off, one could reason that some capacity should be recoverable if the cell is allowed to rest in an oxygen environment for long enough. However, Figure 2.7 shows that, even after 15 days, a second discharge attempt does not recover any significant capacity. Thus, the capacity-limiting mechanism appears to not be the depletion of oxygen, but a process with greater permanence.

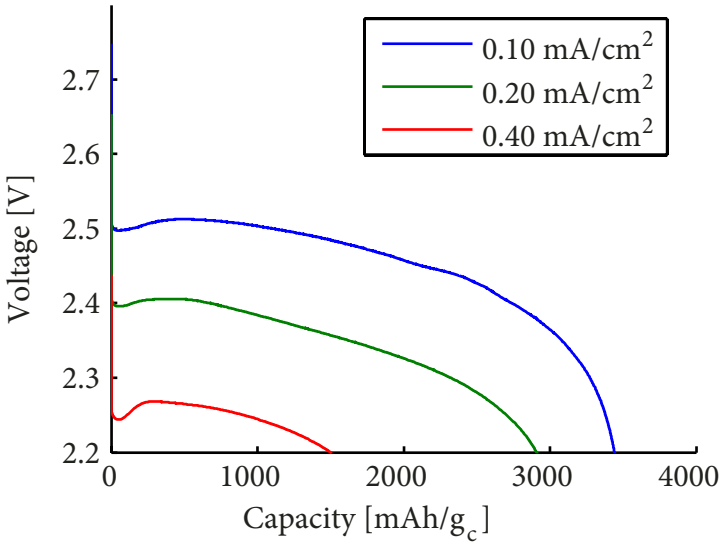

Figure 2.6: Discharge curves at higher currents (0.1 mA cm^{-2} to 0.4 mA cm^{-2}).

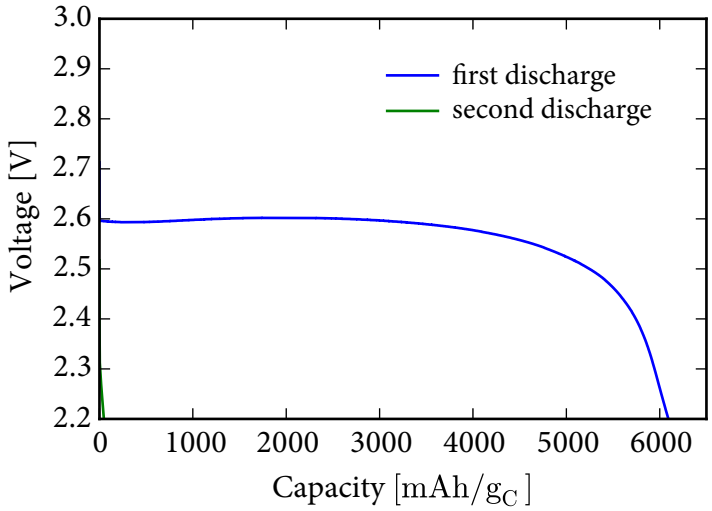

Figure 2.7: Voltage curves of first discharge and a second discharge 15 days after the end of the first discharge. A geometric current density of 0.1 mA cm^{-2} was used.

2.4 Conclusions

The experiments presented in this chapter provide evidence that the discharge of the Li–O_2 cells, as configured, is not limited by the diffusion of oxygen. First, the possibility of extending the discharge capacity by introducing rest periods in a pulsed discharge scheme was investigated. Contrary to expectations that the oxygen would freely diffuse into the pores of the cathode during the rest periods, the introduction of rest periods did not make any significant change to the discharge capacity, nor did the length of the rest periods correlate with any improvement in capacity. In an attempt to more quantitatively analyze the diffusion of oxygen through the cathode, the Li–O_2 cell was used as an electrochemical sensor as oxygen was introduced into the test chamber. This was accomplished by relating the cell voltage to the oxygen concentration with the Nernst equation, then fitting the transient concentration curves to a simple diffusion model. The diffusion model produced a good fit, but suggests that only 57% of the available void volume is occupied by Li_2O_2. An independent calculation based on molecular weights and densities suggest that the cathode is only 39% filled; both values are much lower than the 93% predicted by diffusion-limited models in the literature. Cells still produce a substantial capacity when discharged at a current density much greater than the limiting current density one would estimate for a 43% void fraction, and no significant capacity was recoverable after the initial discharge, despite the fact that the cathode void volume is far from 100% filled. These studies suggest that some other mechanism besides O_2 diffusion is responsible for limiting the discharge capacity of Li–O_2 cells observed in experiments. Most logically, the next capacity-limiting mechanism that should be examined is the electronic resistivity of Li_2O_2. When a sufficiently thick layer of Li_2O_2 is accumulated, an ohmic voltage drop would prohibit further discharge of the cell. This can occur well before the Li_2O_2 fills the pores of the cathode and limits oxygen diffusion. Albertus et al. reported the first model that concurrently simulates

both the effects of the electronic resistivity and oxygen diffusion, qualitatively showing that electronic resistivity is far more significant, at least for carbonate electrolyte cells producing Li_2CO_3.[43] Nonetheless, the effect of electronic resistivity is one that demands further consideration in models of the Li–O_2 cell.

CHAPTER 3

NUCLEATION AND GROWTH OF LITHIUM PEROXIDE

Although pioneering studies of the Li–O_2 battery popularized the hypothesis that oxygen diffusion is the capacity-limiting mechanism, they have largely ignored the possibility that the electronic resistivity of the discharge product may also prevent further discharge of the cell. In fact, it was not until 2011 that electronic resistivity was proposed as a limiting factor,[43] and one that may even take precedence over oxygen diffusion. Given the difficulty in reaching quantitative agreement between oxygen diffusion models and cell discharge experiments, electronic resistivity serves as the next most promising capacity-limiting mechanism because it is an intrinsic property of the discharge product produced by all Li–O_2 cells. The approach used in the previous chapter to analyze oxygen transport has been largely experimental, as there have been plenty of diffusion-limited models in the literature that attempt to replicate cell performance. Electronic resistivity, however, requires a different approach. Since there are no models presently available to predict cell performance metrics, such as discharge curves, from electronic resistivity, additional model development is required to create a more robust association between electronic resistivity and discharge capacity.

The main problems that need to be addressed are the disconnects between fundamental studies of Li_2O_2 resistivity and experimental observations. Much of this is qualitative: the ability of Li_2O_2 particles to grow larger than the theoretical limit imposed by Li_2O_2 resistivity has been a longstanding puzzle, and simple models of Li_2O_2 resistivity were unable to replicate the characteristic shape of the Li–O_2 cell discharge curve. The model presented in this chapter addresses these concerns by starting with an updated knowledge of the cathodic reactions, then simulating the nucleation and growth of Li_2O_2 as discrete particles rather than as a uniform layer. It is demonstrated that this approach not only

reproduces the qualitative shape of experimental discharge curve, but also quantitatively fits the capacity as a function of current density. The model demonstrates that the characteristic sharp voltage drop widely reported at the end of discharge results from the decrease in electrochemical surface area as Li_2O_2 covers the cathode surface.

Some content in this chapter was originally published in *Nano Letters*.[52] Updated methods, findings, and analyses are integrated throughout.

3.1 Background

3.1.1 Electronic Resistivity of Lithium Peroxide

It is currently believed that many of the limitations of the Li–O_2 cell stem from the unique physical properties of the discharge product. First, lithium peroxide (Li_2O_2) is insoluble in the most commonly used aprotic liquid electrolytes.[53] As a result, solid Li_2O_2 precipitates in the cathode—usually a porous carbon—leading to the blocking of oxygen transport pathways.[54] Development of a robust solution to this issue has been the goal of many cathode designs[55–58] and modeling studies.[41,44–46,59] Second, bulk Li_2O_2 has a high electrical resistivity,[42,60,61] which is hypothesized to prevent the transfer of electrons from the carbon surface to the reaction site. In models that simultaneously consider the effect of oxygen transport and electrical resistance of Li_2O_2, the latter has been found to be the more significant in limiting discharge capacity.[43]

An ongoing puzzle in the field concerns the apparent discrepancy between cell discharge experiments and fundamental studies of Li_2O_2 resistivity. Scanning electron microscope (SEM) images of discharged cells show that Li_2O_2 deposits on the cathodes in the form of particles as large as 1 μm in diameter.[40,50,57] However, density func-

tional theory (DFT) studies predict that Li_2O_2 has an electrical conductivity of only $\sim 5 \times 10^{-20}$ S cm^{-1},[62] which—to put into perspective—is less than the electrical conductivity of dry air.[63] It is possible that either electron tunneling or polaron transport may contribute towards enhancing the overall conductivity of Li_2O_2. However, electron tunneling can only support a Li_2O_2 film thickness of 5 nm to 10 nm, after which the potential drop across the Li_2O_2 film becomes sufficiently large to prevent further discharge.[42] An extension of this model that includes polaron charge transport agrees well with the gradually sloping discharge curves obtained from glassy carbon experiments,[64] but cells with high-surface-area carbon cathodes exhibit a different discharge curve shape: one that is characterized by a constant-voltage plateau followed by a precipitous, faster-than-exponential voltage drop at the end of discharge.[50,58,65] The lack of a complete model that explains both the discharge curve shape and the current–capacity relationship of high-surface-area cathodes motivates this study.

3.1.2 Solution-Phase Growth of Lithium Peroxide

Electron tunneling and polaron transport may not be sufficient to explain how Li_2O_2 particles are capable of growing to thicknesses beyond what is considered possible for an electronic insulator. The possibility of surface conductivity has been proposed,[61] but has not been validated by experiments. Alternatively, the growth of large particles of Li_2O_2 may be possible by a chemical means if one of its precursors is soluble. It was once widely assumed that LiO_2 is highly insoluble, and therefore must remain adsorbed on the surface where it was formed.[18] As a consequence, the only way for Li_2O_2 to form is by reaction scheme 1.4, where LiO_2 must be successively reduced on the surface of the electrode or on the surface of a Li_2O_2 thin enough to support electrical conductivity. However, experimental evidence began to indicate that Li_2O_2 could form spontaneously without

the transfer of charge from the electrode. Cyclic voltammetry (CV) experiments by Peng *et al.* showed that the oxidation waves, which consist of both LiO_2 and Li_2O_2 current peaks, change depending on the dwell time allotted after the reduction wave.[20] Specifically, the LiO_2 peak diminished as the Li_2O_2 peak rose, indicating that disproportionation of superoxide (reaction 1.5c) can occur spontaneously at open-circuit. This may be facilitated by surface diffusion, but another study by Black *et al.* showed that precipitation of Li_2O_2 from solution is indeed possible when LiO_2 is formed by a chemical means, indicating that LiO_2 has some limited solubility in the solvent used (TEGDME).[28]

Considering the evidence for LiO_2 solubility, a two-step solution-phase mechanism for Li_2O_2 growth may be proposed. First, LiO_2 forms through a faradaic reaction, where O_2 and Li^+ are reduced by one electron. Afterwards, LiO_2 may freely diffuse until it encounters another LiO_2 molecule, either in solution or adsorbed on the surface of the cathode or a Li_2O_2 particle, disproportionating to form Li_2O_2. Figure 3.1 illustrates this mechanism. This mechanism depends on the surfaces of Li_2O_2 particles having a greater affinity for LiO_2 than carbon surfaces do. According to DFT calculations, the adsorption of LiO_2 on Li_2O_2 may be thermodynamically favorable, since the lowest energy surface of Li_2O_2 is oxygen-rich, closer in stoichiometry to LiO_2 than it is to Li_2O_2.[61] Furthermore, formation of LiO_2 occurs through two steps in quick succession, where the first step—reduction of O_2 to O_2^- (eq 1.5a)—is known to occur by an outer sphere electron transfer,[66] and the second step—reaction with Li^+ ions (eq 1.5b)—quickly acts to stabilize the O_2^-.[20] This means LiO_2 is already in a freely diffusing state upon formation.

The possibility of solution-mediated growth continued to be a subject of debate. While some research groups have consistently seen large toroid-shaped particles of Li_2O_2 in the cathode indicative of solution-mediated growth,[37,38,50,57,67] others have only seen flat, conformal layers.[42,68] Johnson *et al.* attributed these different observations to differences

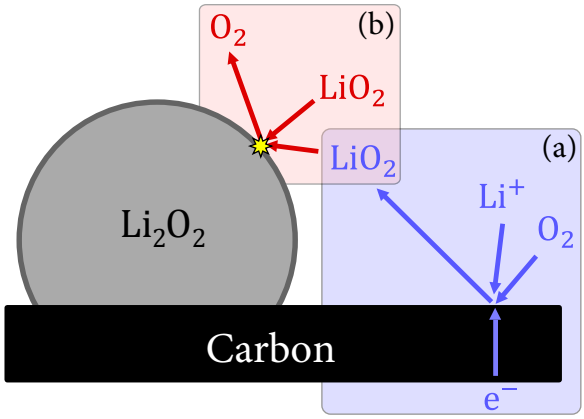

Figure 3.1: Proposed mechanism of solution-mediated growth of Li_2O_2. (a) Faradaic step, involving reduction of an oxygen molecule with one electron and one lithium ion to form lithium superoxide. (b) Two lithium superoxide molecules combine and disproportionate at the surface of a lithium peroxide particle, releasing an oxygen molecule back into the solution.

in electrolyte solvents by showing that better LiO_2 solubility enables the large toroid-shaped particles of Li_2O_2 to grow.[69] Thus, it is necessary to show that the cells used in the experiments described here follow a solution-mediated Li_2O_2 growth mechanism, as indicated by their particle morphology.

3.2 Discharge Experiments

In this work, we study the electrochemical processes in the Li–O_2 battery cathode using a combination of experiments and theory. In particular, we show that a mathematical analysis for the Li–O_2 battery cathode in which Li_2O_2 nucleates and grows as discrete nanosized particles provides a more straightforward explanation for the shape of the discharge curve. We find that the saturation of the cathode surface leads to the characteristic drop in voltage at the end of galvanostatic discharge as observed in numerous experiments. Despite its relative simplicity, the proposed model for the Li–O_2 battery cathode provides a near-quantitative description of the empirically observed discharge curves and gives guidance for designing novel electrodes and electrolytes for improving Li–O_2 battery performance.

The analysis described here require that the mechanisms proposed in the model accurately represent the experiments and vice versa. Therefore, we fabricated Li–O_2 cells with special care to minimize variations in cell construction. Details of the approach and of the testing methods employed in the study are described in Appendix A. Briefly, CR2032 coin cells were constructed with lithium foil as the anode, 1 M $LiCF_3SO_3$ in tetraethylene glycol dimethyl ether (TEGDME) as the electrolyte, and a cathode consisting of Super P carbon and 10% polyvinylidene fluoride (PVDF) binder. Water concentration in the electrolyte was confirmed to be <10 ppm with Karl Fischer titration. The cells were

discharged at constant current densities from 10 μA cm^{-2} to 100 μA cm^{-2} (normalized to geometric cathode area) within a shared, hermetically sealed oxygen chamber to ensure any impurity levels are consistent between cells. It is known that variations in cathode weight and electrolyte wetting can lead to inconsistent current density, and variations in temperature,[70] trace water,[71,72] and trace carbon dioxide[73] can lead to significant changes in specific capacity. X-ray diffraction (XRD) analysis of the discharged cathodes confirmed that Li_2O_2 was formed without any significant side products (Figure B.2).

Figure 3.2 shows post-discharge SEM images with the corresponding voltage profiles as a function of discharge capacity. Throughout the range of current densities used, the particles maintained a toroidal morphology, which is indicative of a solution-mediated growth mechanism. At least three consistent trends are apparent from the experimental results. First, increasing the discharge current density resulted in smaller Li_2O_2 particles, from ~270 nm at 10 μA cm^{-2} to ~180 nm at 100 μA cm^{-2}. Second, although the particle size decreases, the number of particles increases. This maintains the appearance of a fully covered cathode at all current densities. Third, increasing the current density causes a significant reduction of the final discharge capacity. This inverse relationship between the current density and capacity was previously abscribed to Ohmic polaron charge transport, in which the capacity is inversely proportional to the current density.[64] However, this functional relationship was found to significantly diverge from the capacities from our cell discharge experiments, as shown in Figure 3.4b. It is likely that the non-uniform deposition of Li_2O_2 on Super P carbon led to this discrepancy, since inverse proportionality is simply a corollary of Ohm's law, which requires that the Li_2O_2 deposits as a uniform film as it does on glassy carbon. Thus, non-uniform nucleation and growth was used as the basis for the model described in this work.

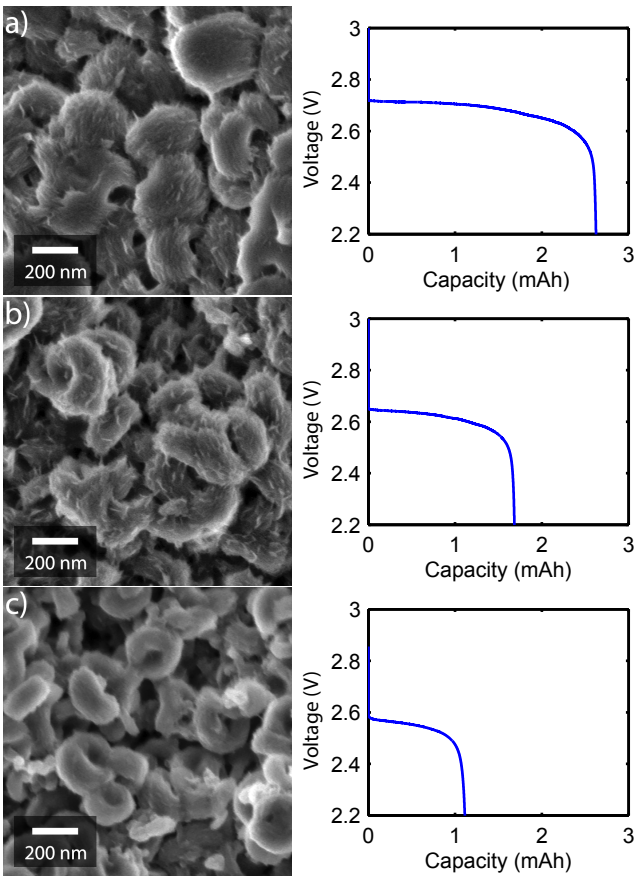

Figure 3.2: SEM images of discharged cathodes and corresponding voltage profiles of cells discharged at (a) 10 μA cm^{-2}, (b) 40 μA cm^{-2}, and (c) 100 μA cm^{-2}.

3.3 Model Development

The goal of the nucleation and growth model is to establish a mathematical connection between the non-uniform growth of Li_2O_2 and the voltage curves obtained from galvanostatic discharge tests. Previous models based on Li_2O_2 resistivity assume Li_2O_2 grows as a uniform layer on the cathode surface,[42,43,64] which is not representative of most discharge experiments of cells with high surface area carbon cathodes. With non-uniform growth, the resistivity of Li_2O_2 is expected to become significant only at the final stages of discharge, when the cathode is completely covered with Li_2O_2. At the very initial stages of discharge, the conditions leading to the initial development of a non-uniform Li_2O_2 layer were previously studied by Bazant et al.[74] Using a nanoscale continuum model for the initial stages of Li_2O_2 growth, they found that particle formation is preferred at low current density while film-like growth is preferred at high current density, which is qualitatively consistent with post-discharge SEM images. However, nucleation of particles can occur throughout the discharge process, and there has yet to be a good mathematical description for their growth. We develop a model that not only predicts these outcomes based on Li_2O_2 nucleation and growth, but does so to a quantitative degree, by combining theories from electrochemistry and phase transformation kinetics.

3.3.1 Overpotential of a Partially Passivated Cathode

We begin by considering the primary reason why uniform-growth models fail at predicting the discharge curves and capacities of experimental Li–O_2 cells that exhibit non-uniform Li_2O_2 growth. The voltage drop through a uniform layer of Li_2O_2 is well-represented by Ohm's law, which states that the electrical resistance is proportional to the layer's thickness. For a non-uniform layer, however, the local resistance changes with position. Calculating

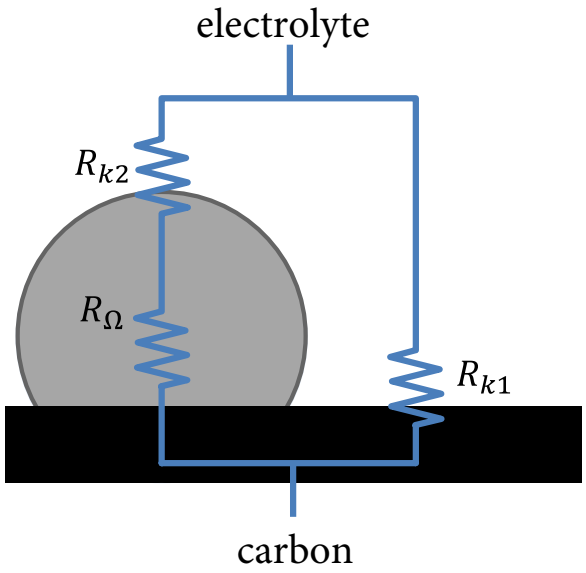

Figure 3.3: Parallel circuit analogy for a partially discharged cathode. R_{ω} is the Ohmic resistance through the Li_2O_2 bulk, while R_{k1} and R_{k2} are kinetic resistances on the uncovered carbon and Li_2O_2 surfaces, respectively. If the bulk Li_2O_2 resistance is assumed to be infinite, the overall resistance becomes equal to R_{k1}.

the voltage drop through this non-uniform layer is not straightforward, as it involves a vast grid of local resistances in parallel. To simplify this calculation, we assume that Li_2O_2 resistivity is so high, that electron transport through the particles is negligible. Thus, electron transport only occurs on parts of the cathode surface not yet covered by Li_2O_2. This could once again be illustrated as a parallel circuit, shown in Figure 3.3, where one branch goes through the Li_2O_2 bulk while the other goes through an uncovered part of the cathode. If the bulk Li_2O_2 resistance is assumed to be infinite, the overall resistance becomes equal to the kinetic resistance through the uncovered part of the carbon surface. The kinetic overpotential, in turn, may then be written using a modified Tafel equation,

$$\eta = \frac{k_B T}{e_0 \alpha} \ln\left(\frac{i}{i_0} \cdot \frac{1}{1-\theta}\right) \tag{3.1}$$

where θ is the fraction of the cathode surface covered by Li_2O_2. A key consequence of a non-uniform Li_2O_2 layer is that the overpotential is dependent on surface coverage rather than Li_2O_2 layer thickness. The coverage increases as the cell is discharged, which effectively squeezes the total current through a progressively decreasing area. Upon approaching complete coverage ($\theta \to 1$), the overpotential in eq 3.1 tends towards infinity. Obtaining a discharge curve that reflects these physics is therefore a possible from a detailed model for the nucleation and growth of Li_2O_2 that allows the coverage to be determined as a function of time.

3.3.2 Nucleation and Growth Rates

Given that the overpotential increases dramatically as the coverage approaches unity, it can be reasoned that the discharge capacity is determined by how much Li_2O_2 can be produced before it covers the entire cathode surface. From Figure 3.2, we know that that the number of Li_2O_2 particles increases with current density, but the particle size and capacity both

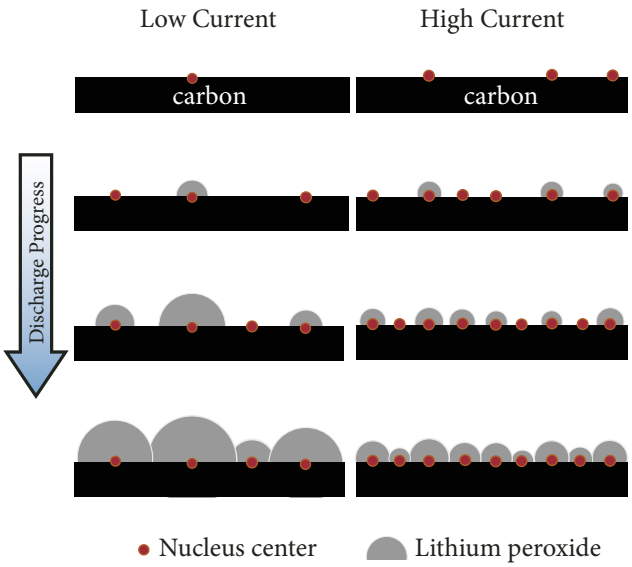

Figure 3.4: Illustration of model, showing the effect of current density on nucleation rate and the final amount of Li_2O_2 deposited.

decrease. To envision how these effects are related, Figure 3.4 compares two hypothetical cathode surfaces, where one has a higher nucleation rate as a result of being subjected to higher current density. In the high current density case, crowding due to the greater number of nuclei reduces the final size of the Li_2O_2 particles. Consequently, less Li_2O_2 is deposited, despite having the same amount of surface area as the low current density case. The final amount of Li_2O_2 deposited is directly proportional to cell's discharge capacity. Simulating the rate of nucleation is therefore an essential part of determining the capacity.

The atomistic theory of electrolytic nucleation, originally developed by Milchev et al.,[75] was adapted to model the Li_2O_2 nucleation kinetics. For a single-step nucleation process where direct deposition of the nucleating species is stable (*i.e.* a critical nucleus size of zero), the nucleation rate may be written in the form

$$J = J_0 \exp\left(\frac{\alpha e_0 \eta_0}{k_B T}\right) \tag{3.2}$$

Li_2O_2 formation, however, is known to follow a two-step reaction in which the first step is the reduction of oxygen to form LiO_2. Extending eq 3.2 to a two-step process requires an additional multiplicative term by which the concentration of LiO_2 is scaled. Furthermore, two LiO_2 molecules are required to form a Li_2O_2 nucleus, so an appropriate scaling must be included. These changes considered, the nucleation rate of Li_2O_2 becomes

$$J = J_0 \exp\left(\frac{2\alpha' e_0 \eta_0}{k_B T}\right) \exp\left(\frac{\alpha e_0 \eta}{k_B T}\right)(1-\theta) \tag{3.3}$$

The first exponential term represents the effect of overpotential on the rate of adsorption of LiO_2 molecules. A factor of 2 indicates that two LiO_2 molcules are needed to form a Li_2O_2 nucleus. α' is the nucleation rate analog of the charge transfer coefficient, which will be determined empirically by fitting the model to a series of discharge curves. η_0 is used as the effective overpotential experienced by LiO_2 from the diffuse layer, which is equal to the overpotential at the beginning of discharge. This is rationalized by the fact that molecular drift of species towards the cathode surface is constant for galvanostatic discharge. The

second exponential is identical to the Tafel equation, which governs the formation of LiO_2 molecules. α can be determined experimentally from the overpotential as a function of current density, and η is the total cathodic overpotential. e_0, k_B, and T are the electron charge, Boltzmann constant, and temperature, respectively. The pre-exponential constant, J_0, is the background rate of attachment and detachment, which can be seen as the analog to the exchange current density in the Tafel equation. This constant is given by

$$J_0 = K_{+0} c_{O_2} N_0 \exp\left(-\frac{U_0}{kT}\right) \tag{3.4}$$

where K_{+0} is a frequency factor, c_{O_2} is the concentration of oxygen in the electrolyte, N_0 is the surface concentration of active sites, and U_0 is the energy barrier to attachment.[75]

An important feature of this model is that the growth of Li_2O_2 particles is not restricted by their size, even though Li_2O_2 is a bulk ideal insulator. This is a direct consequence of LiO_2 solubility. Disproportionation of LiO_2 to Li_2O_2 is non-Faradaic, which allows the Li_2O_2 particles to grow by precipitation from solution. Indeed, while both O_2^- and LiO_2 have been observed to have some degree of solubility in stable electrolytes,[28,76] disproportionation of LiO_2 to Li_2O_2 was measured by cyclic voltammetry at room temperature to have a half life of 4 minutes,[20] which is well within the time scales assessed in our discharge experiments. Given the large size of the Li_2O_2 particles, one would expect precipitation on existing Li_2O_2 particle surfaces to contribute more towards the observed discharge capacity than precipitation on the cathode surface. Although other works may use the term "nucleation" to refer to any type of precipitation, we adopt a more specific nomenclature in this work: "nucleation" refers only to Li_2O_2–on–cathode precipitation, which creates new particles, while "growth" refers to Li_2O_2–on–Li_2O_2 precipitation, which enlarges existing particles. Unlike the nucleation rate, which depends mainly on the cathode potential as described by eq 3.3, the growth rate depends mainly on O_2^- supersaturation and the surface energy of the Li_2O_2 particles. During galvanostatic discharge, the O_2^- concentration reaches a steady state. Thus, the growth rate can be modeled by a constant

flux of Li_2O_2 at the electrolyte-facing surfaces of the Li_2O_2 particles. For simplicity, the particle shape is here taken to be hemispherical and all particles are assumed to grow at the same radial growth rate. In principle, this model does not rely on the specific shape of the Li_2O_2 particles, as long as the shape remains self-similar as it grows. The constant growth rate assumption follows from the fact that the radial growth rate for a fixed amount of Li_2O_2 precipitate scales with $1/r^2$, where r is the particle radius, while the amount of Li_2O_2 precipitated at a particle scales with r^2 due to the larger exposed surface area.

Under these assumptions, the Li_2O_2 growth rate can be derived from a simple conservation of current for a set of non-overlapping particles. However, as the coverage increases, the growth fronts begin to overlap. To account for overlap, Kolmogorov's phase transformation theory was used to relate the real volume to the "extended" volume, or the hypothetical volume of transformed material if the growth fronts did not overlap.[77] In differential form, this relationship is

$$\frac{dV_{ex}}{dt} = \frac{1}{1 - V/V_{max}} \frac{dV}{dt} \tag{3.5}$$

where V_{ex} is the extended volume, V_{max} is the maximum volume defined by the system boundaries, and V is the real volume. The extended volumetric growth rate dV_{ex}/dt is given by the sum of each individual particle's extended growth rate, which is simply the particle surface area multiplied by the radial growth rate. Since the maximum volume is defined by the surface area of the cathode, the volume fraction V/V_{max} can be approximated by the surface coverage θ. The real volumetric growth rate is simply derived from the conservation of current, where every two electrons correspond to one formula unit of Li_2O_2. Applying these relationships to eq 3.5, we arrive at an equation for the radial growth rate,

$$\frac{dr}{dt} = \frac{1}{1 - \theta} \frac{i}{2F} \left(\frac{M}{\rho} \right)_{Li_2O_2} \frac{1}{2\pi \sum_k n_j r_j^2} \tag{3.6}$$

where M and ρ are the molecular weight and density of Li_2O_2, respectively, r_j is a particular radius, and n_j is the number of particles with that radius.

To complete the analysis, we need to derive an expression for the coverage. The 2D version of Kolmogrov's phase transformation theory is sufficient for our purposes: $\theta = 1 - \exp(-\theta_{ex})$, where the extended coverage is the sum of the basal areas of all particles. The coverage is therefore given by

$$\theta = 1 - \exp\left(-\frac{\pi}{A}\sum_j n_j r_j^2\right) \tag{3.7}$$

where A is the cathode surface area. Eqs 3.1, 3.3, 3.6, and 3.7 can now be solved together numerically to simulate discharge curves. While Bazant et al.'s model can theoretically be used to estimate an initial nuclei density,[74] we considered it more reliable to obtain this value empirically because defects and impurities in the carbon cathode itself can possibly influence the initial state of discharge. In fact, DFT studies show that a defect site can have a Li_2O_2 binding energy 0.64 eV stronger than that of a perfect-graphene region,[58] which is larger than the overpotentials measured in this study. Thus, the initial nuclei density is expected to be independent of the discharge current density, and is best estimated by partially discharging the cell at a low current density to distinguish the initial nuclei (at $t = 0$) from the progressively formed nuclei (at $t > 0$). The initial nuclei density was estimated to be 2.9 nuclei μm^{-2} from SEM imaging of a cathode partially discharged at 2.5 $\mu A\ cm^{-2}$ (Figure B.3).

3.3.3 Simulation Technique

Eqs 3.1, 3.3, 3.6, and 3.7 are integrated numerically with time to simulate the nucleation and growth of Li_2O_2 and the resulting discharge curve. However, a straightforward implementation would be inefficient and inaccurate. First, keeping track of every particle

radius at every point in time requires a memory complexity of $O(n^2)$. Second, explicit numerical integration methods are not suitable for simulating the growth of the particles because the radial growth rate diverges at the very beginning of the simulation, when the total particle surface area is low. The techniques described here solves both of these challenges, allowing for a robust numerical simulation.

The memory complexity of the simulation can be reduced by considering that the radial growth rate of a particle at a given point in time is invariant of its size if the flux of LiO_2 is assumed to be constant on all Li_2O_2 surfaces. For an array of discrete timesteps, t_k, and an accompanying equal-length array denoting the number of particles nucleated at that time step, n_j, the particle radii at each time step may be stored in a two-dimensional array, r_{jk}, as all the particles that have nucleated in a particular time step are expected to share the same radius:

$$\begin{array}{cc} t_k & \begin{bmatrix} t_1 & t_2 & t_3 & \cdots & t_N \end{bmatrix} \\ r_{jk} & \begin{bmatrix} r_{11} & r_{12} & r_{13} & \cdots & r_{1N} \\ & r_{22} & r_{23} & \cdots & r_{2N} \\ & & r_{33} & \cdots & r_{3N} \\ & & & \ddots & \vdots \\ & & & & r_{NN} \end{bmatrix} \end{array} \quad \begin{array}{c} n_j \\ \begin{bmatrix} n_1 \\ n_2 \\ n_3 \\ \vdots \\ n_N \end{bmatrix} \end{array} \tag{3.8}$$

Applying the constant-flux assumption, the radial growth rate is the same for each time step for all particles, regardless of when they were nucleated, *i.e.*

$$\Delta r_N = r_{1,N+1} - r_{1,N} = r_{2,N+1} - r_{2,N} = \cdots = r_{N,N+1} - r_{N,N} \tag{3.9}$$

It then follows that all radii can be derived from the radius of the particles that nucleated at the first time step. Specifically,

$$r_{jk} = r_{1j} - r_{1k} \tag{3.10}$$

which effectively reduces the memory complexity of the simulation from $O(n^2)$ to $O(n)$, as only the first row of the matrix is required.

The second challenge is addressed by performing a segmented integration of the growth rate. First, the differential equation, eq 3.6, was discretized with respect to the time steps:

$$\frac{dr_k}{dt_k} = \frac{1}{1-\theta}\frac{i}{2F}\left(\frac{M}{\rho}\right)_{Li_2O_2}\frac{1}{2\pi\sum_{j=1}^{k} n_j r_{jk}^2} \tag{3.11}$$

Applying the relationship in eq 3.10 and integrating over the interval $t_k \in [t_N, t_{N+1}]$, we arrive at

$$\sum_{j=1}^{N} n_j \begin{pmatrix} \frac{1}{3}r_{1,N+1}^3 - r_{1,N+1}^2 r_{1,j} + r_{1,N+1} r_{1,j}^2 \\ -\frac{1}{3}r_{1,N}^3 + r_{1,N}^2 r_{1,j} - r_{1,N} r_{1,j}^2 \end{pmatrix} = \frac{1}{1-\theta}\frac{i}{2F}\left(\frac{M}{\rho}\right)_{Li_2O_2}(t_{N+1} - t_N) \tag{3.12}$$

The only unknown variable in eq 3.12 is $r_{1,N+1}$, allowing it to be solved numerically with the Newton-Raphson method.

The remaining eqs 3.1, 3.3, and 3.7 are discretized as eqs 3.13, 3.14, and 3.15and solved iteratively using the scheme shown in Figure 3.5.

$$\eta_k = \frac{k_B T}{e_0 \alpha}\ln\left(\frac{i}{i_0}\cdot\frac{1}{1-\theta_k}\right) \tag{3.13}$$

$$J_k = J_0 \exp\left(\frac{2\alpha' e_0 \eta_0}{k_B T}\right)\exp\left(\frac{\alpha e_0 \eta}{k_B T}\right)(1-\theta_k) \tag{3.14}$$

$$\theta_k = 1 - \exp\left(-\frac{\pi}{A}\sum_{j=1}^{k} n_j (r_{1j} - r_{1k})^2\right) \tag{3.15}$$

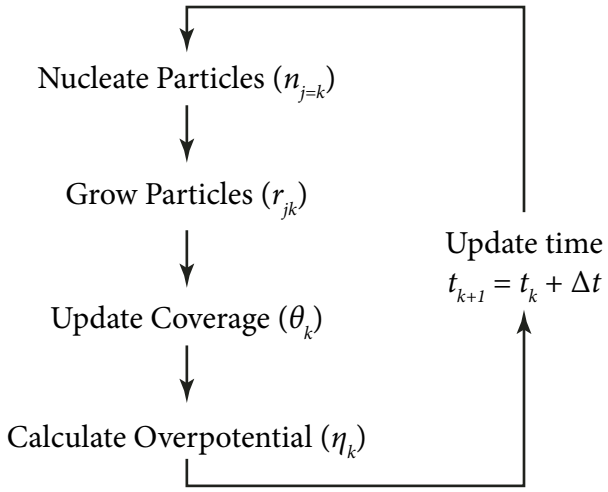

Figure 3.5: Flowchart of nucleation and growth simulation.

3.4 Analysis and Discussion

Figure 3.6a compares the simulated discharge curves obtained from the theoretical analysis to those obtained from experiments. It is apparent that the model predictions are in remarkably good accord with the experimental discharge curves. The three model parameters, α, α', and J_0, provide important insights about the cathode processes. The overall charge transfer coefficient, α, can be determined independently from an iR-corrected Tafel plot of the onset potentials (Figure B.5), as it is independent of the discharge curves. The quantity $J_0 \exp(2\alpha' e_0 \eta_0 / kT)$ was treated as an adjustable variable for each current density. α' and J_0 can then be determined by linear regression, as shown in Figure 3.6b. To verify the robustness of the model, we compare its predictions with experimental results reported by Nazar et al. in Figure B.4.[50] These experiments covered the same range of current densities used in our studies, but employed a different cathode material (XC-72/Nafion composite) and used LiTFSI as the electrolyte salt. It is apparent from the figure that the model predictions are once again in good accord with the experimentally measured discharge curves. The parameter values employed in both sets of experiments are summarized in Table 3.1.

Comparison of the parameters in Table 3.1 reveals an interesting result. In particular it is seen that α' is essentially the same for the two experiments, despite the very different cathode materials employed in our study and in the earlier study by Nazar and co-workers. The electrolyte solvent, however, is identical, which suggests that the major energy barrier to LiO_2 adsorption is the removal of the solvation shell. A more detailed study of the energy barrier to adsorption is described in the following chapter. In contrast, J_0 is almost two orders of magnitude greater for the cells made with XC-72 than for those made with Super P. J_0 is a product of several factors, as defined in eq 3.4. However, it is unlikely that differences in oxygen concentration (c_{O_2}) or the attachment frequency factor

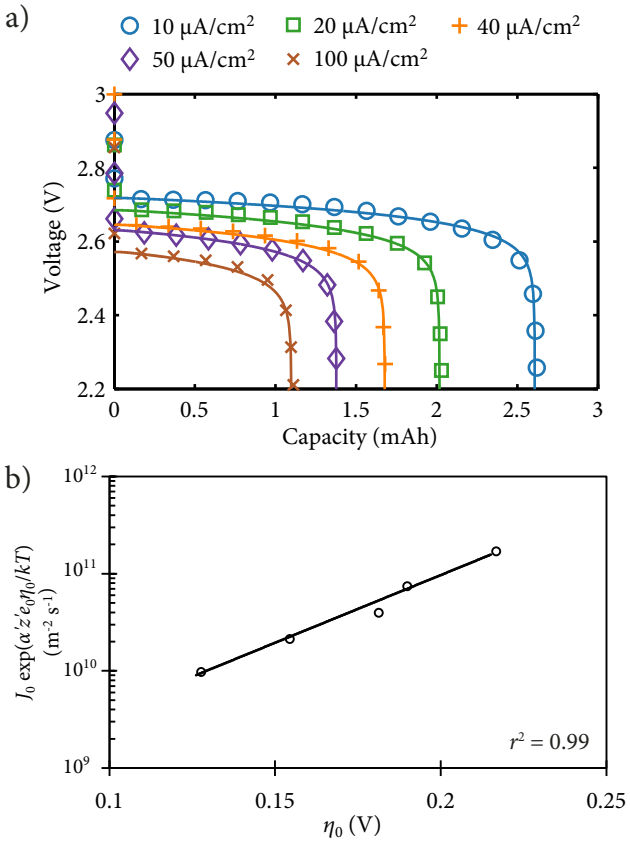

Figure 3.6: (a) Simulated (lines) and experimental (symbols) discharge curves for a Li–O_2 cell with Super P cathode. (b) Plot to obtain J_0 and α'.

Parameter	Value		Units	Description
	Super P	XC-72		
J_0	1.5×10^7	8.0×10^8	$m^{-2}\ s^{-1}$	Frequency of nuclei formation and disintegration at zero overpotential.†
α'	0.407	0.415	——	Charge transfer coefficient of superoxide adsorption.†
α	0.656	0.496	——	Charge transfer coefficient of $O_2 + e^- \rightarrow O_2^-$.‡

Table 3.1: Atomistic nucleation model parameters.
†From discharge curve fits.
‡From Tafel analysis of onset potentials.

(K_{+0}) contributed significantly to the change in J_0 because both cell types used the same electrolyte solvent with the same salt concentration and were tested under similar O_2 pressures. The remaining factors—active site density (N_0) and nucleation energy barrier (U_0)—depend primarily on the cathode material. XC-72 has a lower pH than Super P, which is an indication of a higher number of carboxylic acid functional groups. DFT calculations show that oxygen defect sites have a stronger binding interaction than a defect-free graphene surface.[58] Thus, the extra functional groups on XC-72 may act as active nucleation sites to increase N_0. Additionally, XC-72 is more hydrophillic than Super P, with a contact angle of 82° versus 95°.[78,79] This can lead to a higher surface concentration of Li^+ ions to stabilize the O_2^- upon formation, corresponding to a reduction in U_0. Both an increased N_0 and a decreased U_0 result in a higher J_0 and a higher rate of nucleation.

In addition to capturing the discharge profile in Li–O_2 cells with high-surface-area carbon, the model also directly links the Li_2O_2 growth to the cell voltage and usable capacity. Figure 3.7 compares the discharge curve to the simulated coverage and reveals that the characteristic sharp drop in voltage occurs immediately before the cathode becomes completely covered by Li_2O_2. Despite the steepness of the voltage drop, the surface coverage increases almost linearly as a function of capacity. This observation can be contrasted with previous results from uniform growth models, which are unable to replicate this sharp voltage drop seen in experiments. Thus, heterogeneous Li_2O_2 growth is evidently a key aspect of the Li–O_2 cell that cannot be omitted when modeling its performance. Instead of having the capacity limited by the thickness of the Li_2O_2 layer, a cell simulated by this model is effectively limited by the surface coverage on the cathode. When compared to a fit to Ohmic resistance through a uniform layer, the non-uniform growth model predicts the capacity as a function of current density much more closely, as shown in Figure 3.8.

Since all Li_2O_2 particle sizes are tracked within the simulation, particle size distribu-

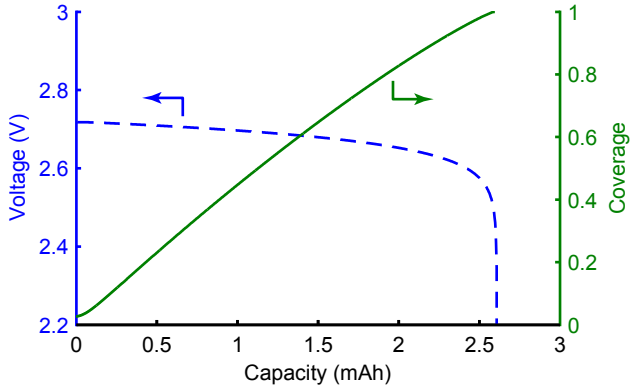

Figure 3.7: Cathode surface coverage (—) compared with cell voltage (– –) as a function of capacity discharged. (Example shown is $i = 10\,\mu\text{A cm}^{-2}$.)

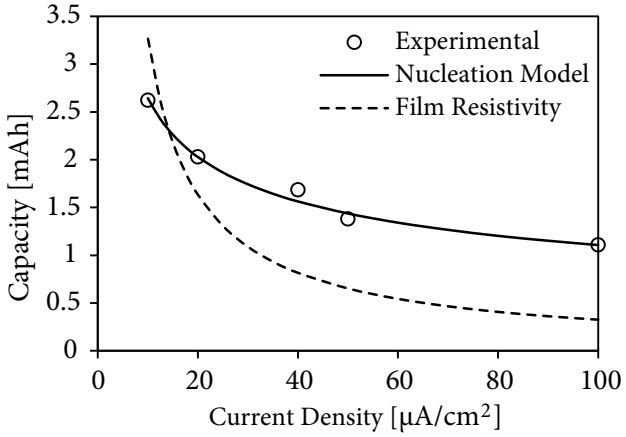

Figure 3.8: Fit of capacity as a function of current density to the non-uniform nucleation and growth model presented in this work, compared with the best obtainable fit based on the Ohmic resistance of a uniform Li_2O_2 film.

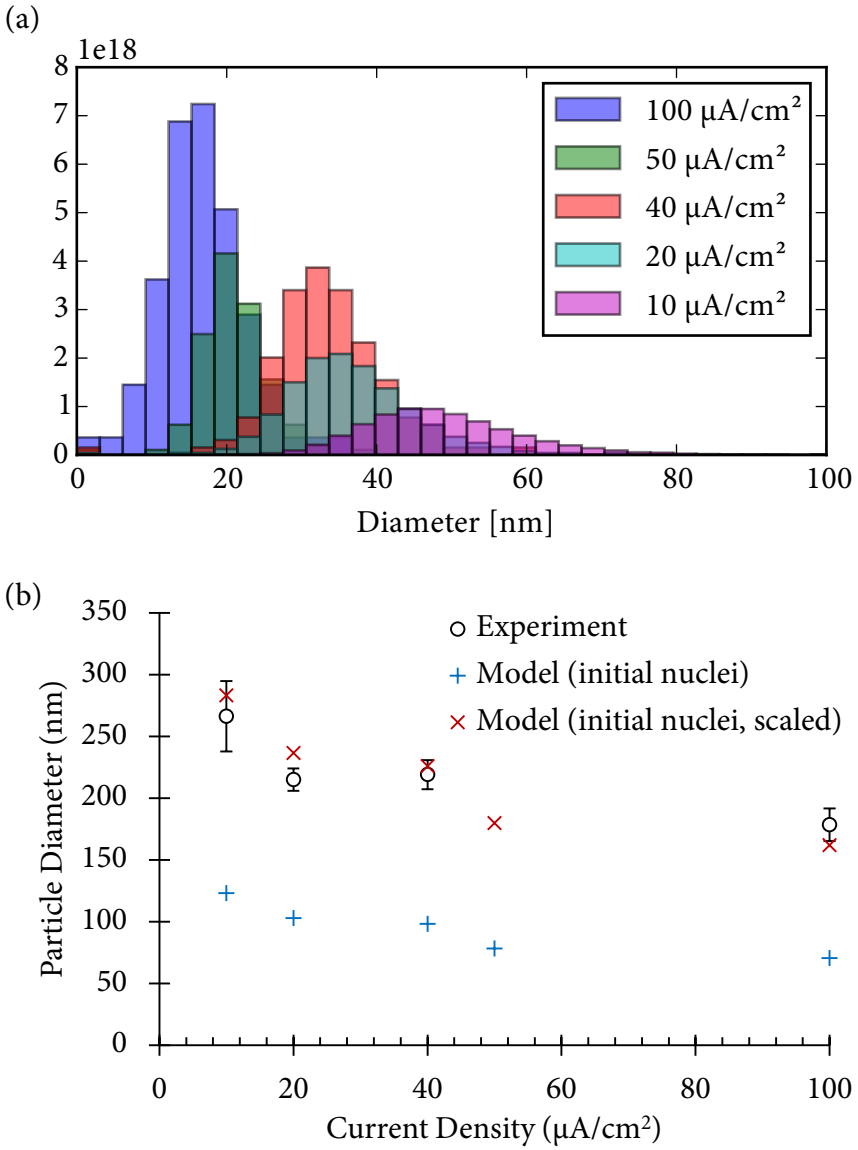

Figure 3.9: (a) Simulated Li_2O_2 particle size distributions. (b) Comparison of experimentally observed dominant particle sizes to the size of the initial nuclei in the model. A multiplicative scaling factor of 2.3 places the model's prediction within the experimental measurements, suggesting that discrepancy may be due to a difference in contact angle ($\theta_c \sim 154°$).

tions can be found as a function of discharge current density. The predicted distributions, shown in Figure 3.9a, show a familiar trend seen in the SEM images: as the current density increases, the size of the particles decreases as the number of particles increases. However, the sizes appear to be systematically lower than those seen in the SEM images. Biased sampling may have affected the measurements in the SEM images, since larger particles tend to dominate and obscure smaller particles from view. Thus, a better comparison may be made with the upper end of the predicted particle size distribution, which corresponds to the particles that nucleated at the start of the simulation. Figure 3.9b compares these diameters to their experimental counterparts from SEM images. Since Li_2O_2 particles are toroidal in shape, the experimentally-determined diameters are taken to be the average of the major and minor axes. Scaling the model-predicted diameters by a constant multiplicative factor of 2.3 brings them within the experimental values, which suggest that a difference in contact angle may be at play. Eqs 3.6 and 3.7 assume the particles are hemispherical, meaning the ratio of the particle radius to the base radius is one. In general, this ratio is a function of the contact angle (θ_c), where

$$\frac{r_{\text{particle}}}{r_{\text{base}}} = \csc^{-1} \theta_c \tag{3.16}$$

From this relationship, a scaling factor of 2.3 would correspond to a contact angle of $\theta_c \sim 154°$, which is reasonable based on the amount of curvature visible in SEM images.

Although the large particles dominate the view in the end-of-discharge SEM images, the model predicts that the capacity is contained throughout the entire size distribution. To obtain a better look at the experimental particle size distribution, coin cells were stopped at various depths of discharge and imaged *ex situ* such that the progression of Li_2O_2 particle morphology is visible. The images, shown in Figure 3.10, reveal that nucleation and growth occurs in two stages. First, a small burst of Li_2O_2 particles nucleate at the onset of discharge and grow without much additional nucleation activity. This is shown in Figure 3.10b by the presence of uniformly sized Li_2O_2 particles. About 30% into discharge, smaller Li_2O_2

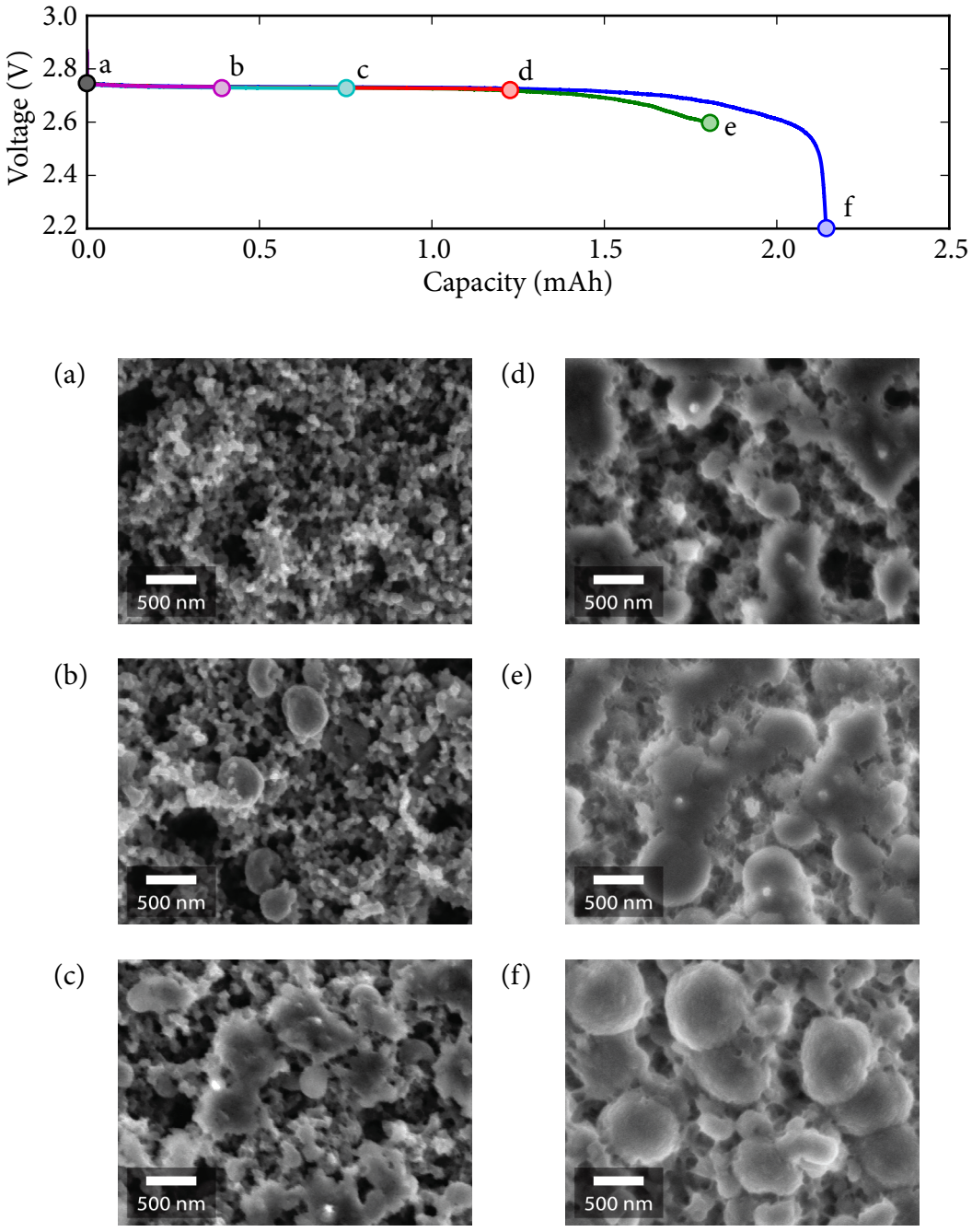

Figure 3.10: SEM images of cathodes at different depths of discharge: (a) 0 mAh, (b) 0.37 mAh, (c) 0.73 mAh, (d) 1.21 mAh, (e) 1.79 mAh, and (f) 2.14 mAh. $i = 2.5\ \mu\text{A cm}^{-2}$

particles develop as progressive nucleation commences. This is seen in Figures 3.10c-f, where smaller and less uniformily-sized particles coexist with the larger ones. Particles of all sizes continue to grow, but the large particles that nucleated at the onset of discharge dominate the image towards the end of discharge in Figure 3.10f. Given the uniform size distribution of the large particles, defects or impurities on the cathode were likely to have driven the onset nucleation event. This observation points to cathode-seeding as a possible strategy for extending capacity. Impurities, if added in modest amounts, can enhance the nucleation at the onset of discharge, therefore promoting the growth of larger Li_2O_2 clusters over those progressively nucleated later in the discharge process. One such cathode design has been reported in the literature in which silver nanoclusters are employed as preferred nucleation sites.[80] The authors found that this simultaneously increased discharge capacity and the size of the Li_2O_2 particles at the end of discharge. Addition of electrochemically inert silica nanoparticles may be expected to play a similar role in altering the size of Li_2O_2 particles and discharge capacity of Li–O_2 cells.[81]

Cathode seeding to increase discharge capacity is just one of several recent trends in the Li–O_2 field focused on increasing the cell discharge capacity to approach theoretical values. Most of these approaches appear to follow a familiar trial-and-error strategy with no apparent basis in the underlying relationship between Li_2O_2 deposition and cell capacity. For example, "hierarchical" cathode designs,[82–84] cathode surface treatments,[67,85] and use of high donor number solvents have all been advocated for improving cell capacity.[69] Significantly, the proposed model provides a unified framework that can explain all of these seemingly different approaches under one general strategy: prevent complete coverage of the cathode by Li_2O_2. Hierarchical cathode designs, for example, appear to achieve this function by altering the nucleation or growth of Li_2O_2 in such a way that it delays the coverage of the carbon surface. For example, in the nanoparticle-seeded cathodes described earlier, Li_2O_2 prefers to nucleate around the nanoparticles rather than directly

on the carbon surface, which delays the passivation of the carbon and allows the Li_2O_2 to grow larger. This strategy can even be extended by designing a cathode in which Li_2O_2 nucleates and grows on non-conductive surfaces away from the location of charge transfer. In one such implementation using $NiCo_2O_4$ nanowires, the Li_2O_2 particles grew as large as 1 μm in diameter on the tips of the nanowires while leaving the carbon surface uncovered.[82] This cathode design strategy should be further explored, as it theoretically decouples the limiting effect of Li_2O_2 coverage from the nucleation and growth process.

Cathode surface treatments have also been demonstrated to enhance the capacity of the Li–O_2 cell. For example, activated carbon cathodes treated with long-chain hydrophobic groups demonstrated a five fold increase in capacity relative to the untreated carbon.[85] The hydrophobic groups were attached by a condensation reaction with the –OH defects, presumably deactivating them as nucleation centers. Similarly, another surface treatment that selectively targets the defect sites on the carbon is the atomic layer deposition (ALD) of Al_2O_3.[67] The Li_2O_2 particle diameter after discharge was found to increase from just 200 nm in the untreated case to 1 μm in the treated case. Both treatment techniques work by covering defect sites that would have otherwise acted as active sites for nucleation. In our model, this means N_0 was decreased, which lowers the rate of nucleation and allows for a larger capacity.

Since the general strategy for improving capacity is to hinder nucleation of new Li_2O_2 particles, a preferred electrolyte should solvate the LiO_2 precursor well. Bruce et al. found that high donor number (DN) solvents work better in keeping LiO_2 in solution, specifically due to their ability to solvate the Li^+ ions.[69] Furthermore, the authors showed that a cell using a high DN solvent such as dimethyl sulfoxide (DMSO) results in both larger Li_2O_2 particles and higher discharge capacity than a cell using a low donor number solvent such as DME. The high DN solvents decrease the free energy of the solvated state, which leads

to an increase in the energy barrier of nucleation, U_0. As a consequence, fewer nucleation events happen, and larger Li_2O_2 particles are allowed to grow. The solvent's effect on Li_2O_2 nucleation is therefore an important criterion to consider, along with the usual criteria of stability, when seeking an optimal solvent for the Li–O_2 cell.

All of the approaches recommended by the proposed model favor the growth of larger Li_2O_2 particles. However, this can pose a problem during recharge because the particle sizes are much larger what is accessible with electron conduction or tunneling. Therefore, direct oxidation of Li_2O_2 by charge transfer from the cathode surface is unlikely to thoroughly decompose all of the Li_2O_2 accumulated during discharge. To obtain Li–O_2 cells that simultaneously exhibit high discharge capacity and rechargeability, it is essential that the inside-out process that occurs during Li_2O_2 growth is complemented by an outside-in mechanism for depleting the accumulated Li_2O_2 discharge product at the cathode during cell recharge. Soluble redox mediators such as those proposed by Bruce and co-workers appear to be superior among current options for overcoming this hurdle. By transferring charge across the electrolyte to the otherwise inaccessible Li_2O_2 surfaces, redox mediators such as tetrathiafulvalene[86] and iodide[87] have already been reported to assist the charging of the Li–O_2 cell. Oxidation of the redox mediator can occur on the uncovered surface area of the cathode as long as the cell has not been discharged to complete coverage. A serious problem with this approach is that redox mediators dissolved in the electrolyte will diffuse to the lithium metal anode and react. Use of a intercalated cathodes, such as $LiFePO_4$, in place of Li and a solid Li^+ -conducting separator have both been shown to be effective in preventing crossover.[86,87] However, more approaches along these lines are needed in order to take complete advantage of the guidance provided by the proposed model for improving Li–O_2 cell performance.

As with any theoretical model, the one proposed here is expected to work within

certain constraints. To our knowledge, the model most accurately reproduces experimental discharge curves at low current density (< 0.1 mA cm^{-2}) and with negligible side product formation. However, increasing the usable current density of the Li–O_2 cell is an active topic of research because the typical current density of a Li–O_2 cell is still an order of magnitude less than that of a lithium-ion cell. The proposed model may begin to diverge at higher current densities and overpotentials, where a surface reduction mechanism of Li_2O_2 formation, $LiO_2 + Li^+ + e^- \rightarrow Li_2O_2$, can become significant.[20] This would lead to a higher rate of nucleation than expected from the model. If this is the case, a second term can be added to eq 3.3 such that the nucleation rate becomes the sum of the contributions from the disproportionation mechanism and the surface reduction mechanism. The model also ignores the effect of slow oxygen diffusion, which can impose a concentration overpotential at high current density. A rough calculation for a TEGDME electrolyte, using an O_2 solubility of 4.4 mM,[44] a diffusion coefficient of 2.2×10^{-6} cm^2 s^{-1},[49] and assuming an electrode thickness of 10 μm, estimates the limiting current due to oxygen transport as 0.9 μA cm^{-2}, which is nine times the highest current density used in this study.

Charge transport across Li_2O_2 was assumed to contribute a negligible amount to the capacity under the reported experimental conditions. However, Li_2O_2 conductivity becomes important at either high current densities, in which the Li_2O_2 growth is more uniform, or elevated temperatures, in which Li_2O_2 conductivity increases due to a higher polaron concentration. A study by Tan *et al.* showed that increasing the temperature results in a an increase in Li_2O_2 particle density, a decrease in Li_2O_2 particle size, as well as an increase in discharge capacity.[88] Under the proposed model alone, the increased discharge capacity seems contradictory. The morphological trends are correctly predicted by an increase in J_0 according to eq 3.4, which leads to a higher rate of nucleation. However, the model would predict a decrease in capacity due to the faster saturation of the cathode surface.

We propose that this discrepancy arises from an increase in Li_2O_2 conductivity, which allows the Li_2O_2 layer to grow perpendicularly from the cathode surface past the point of surface saturation. Indeed, a study by Das *et al.* using an ionic-liquid electrolyte, which leads to conformal layers of Li_2O_2, was found to simultaneously increase the discharge capacity and the thickness of the Li_2O_2 layer.[70]

Finally, minimizing side reactions is an ongoing challenge of the Li–O_2 cell. Although XRD measurements (Figure B.2) show no significant side products after a single discharge, side products can accumulate after several cycles.[89] The type of deviations from the discharge curve predicted by this model will depend on the particular side reactions. If the side reactions reduce the active surface area for charge transfer, either by the formation of irreversibly passivating side products or by the decomposition of conductive bridges within the cathode, the effect on the discharge curve will be similar to that caused by an increase in current density. Side reactions can also manifest as an increase in the transport overpotential if the electrolyte decomposes, if the electrolyte accumulates side products, or if the lithium anode undergoes side reactions. Using this model in future studies to analyze extensively cycled cells can help identify which types of side reactions are most significant.

In summary, we have employed a combination of experiment and theory to study a model for the nucleation and growth of Li_2O_2 in the Li–O_2 cathode. Using a combination of the atomistic nucleation theory and Kolmogorov's phase transformation theory, the proposed model is shown to provide an excellent description of the discharge profile obtained experimentally for Li–O_2 cells at low current density. The characteristic sharp voltage drop at the end of the discharge curve is shown to be caused by an increased kinetic overpotential due to Li_2O_2 covering up the available surface area for LiO_2 intermediate formation, rather than an ohmic overpotential due to electron transfer through the Li_2O_2

itself. This view is consistent with the current understanding of the Li_2O_2 formation mechanism as determined by experiments. Our analysis also highlights the importance of preventing surface nucleation of Li_2O_2 as a unified strategy for increasing Li–O_2 discharge capacity. Hierarchical cathode designs, surface treatments, and high DN electrolyte solvents are amongst the techniques that fall under this general strategy according to our model. As fundamental knowledge of the Li–O_2 battery improves, models such as that proposed on the current work become essential in identifying meaningful strategies such that we can efficiently direct our experimental efforts toward them.

CHAPTER 4

STRATEGIES TO IMPROVE CAPACITY

An overall strategy for improving capacity as suggested by the model introduced in Chapter 3 is to nucleate fewer particles on the cathode surface. The methods suggested in the literature generally accomplish this by a thermodynamic means. For example, high donor number solvents,[69] high acceptor number electrolyte additives,[72] and cathode surface treatments[67,85] all act by making the solvated state more energetically favorable relative to the surface-adsorbed state. However, the thermodynamic equilibrium still needs to be balanced in favor of Li_2O_2 formation for a practical Li–O_2 cell. Therefore, one should expect kinetic methods of slowing down nucleation to work just as well.

This chapter explores two potential methods for improving cell capacity by kinetically slowing down Li_2O_2 nucleation. First, the origins of the energy barrier to LiO_2 deposition on a carbon electrode is studied with molecular dynamics. This study was inspired by the observation that cells with TEGDME as an electrolyte solvent produces high capacities, despite its relatively low donor number. We find that TEGDME molecules chelate with adsorbed lithium ions on the cathode surface, essentially creating a barrier of adsorbed solvent molecules in which O_2^- must penetrate in order to adsorb and react. Second, the effects of an open cathode structure on discharge capacity are studied both experimentally with vapor grown carbon fiber (VGCF) cathodes and theoretically. It was found that an open cathode structure in which LiO_2 is able to freely diffuse into the electrolyte bulk can limit the nucleation rate by slowing the accumulation of LiO_2. As a result, increasing the discharge current density has a less negative impact on discharge capacity of cells that use

VGCF cathodes, in comparison to those that use Super P carbon.

4.1 Kinetic Barrier to LiO_2 Deposition

The motivation for this work stems from the large variations in Li–O_2 cell capacity that can be achieved by changing the electrolyte. Specifically, the solvents that are expected to be good solvents of the LiO_2 intermediate have been shown to extend the discharge curve to higher capacity.[69] The current hypothesis is that good solvents reduce the rate of LiO_2 deposition on the cathode surface, therefore allowing larger particles of Li_2O_2 to grow, resulting in a higher capacity. Besides thermodynamic correlations, little is known about the mechanism in which the solvent influences the rate of nucleation. Our goal is to provide more detailed insight by simulating the LiO_2 deposition process at a molecular level and calculating the free energy barriers associated with it.

We consider two open questions regarding the relationship between the electrolyte solvent and the kinetics of LiO_2 deposition in the Li–O_2 battery cathode using a series of potential of mean force (PMF) calculations. First, the ability of tetraethylene glycol dimethyl ether (TEGDME) to solvate LiO_2 was investigated, because it exhibits the qualities of a good solvent for LiO_2 but has a low donor number. The calculated PMF showed a symmetric energy barrier between the unsolvated and solvated states, indicating that neither is significantly favored over the other. TEGDME was found to solvate LiO_2 by coordinating its oxygen atoms around the Li^+ ion, consistent with other simulations in the literature, which suggest a coordination number of 3–4 per TEGDME molecule.[90,91] Second, the origin of the energy barrier for LiO_2 deposition was investigated. It was found that the energy barrier for deposition on graphene is only 0.74 kcal mol^{-1}. However, applying a small $-\frac{1}{6}e$ per carbon charge to the cathode surface increased this energy barrier to 2.29 kcal mol^{-1}. This increase is accompanied by the appearance of an immobilized

layer of solvent molecules that are tightly coordinated with the Li^+ ions adsorbed on the cathode surface.

4.1.1 Simulation Methods

Molecular dynamics simulations were performed using LAMMPS*.[92] The initial states of the simulations were prepared in stages. A tetraethylene glycol dimethyl ether (TEGDME) molecule was created and geometrically optimized in Avogadro.[93] The hydrogen atoms were deleted in place to create a united-atom representation of the molecule, and the atomic coordinates were fed into PackMol to fill a 40 Å cubic simulation box.[94] The scikit-nano Python toolkit was used to generate a 1 nm by 1 nm graphene bilayer to represent the cathode surface. The atomic coordinates of the graphene, lithium ions, and superoxide were manually appended, and any solvent molecules that overlapped within 1.9 Å of the non-solvent molecules were deleted.

The OPLS force field was used for the simulations, with united-atom (OPLS-UA) parameters for the TEGDME atoms and all-atom (OPLS-AA) parameters for the other atoms. Parameter values were borrowed from those distributed in TINKER, with a few exceptions. Lennard-Jones parameters for the graphene carbons ($\sigma = 3.39$ Å and $\varepsilon = 6.36\,\mathrm{kcal\,mol^{-1}}$) were obtained from Popova *et al.*,[95] superoxide bond-stretching parameters ($K = 888.0\,\mathrm{kcal\,mol^{-1}\,Å^{-2}}$ and $r_0 = 1.28$ Å) were obtained from Creighton *et al.*,[96] and Lennard-Jones parameters for the superoxide oxygens were approximated by those for carboxylate oxygen. An energy minimization was performed prior to the simulation runs. Two isothermal-isobaric (NPT ensemble) simulation runs were performed in sequence: the first with a time-step of 2 fs for 80 ps to allow the system to reach equilibrium, and the second with a time-step of 1 fs for 50 ps, which provided the

*`http://lammps.sandia.gov`

information for the force and energy calculations.

Three sets of simulations were performed to understand the origin of activation barriers in the Li–O_2 battery cathode: (1) the solvation of lithium superoxide, (2) the deposition of superoxide on a neutral graphene surface, and (3) the deposition of superoxide on a charged graphene surface. To simulate the solvation of lithium superoxide, a lithium ion (Li^+) and a superoxide anion (O_2^-) were held at fixed separation distances from 2.0 Å to 10.0 Å at 0.25 Å increments and the force-distance profile along the separation axis was calculated. For the deposition of superoxide on neutral graphene, the superoxide was held at the same set of separation distances along a path perpendicular to the plane of the graphene. The deposition of superoxide on charged graphene was simulated in a similar way, except partial charges were applied to the top layer (the layer facing the superoxide). Li^+ ions were also initialized 1 Å above this layer to represent the Stern layer, placed according to the crystal structure of lithium-adsorbed graphene (LiC_6).[97]

For all three sets of simulations, the average net force on the O_2^- molecule was integrated along the axis of separation to obtain the potential of mean force (PMF) using the trapezoidal rule. Errors were estimated for each simulation by a block-averaging analysis.[98]

4.1.2 Results and Discussion

Solvation of Lithium Superoxide

Lithium superoxide is believed to partially dissociate in some electrolyte solvents to its ionic constituents in the following equilibrium equation: $LiO_2 \leftrightarrow Li^+ + O_2^-$.[69,72] The amount of solvated O_2^- detected in rotating ring-disk electrode experiments was found

(a)

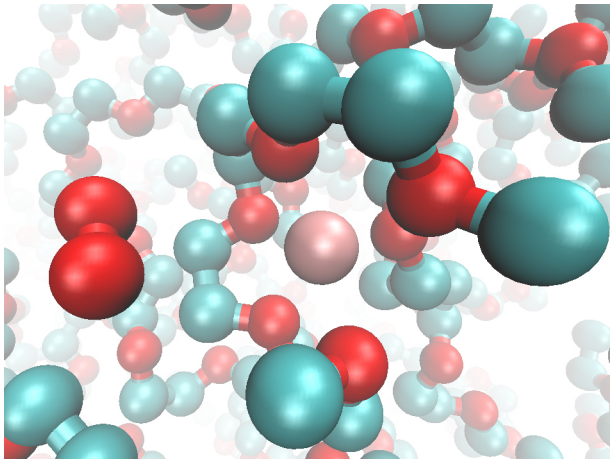

(b)

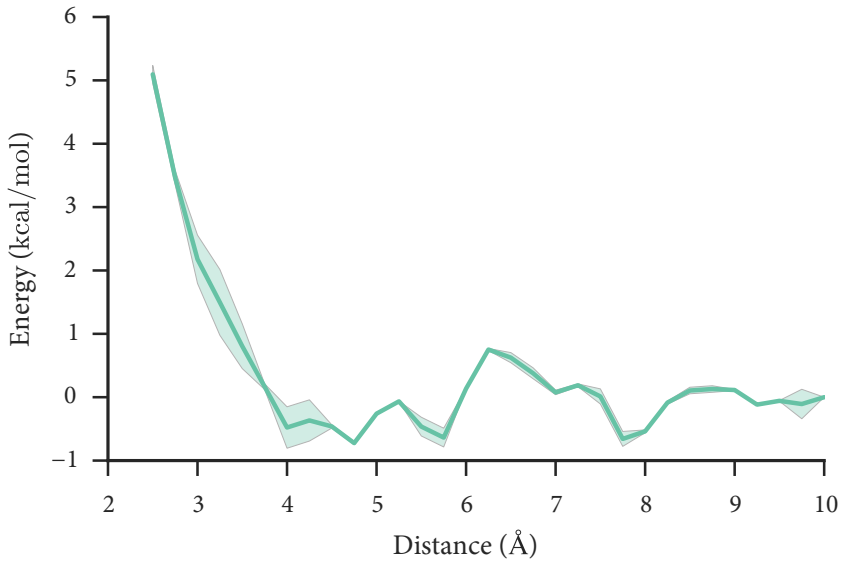

Figure 4.1: (a) Visualization of simulation at a separation distance of 4.0 Å, showing coordination of Li^+ with TEGDME molecule. Red = O, salmon = Li, teal = CH_2 and CH_3 united atoms. (b) PMF free energy with respect to Li^+ and $O_2{}^-$ separation distance. Shading represents error.

to be positively correlated with the solvent's donor number (DN),[69] which is a measure of the solvent's ability to solvate cations. High-DN solvents, such as dimethyl sulfoxide (DN = 30), were also found to result in higher discharge capacity and the formation of large toroid-shaped Li_2O_2 deposits, presumably because Li_2O_2 formation no longer requires electronic conduction if it can precipitate from a solvated LiO_2 intermediate.[69] However, TEGDME only has a donor number of 16.6, but is one of the most popular solvents used in Li–O_2 batteries, demonstrating both high discharge capacity and the formation of large toroid-shaped Li_2O_2 deposits.[49] The purpose of the LiO_2 solvation simulation is to determine whether the solvated state is stable in TEGDME, and to visualize the mechanism of solvation. A snapshot of the molecular configurations in the simulation is shown in Figure 4.1a.

The PMF free energy plot, shown in Figure 4.1b, suggests that TEGDME is capable of solvating LiO_2. A local minimum of $-0.66\,\mathrm{kcal\,mol^{-1}}$ was found at a separation distance of 7.75 Å, which corresponds to the distance at which a TEGDME molecule is able to freely pass between the Li^+ and O_2^-. Minima of $-0.72\,\mathrm{kcal\,mol^{-1}}$ and $-0.64\,\mathrm{kcal\,mol^{-1}}$ were also found at separations of 4.75 Å and 5.75 Å, respectively. The similarity in free energy of all the minima indicates that there is no strong preference for LiO_2 to be in one state (solvated or desolvated) over the other. The free energy is mostly flat at distances greater than 4.0 Å, indicating that coulombic attraction between Li^+ and O_2^- is effectively screened by TEGDME. From the simulation visualization, the TEGDME molecule was found to wrap around the Li^+ cation much like a crown ether, with the oxygen atoms coordinating with the Li^+. This hints to why LiO_2 solvation is possible despite the low donor number of TEGDME. The donor number is measured with a standard Lewis acid, $SbCl_5$, that is much larger than Li^+ and therefore cannot be encapsulated by a single TEGDME molecule. Using O_2^- as the depositing species in the following simulations is therefore justified by its stability in TEGDME electrolyte.

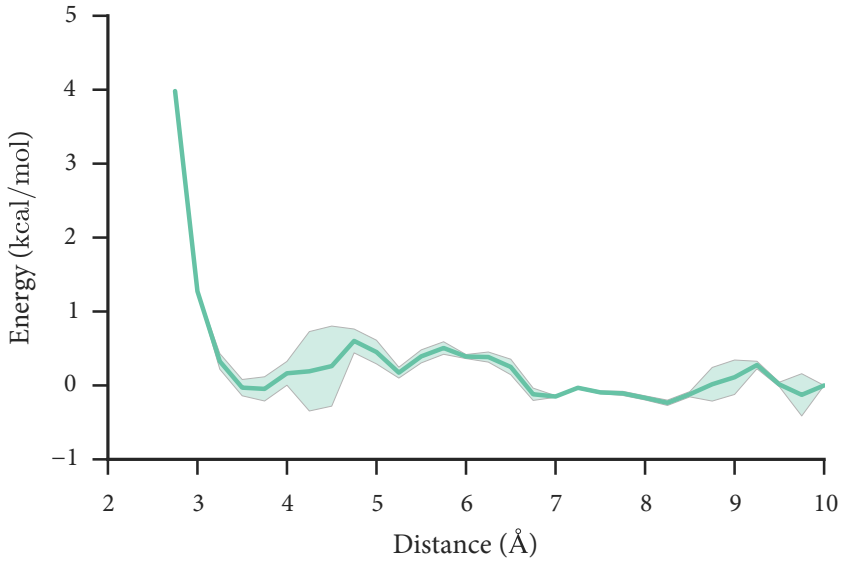

Figure 4.2: PMF free energy as a function of separation distance for O_2^- depositing on neutral graphene.

Deposition on Neutral Graphene

The deposition of O_2^- on neutral graphene was simulated to gain insight on the features of the PMF free energy function that are not electrochemical in origin. In principle, this is equivalent to a battery at open-circuit voltage. Figure 4.2 shows the PMF free energy as a function of separation distance for this set of simulations.

A minimum of $-0.23\,\mathrm{kcal\,mol^{-1}}$ was found at a separation of 8.0 Å, corresponding to the solvated state, as well as a local minimum of $-0.05\,\mathrm{kcal\,mol^{-1}}$ at a separation of 3.75 Å, corresponding to the deposited state. The difference in free energy indicates that the solvated state is slightly more favorable than the deposited state. An energy barrier exists at 5.75 Å with a height of $0.74\,\mathrm{kcal\,mol^{-1}}$ in the direction of deposition and $0.55\,\mathrm{kcal\,mol^{-1}}$ in the direction of solvation. At 25 °C, this barrier height is equal to $1.25k_BT$ and $0.93k_BT$ in the deposition and solvation directions, respectively, indicating that O_2^- is able to exchange between the graphene surface and the electrolyte to a limited extent with thermal energy alone.

On a per-electron basis, the potential barrier for deposition on neutral graphene is 0.032 V, which is only a small fraction of the typical overpotential of 0.2 V in a Li–O_2 cell.[74] This begs the question of whether a charged cathode would affect the energy barrier. Thus, a set of follow-up simulations was performed with a charged graphene surface, rather than with a different cathode surface chemistry, as this was considered the more fundamental question.

Deposition on Charged Graphene

The deposition of O_2^- on a charged graphene surface was simulated to gain further insight into how the act of discharging the Li–O_2 cell, which invariably results in overpotentials

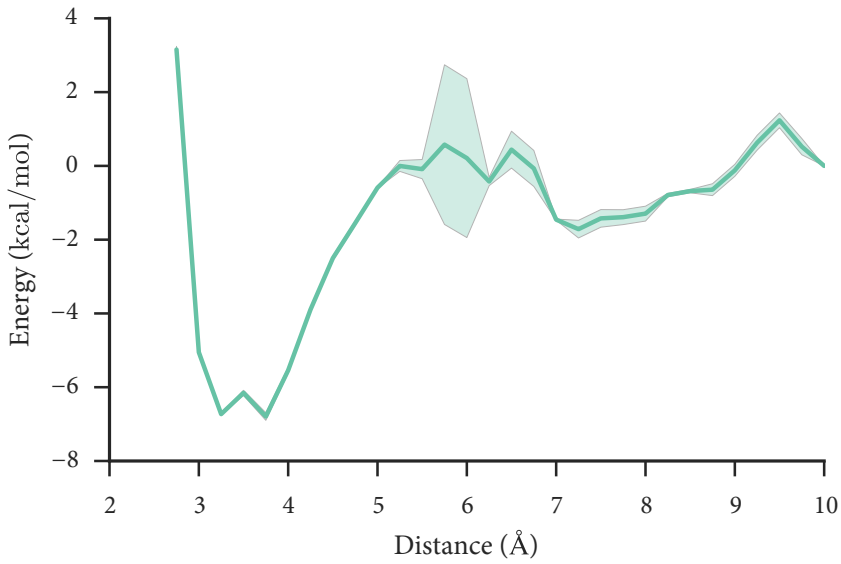

Figure 4.3: PMF free energy as a function of separation distance for O_2^- depositing on negatively-charged graphene.

at both electrodes, affects the free energy of deposition. A negative charge at the cathode is needed to discharge the Li–O_2 cell, which is balanced by the adsorption of positively charged Li^+ ions. For these simulations, the charge of the graphene was set such that its negative charge is exactly balanced by a monolayer of Li^+ ions at a stoichiometric ratio of LiC_6 (*i.e.* $\delta_C^- = -1/6$). This condition is analogous to the limiting case of infinitesimally small discharge current, since any additional negative charge on the cathode will result in the development of an electric field in the bulk electrolyte and the migration of Li^+ ions. Even at this limiting case, the negative charge of the graphene was found to substantially affect the free energy landscape for $O_2{}^-$ deposition by influencing the behavior of the electrolyte near the surface.

Figure 4.3 shows the PMF free energy as a function of distance from the charged graphene surface. The most obvious change from the neutral case in Figure 4.2 is the decreased minimum at 3.75 Å, which now has an energy of $-6.79\,\mathrm{kcal\,mol^{-1}}$. At this distance, there are no TEGDME molecules screening the charge of the Li^+ ions. Thus, the lower energy is the result of coulombic attraction between $O_2{}^-$ and the Li^+ monolayer. The minimum centered at 7.25 Å also decreased in energy to $-1.71\,\mathrm{kcal\,mol^{-1}}$ due to long-range electrostatic attraction, albeit not by as much due to the screening effect of the TEGDME. The height of the energy barrier of deposition, however, increased to $2.29\,\mathrm{kcal\,mol^{-1}}$ ($3.9k_BT$). The simulation visualization, a frame of which is shown in Figure 4.4, reveals that the solvent molecules immediately above the Stern layer are tightly coordinated with the Li^+ ions. Although the Li^+ ions were allowed to diffuse, thermal energy was not sufficient in overcoming the coulombic attraction to the cathode. The Li^+ ions and the coordinated solvent molecules are essentially immobilized on the surface of the cathode. Consequently, the energy barrier for deposition increased because the $O_2{}^-$ must penetrate the layer of coordinated solvent molecules in order to reach the cathode surface.

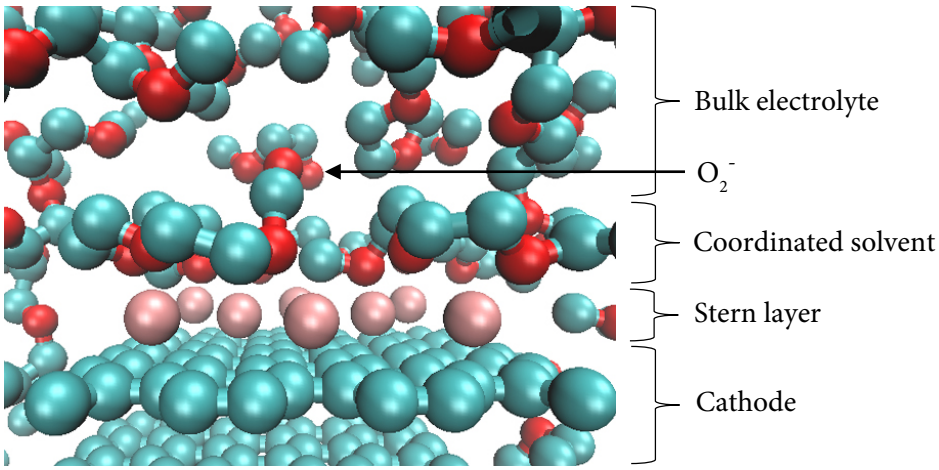

Figure 4.4: Simulation frame showing the structure of the double-layer. Separation distance = 6.0 Å.

This study highlights a previously overlooked contribution to the rate of nucleation. The free energy of LiO_2 dissolution was considered to be the primary determining factor for promoting a solution-mediated discharge mechanism,[69,99] but the kinetic energy barrier formed during discharge may prove to be even more influential in some solvents. In TEGDME, for example, LiO_2 does not have a strong preference of being in the solvated state versus the desolvated state. During discharge, however, the interaction between the solvent molecules and the Li^+ adsorbed on the cathode surface creates a barrier that O_2^- must penetrate through in order to nucleate onto the cathode. The energy barrier is kinetic in nature because it represents the amount of energy needed to "push" the co-adsorbed solvent molecules out of the way. Therefore, thermodynamic calculations alone would not be able to fully predict the size of this energy barrier; other factors such as the length of the solvent molecule and the number of coordination sites would need to be considered together when selecting a solvent for the Li–O_2 battery.

4.2 Open Cathode Structure

The overall discharge reaction in the Li–O_2 battery, $2Li^+ + O_2 + 2e^- \rightarrow Li_2O_2$, ultimately leads to every two electrons corresponding to one molecular unit of Li_2O_2 produced, which is responsible for limiting the discharge capacity in the mechanism discussed in the previous chapter. However, the only Faradaic reaction involved in the formation of Li_2O_2 is the formation of the superoxide precursor, $O_2 + e^- \rightarrow O_2^-$ (eq 1.5a). In a hypothetical scenario, where disproportionation to Li_2O_2 does not occur, the Faradaic reaction would be able to run indefinitely, enabling the full theoretical discharge capacity, because the cathode surface would not become passivated by Li_2O_2. While complete abatement of Li_2O_2 formation is not realistic, it may be possible to slow down the rate of Li_2O_2 formation without hindering the rate of LiO_2 formation.

The capacity of a Li–O_2 cell has been shown in multiple studies to increase with the pore size of the carbon cathode.[56,100] Usually, this correlation is qualitatively rationalized with the hypothesis that the larger pores permit more Li_2O_2 growth before it limits O_2 diffusion. However, if electronic resistivity reigns dominant over O_2 diffusion, an alternative explanation is necessary: the larger pores provide access to a greater volume of electrolyte, which delays the saturation of LiO_2 and slows down the rate of nucleation of Li_2O_2 particles. A combined experimental and modeling study was used to test this alternative hypothesis. Vapor grown carbon fiber (VGCF) provides a cathode material with an open void structure, allowing LiO_2 to access a much larger volume of electrolyte. The nucleation and growth model presented in the previous chapter was expanded to include the transient mass transport of LiO_2. The results of this study show that at any given current density, the capacity per carbon surface area is higher with a more open cathode structure. We propose that the rate of nucleation is abated by the diffusion of LiO_2 into the electrolyte, until a supersaturation-driven mechanism accelerates nucleation at high current density.

4.2.1 Discharge Experiments

VGCF cathodes were prepared according to the procedure described in appendix A.1.2. The electrolyte (1 M $LiCF_3SO_3$ in TEGDME) was prepared and coin cells were assembled in the same manner as they were for the cells with Super P cathodes (appendix A.2-A.4). Galvanostatic discharge experiments were performed using a similar approach to that discussed in Chapter 3, but the cutoff voltage was reduced to 2.0 V to accommodate the lower voltage plateaus from the high current tests. The lower cutoff voltage is not expected to have a significant effect on discharge capacity due to the steep voltage drop at the end of the discharge curve. SEM images were taken after discharge, following the procedure described in appendix A.5.

The VGCF cathodes have a more open pore structure in contrast to the packed morphology of the Super P cathodes, as seen in SEM images of undischarged cathodes (Figure B.6). This is largely due to the different aspect ratios of the particles themselves. Super P particles, are roughly spherical in shape with a diameter of ∼40 nm, leading to a packed sphere structure with an average pore size of only 11.9 nm.[101] VGCF, on the other hand, is composed of fibers approximately 150 nm in diameter but 10 μm to 20 μm in length, leading to a high aspect ratio that resists close-packing.[102] Instead of having well-defined pores, the VGCF cathode appears to have continuous voids throughout.

The morphology of the Li_2O_2 particles formed during discharge of the VGCF cathodes were unexpectedly large. Figure 4.5 shows the SEM images of the discharged VGCF cathodes, showing particles up to ∼4 μm in diameter. To our knowledge, these are the largest Li_2O_2 particles ever reported in a Li–O_2 cell. VGCF has a much lower specific surface area (13 $m^2\ g^{-1}$) than Super P (62 $m^2\ g^{-1}$),[102,103] which means the real current density, normalized to the microscopic surface area of the carbon material, would be higher in VGCF if they were subjected to the same geometric current density, normalized to the superficial area of the carbon cathode, as the Super P cathodes. A higher effective current density in a VGCF cathode would drive a higher nucleation rate of Li2O2 particles, which would reduce the average particle size and lower the cell discharge capacity. It is apparent from Figure 4.5, however, that there are significantly fewer and larger Li_2O_2 particles on the VGCF than there are on Super P at the same geometric current density.

The discharge curves (Figure 4.6) also show that cells with VGCF cathodes behave very differently as a function of current density than those with Super P cathodes. While the voltage plateau does decrease with increasing current density, the capacity does not have a clear relationship until the current density reaches 108.8 μA cm^{-2}, after which it decreases. A duplicate of this experiment, shown in Figure B.7 also exhibited this behavior. This

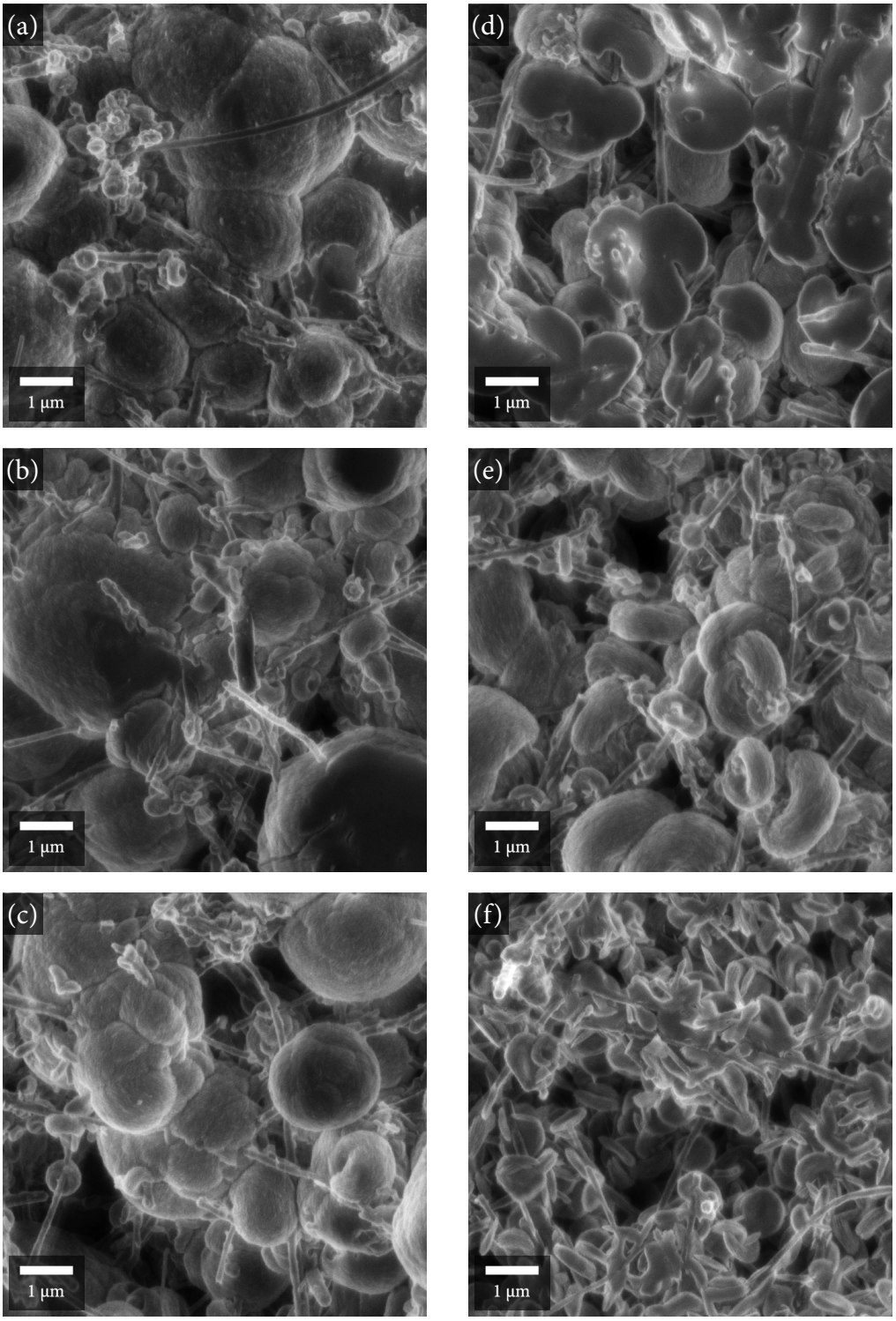

Figure 4.5: SEM images of discharged VGCF cathodes. Geometric current densities of (a) 5 µA cm^{-2}, (b) 10 µA cm^{-2}, (c) 20 µA cm^{-2}, (d) 40 µA cm^{-2}, (e) 80 µA cm^{-2}, and (f)160 µA cm^{-2}.

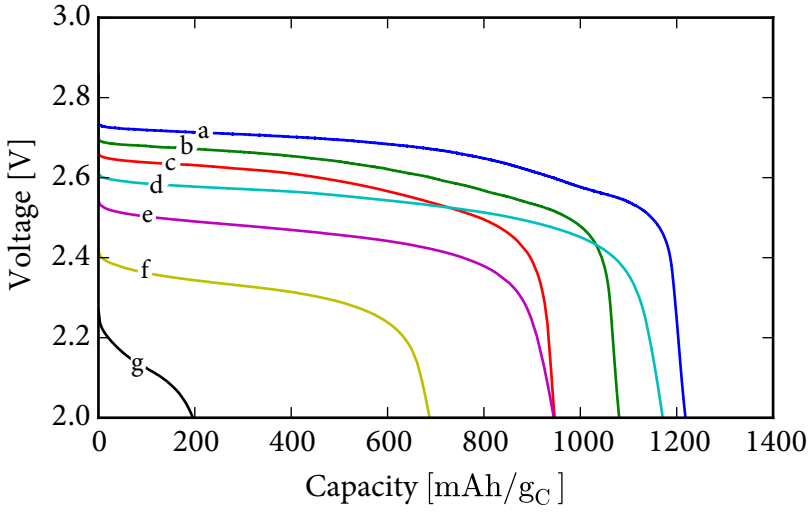

Figure 4.6: Discharge curves of cells with VGCF cathodes discharged at geometric current densities of (a) 5.1 μA cm^{-2}, (b) 10.9 μA cm^{-2}, (c) 23.5 μA cm^{-2}, (d) 50.5 μA cm^{-2}, (e) 108.8 μA cm^{-2}, (f) 234.5 μA cm^{-2}, (g) 505.2 μA cm^{-2}.

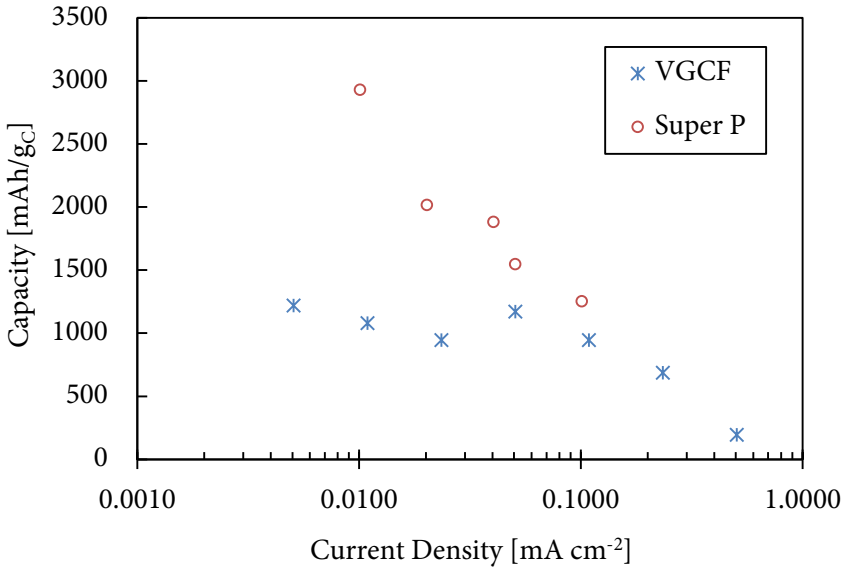

Figure 4.7: Capacity as a function of geometric current density, compared between VGCF and Super P.

unusual capacity-vs-current density relationship can be better visualized in Figure 4.7, where the capacity versus current density plot for the VGCF cathode is contrasted with that for Super P, which had a clear inverse relationship between capacity and current density at all current densities tested.

The unusual performance characteristics and the large Li_2O_2 particles may both be the result of the open void structure of VGCF, which can facilitate diffusion of LiO_2 away from the carbon surface. First, enhanced diffusion leads to a lower surface concentration of LiO_2, which reduces the nucleation rate. Second, access to a large reservoir of electrolyte enabled by the VGCF structure leads to a transient buildup of LiO_2 concentration. This, in turn, implies a transient increase in nucleation rate. As a result, increased current would not have as strong of an impact on nucleation rate because the rise in nucleation rate is limited by how quickly the LiO_2 concentration can reach steady-state. To test the proposed hypothesis against the experimental performance characteristics, the effects of LiO_2 diffusion will need to be formulated mathematically. The model presented in the previous chapter assumes the pore sizes are sufficiently small, such that LiO_2 concentrations and nucleation rates reach steady state immediately. We show that the inclusion of LiO_2 diffusion effectively reduces the cell capacity's dependence on current density by delaying the rise in nucleation rate.

4.2.2 Model Development

To test the effects of LiO_2 diffusion on the nucleation and growth of Li_2O_2, a transient diffusion model was developed and integrated with the Li_2O_2 nucleation model described in chapter 3. Figure 4.8 illustrates the scheme of the diffusion model. For simplicity, a one-dimensional spatial domain was used to represent the electrolyte, $x \in [0, L]$, where $x = 0$ represents the cathode surface and $x = L$ represents an imaginary no-flux plane or

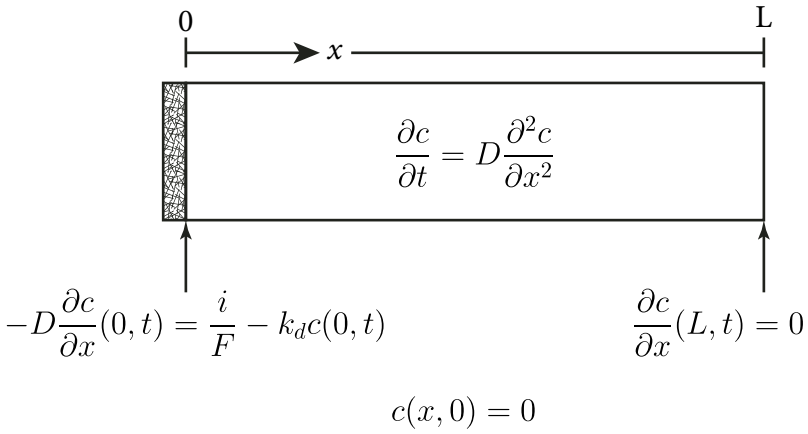

Figure 4.8: Scheme of the LiO_2 diffusion model.

plane of symmetry. Fick's second law applies within the electrolyte,

$$\frac{\partial c}{\partial t} = D_{\mathrm{LiO_2}} \frac{\partial^2 c}{\partial x^2} \tag{4.1}$$

At the cathode surface, the diffusive flux is balanced with the rate of formation due to Faradaic reaction and the rate of depletion due to disproportionation of LiO_2,

$$-D_{\mathrm{LiO_2}} \frac{\partial c}{\partial x}(0,t) = \frac{i}{F} - k_d c(0,t) \tag{4.2}$$

where k_d is the heterogeneous first order rate constant for LiO_2 disproportionation. At $x = L$ a no-flux boundary condition was enforced:

$$\frac{\partial c}{\partial x}(L,t) = 0 \tag{4.3}$$

No LiO_2 is present at the start of discharge. Thus, the initial condition was set to

$$c(x,0) = 0 \tag{4.4}$$

To aid in solving the model, eqs 4.1-4.4 were non-dimensionalized using the following substitutions:

$$\tilde{x} = x/L \qquad \tilde{t} = tD_{\mathrm{LiO_2}}/L^2 \qquad \tilde{c} = c/c_\infty \tag{4.5}$$

c_∞ is the steady-state LiO_2 concentration in the electrolyte, which can be found by setting $\partial c/\partial x$ in eq 4.2 to zero, corresponding to a flat concentration profile.

$$c_\infty = \frac{i}{Fk_d} \tag{4.6}$$

Applying these substitutions, the dimensionless diffusion equation, boundary conditions,

and initial condition are

$$\frac{\partial \tilde{c}}{\partial \tilde{t}} = \frac{\partial^2 \tilde{c}}{\partial \tilde{x}^2} \tag{4.7}$$

$$\frac{\partial \tilde{c}}{\partial \tilde{x}}(0,\tilde{t}) = \mathrm{Bi}_m\left(\tilde{c}(0,\tilde{t}) - 1\right) \tag{4.8}$$

$$\frac{\partial \tilde{c}}{\partial \tilde{x}}(1,\tilde{t}) = 0 \tag{4.9}$$

$$\tilde{c}(\tilde{x},0) = 0 \tag{4.10}$$

where $\mathrm{Bi}_m = k_d L/D_{\mathrm{LiO_2}}$ is the mass transfer Biot number. Eqs 4.7-4.10 were solved using the Crank-Nicolson finite differences method.

To combine LiO_2 diffusion with nucleation and growth, the relationships between the LiO_2 surface concentration and the nucleation and growth rates are required. The nucleation rate of Li_2O_2 was modeled as an apparent second-order process,

$$J = k_n c^2 \tag{4.11}$$

which was found to empirically match the predictions of the atomistic model for the Super P experiments. This form can be rationalized by considering that two LiO_2 molecules are required to disproportionate to Li_2O_2. In addition, the growth rate was scaled according to the transient LiO_2 concentration with a modification to eq 4.12.

$$\frac{dr}{dt} = \frac{1}{1-\theta}\frac{i}{2F}\left(\frac{M}{\rho}\right)_{\mathrm{Li_2O_2}}\frac{c(0,t)}{c_\infty}\frac{1}{2\pi\sum_k n_j r_j^2} \tag{4.12}$$

This assumes Li_2O_2 growth is a first order process, which is rationalized by the stability of oxygen-rich (LiO_2-stoichiometry) layers on Li_2O_2 surfaces.[61] During the initial stages of discharge, when $c(0,t) < c_\infty$, the growth rate rises in proportion to the concentration of LiO_2 near the cathode surface. Once the LiO_2 concentration reaches steady state, the Li_2O_2 growth rate also reaches steady state and becomes stoichiometrically equivalent to the discharge current. Eqs 4.11 and 4.12 were integrated together with eqs 3.7 and 3.1 following the techniques described in section 3.3.3, and the discharge curves were calculated from the overpotential.

Parameter	Description	Value		Source(s)
c_{sat}	Saturation concentration of LiO_2	$21.7\ mol\ m^{-3}$		Fitted.
D_{LiO_2}	Diffusion coefficient of LiO_2	$8.68 \times 10^{-7}\ cm^2\ s^{-1}$		Assumed to be $\frac{2}{5}D_{O_2}$.[49,104]
k_d	Heterogeneous rate constant of LiO_2 disproportionation	$2.9 \times 10^{-7}\ cm\ s^{-1}$		Assumed.
k_{sat}	Rate constant of nucleation due to supersaturation	$7.8 \times 10^{7}\ cm^{-1}\ s^{-1}$		Fitted.
		Super P	VGCF	
α	Charge transfer coefficient of O_2 reduction	0.656	0.610	Tafel plot.
A	Total cathode area	$558\ cm^2$	$117\ cm^2$	Equal to $m_C \cdot A_{specific}$
A_{spc}	Specific area of carbon	$62\ m^2\ g^{-1}$	$13\ m^2\ g^{-1}$	Manufacturer specification.[102,103]
E_0	Open circuit voltage	2.85 V	2.83 V	Measured from experiments.
i_0	Exchange current density of O_2 reduction	$3.7 \times 10^{-4}\ mA\ cm_{geo}^{-2}$	$1.7 \times 10^{-4}\ mA\ cm_{geo}^{-2}$	Tafel plot.
k_n	Rate constant of heterogeneous nucleation	$1 \times 10^{14}\ mol\ cm\ s^{-1}$	$4.5 \times 10^{12}\ mol\ cm\ s^{-1}$	Fitted.
L	Effective diffusion length	11.9 nm	40 µm	Super P: Younesi *et al.*;[101] VGCF fitted.
m_C	Mass of carbon	(0.9 ± 0.1) mg		Measured from experiments.
R_Ω	Ohmic cell resistivity (normalized to geometric area)	$624\ \Omega\ cm^2$	$883\ \Omega\ cm^2$	Tafel plot.

Table 4.1: List of parameters for diffusion-nucleation-growth model.

4.2.3 Analysis and Discussion

The LiO_2 diffusion model introduces several parameters that have not yet been measured in experiments, such as the heterogeneous rate constant of disproportionation (k_d) and the diffusion coefficient (D_{LiO_2}) of LiO_2 in TEGDME. However, the model can be constrained by considering its limiting conditions. In the limit of small pore size (small L) or low current density, the LiO_2 concentration should reach steady state quickly, resulting in the simple inverse relationship between capacity and current density seen in Super P cathodes. Essentially, parameters should be chosen such that the predicted discharge curves match well with those of Super P cathodes, while being able to extrapolate to larger pore sizes to match the discharge curves of VGCF cathodes with minimal adjustment to other parameters. Table 4.1 summarizes the parameters used in the model. Although D_{LiO_2} has not been measured in TEGDME, the diffusion coefficient of O_2^- has been estimated to be $\sim\frac{2}{5}D_{O_2}$ in acetonitrile.[104] Since LiO_2 is capable of existing as a solvated ion pair in TEGDME,[72] we will assume the hydrodynamic properties of O_2^- apply. A value of $D_{LiO_2} = 8.68 \times 10^{-7}$ cm^2 s^{-1} was chosen, which is $\sim\frac{2}{5}$ of $D_{O_2} = 2.17 \times 10^{-6}$ cm^2 s^{-1} for TEGDME.[49] α, i_0, and R_Ω were found by *iR*-corrected Tafel plots of the discharge plateau voltages with current density (Figure B.5). Although a homogeneous first-order rate constant of LiO_2 disproportionation of 2.9×10^{-3} s^{-1} has been proposed by Peng *et al.* based on cyclic voltammetry, the LiO_2 disproportionation is likely to follow a more complex heterogeneous process in a working coin cell. A value of $k_d = 2.9 \times 10^{-9}$ m s^{-1} was found to work well for the purposes of this model. Considering the difference in dimensionality and the dependence of the homoegeneous rate constant on the experimental conditions, the heterogeneous value is not necessarily comparable to the homogeneous value. k_n was fit according to the capacity of the lowest current discharge curve of each respective cathode type.

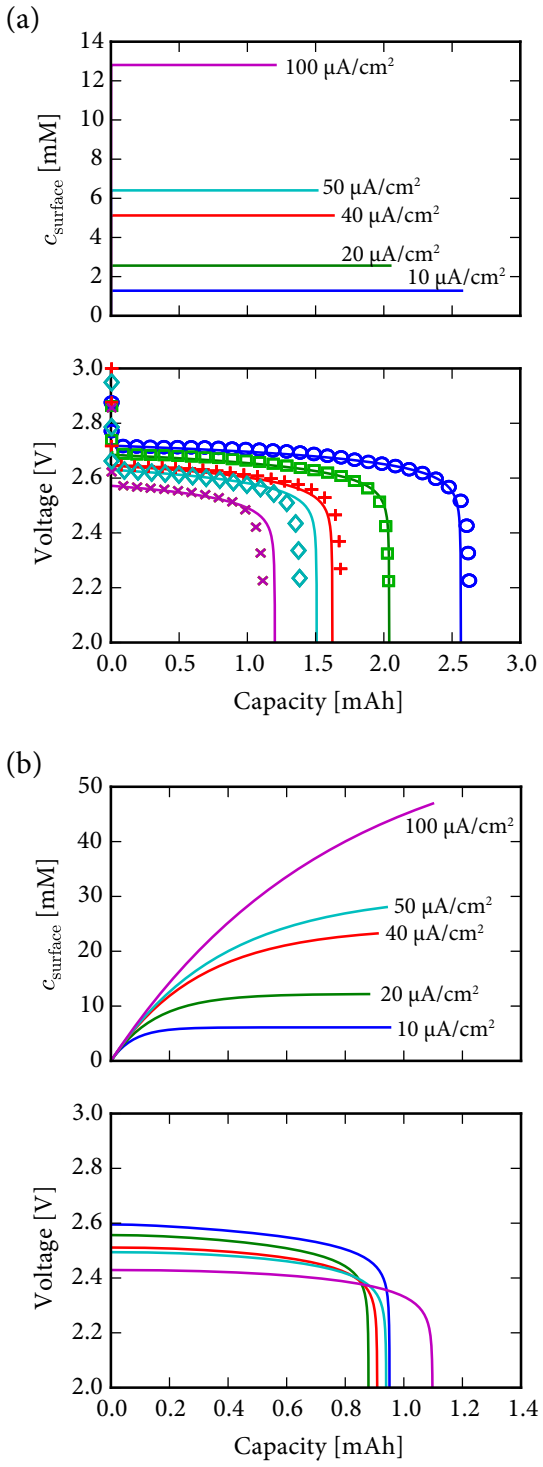

Figure 4.9: Comparison of predicted LiO_2 concentrations and discharge curves for (a) Super P and (b) VGCF cathoes.

Figure 4.9 compares the model's predicted discharge curves and surface LiO_2 concentrations for Super P and VGCF. For Super P, L was set to the average pore diameter, 11.9 nm.[101] At this pore size, the LiO_2 concentration reaches its steady state value quickly, leading to the immediate onset of nucleation. A strong inverse relationship between the capacity and current density is seen in the simulated discharge curves, matching the experimental curves. However, when the characteristic length is increased to $L = 40\,\mu m$, the greater volume of electrolyte that can be accessed by LiO_2 leads to a slower rise in concentration. The transient accumulation of LiO_2 leads to an interesting behavior when increasing current densities are considered. At low current density (*e.g.* $i_{geo} = 10\,\mu A\,cm^{-2}$), the LiO_2 concentration is still able to reach steady state early in the discharge process. However, as the current density increases, the concentration reaches steady state later in the discharge process. At $i_{geo} = 40\,\mu A\,cm^{-2}$, most of the discharge capacity has been consumed by the time the concentration reaches steady state. The nucleation rate, which is limited by this rise in LiO_2 concentration, is therefore a fraction of what it would have been if the LiO_2 concentration reached steady state immediately. This leads to a weaker dependence of the capacity as a function of current density, as seen in the corresponding discharge curves.

The model predicts a peculiar phenomenon in which the capacity actually begins to increase with current density at $\sim 40\,\mu A\,cm^{-2}$. At this point, the nucleation rate is unable to increase on par with the current density as it becomes limited by the rate of diffusion. This behavior was observed in experiments (Figures 4.6 and B.7) as well, although the exact position of the turnaround point varies between $\sim 25\,\mu A\,cm^{-2}$ to $100\,\mu A\,cm^{-2}$. However, this increase tends to only occur over a small range of current densities in experiments; the capacity once again drops rapidly with current density after $100\,\mu A\,cm^{-2}$. In its present incarnation, the model predicts that the capacity will continue to increase with current density. This divergence was not found to occur when L is small,

as in the Super P case, which suggests that the unbounded transient accumulation of LiO_2 is at fault. We propose that an additional supersaturation-driven mechanism is responsible for accelerating the nucleation rate at high current density, considering how the LiO_2 was allowed to reach higher concentrations in the VGCF simulation than in the Super P simulation. To determine a possible relationship between LiO_2 concentration and nucleation rate, a term representing the residual nucleation rate (J_r) required to achieve the experimental capacity was added to eq 4.11:

$$J = k_n c^2 + J_r \tag{4.13}$$

The residual nucleation rate was found to fit to the following function:

$$J_r = \frac{c_\infty}{c_{\text{sat}}} k_{\text{sat}} \exp\left(\frac{c_\infty}{c_{\text{sat}}}\right) \tag{4.14}$$

where c_{sat} is the saturation concentration and k_{sat} is the rate constant of this process. The fit of eq 4.14 is shown in Figure B.8. Although this relationship is empirical, a reasonable value of 21.7 mol m^{-3} was found for c_{sat}. The model's capacity predictions, both with and without the added supersaturation mechanism, are compared with the experimental capacities in Figure 4.10a. Evidently, a supersaturation mechanism is necessary to prevent the capacity from diverging as a function of current density. It should be noted that eq 4.14 has a negligible effect on the Super P simulations, since the steady state concentration of LiO_2 is lower due to the higher real surface area of Super P available for heterogeneous disproportionation. In general, the simulated discharge curves for VGCF agree well with experiment, except in the region around 50 μA cm^{-2}, where it transitions from a second-order nucleation process to a supersaturation-driven process.

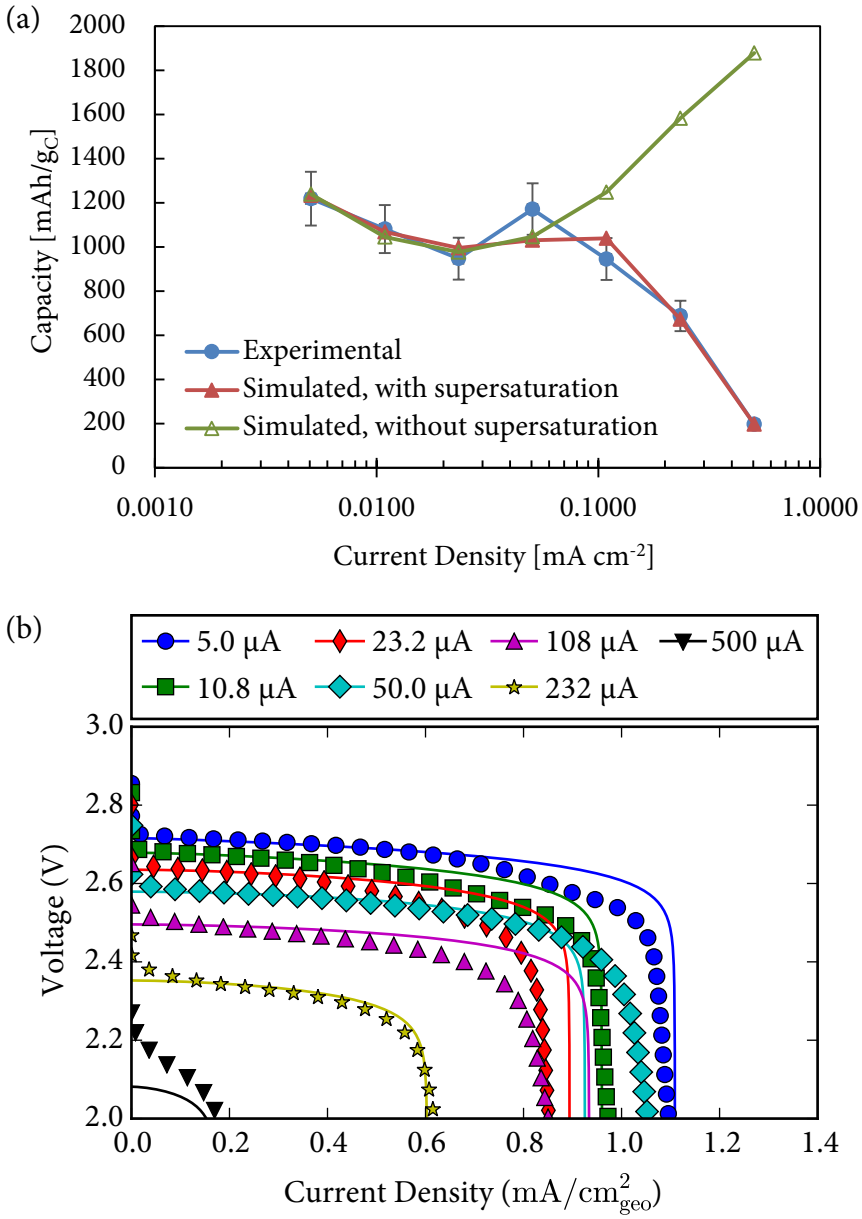

Figure 4.10: (a) Comparison of experimental discharge capacities of VGCF cathodes to simulated capacities, both with and without the supersaturation mechanism. Experimental error bars are based on cathode weight uncertainty. (b) Comparison of experimental discharge curves of VGCF cathodes to those predicted by the model, with supersaturation effect included.

4.3 Conclusions

The influence of the solvent on nucleation energy barriers in the Li–O_2 battery cathode was elucidated through a series of fixed-separation molecular dynamics simulations. Despite its relatively low donor number, TEGDME was found to solvate $Li^+ + O_2^-$ by encapsulating the Li^+ ion in a manner analagous to what is seen in bulk electrolytes containing lithium salts. This implies that the dominant mechanism of Li_2O_2 formation in TEGDME-based electrolytes is through the deposition of solvated LiO_2. Following this observation, the free energy for the deposition of $O_2{}^-$ on a graphitic cathode was determined as a function of separation distance. It was found that the energy barrier of nucleation increases by a factor of three simply by the application of a negative charge on the cathode. This increased energy barrier arises from the formation of the electrical double layer, which consists of a Stern layer of adsorbed Li^+ ions and a layer of solvent molecules tightly coordinated to the Li^+ ions in the Stern layer. This work uncovers a previously unknown mechanism for the role of Li^+-coordinating solvents play in increasing the discharge capacity of LiO2 batteries: not only do they make LiO_2 solvation more thermodynamically favorable, they also form a more tightly-bound solvent layer on the cathode that acts as a kinetic barrier to nucleation.

Many future studies could be done to refine or extend this work. For example, the OPLS force field is completely classical and makes no considerations of polarization effects that may happen when atoms are brought close together. In spectroscopic studies by Andrews and Smardzewski, the lithium and the superoxide in LiO_2 are ionically bonded, but with weak polarizability at close proximity.[105,106] It will be helpful to supplement these studies with *ab initio* calculations to account for this change in free energy. In addition, the claim that the donor number misrepresents TEGDME's ability to solvate Li^+ will need to be verified by simulation as well. The coordination energy between the solvent molecule

and $SbCl_5$ is used to determine the donor number of a solvent, but glymes can have multiple points of coordination around smaller cations such as Li^+. Our results suggest that electrolyte additives such as crown ethers, with even greater affininity for Li^+, or electrolyte solvents that include polymers with ether oxygens, may be even more effective in regulating nucleation of LiO_2. Simulation and experimental studies that directly probe these effects are needed to expand our repertoire of promising solvents for the Li–O_2 cell.

The use of a cathode material with an open void structure shows promise as a method for enabling higher current density Li–O_2 cells. Despite the relatively low specific surface area of VGCF, it is capable of growing and accommodating large particles of Li_2O_2. Furthermore, its capacity is a weak function of current density until a geometric current density of 0.1 mA cm^{-2}. We propose that the open void structure of VGCF allows LiO_2 produced during discharge to readily diffuse into the electrolyte. The diffusion model found that increasing the characteristic diffusion length from nanometer-scale to micron-scale increases the time it takes for LiO_2 to reach steady state. The rate of nucleation is therefore limited by the rate at which LiO_2 accumulates. This reduces the effect of current density on nucleation rate and, based on the Li_2O_2 nucleation and growth model, its effect on capacity. Above a certain current density ($\sim$0.1 mA cm^{-2} in our tests), however, the capacity once again decreases. We suspect this is due to the supersaturation of LiO_2 in the electrolyte.

Additional studies on the role of LiO_2 solubility will be beneficial towards testing the validity of this strategy, as well as expanding its capabilities. In this study, a saturation concentration of $\sim$20 mM was estimated for LiO_2, but this value comes with high uncertainty due to its dependence on other model parameters, and is likely to only be valid for this particular system. LiO_2 solubility is expected to depend heavily on the solvent in use,[69] the presence of water,[72] and the even choice of salt anion.[107] In addition, experimental

studies on LiO_2 solubility thus far focus on the disproportionation reaction as the driving force for LiO_2 deposition. In this study, the sharp decline in discharge capacity at the high current density tests suggest that a separate supersaturation-driven deposition mechanism may become dominant with high concentrations of LiO_2. This is challenging to test experimentally because LiO_2 can spontaneously disproportionate to form Li_2O_2, making supersaturation-driven deposition difficult to distinguish. Nonetheless, improving the solubility of LiO_2 can enable higher current density operation of the Li–O_2 cell, as it allows for the stable accumulation of LiO_2 and delays the onset of capacity-limiting nucleation on the cathode surface.

CHAPTER 5

STRATEGIES TO IMPROVE RECHARGEABILITY

The studies presented thus far focus on the capacity-limiting processes within a single discharge step. For the Li–O_2 battery to become commercially viable, however, it must be able to sustain its capacity over many cycles. It is estimated that the energy spent to manufacture a electric vehicle Li-ion battery pack is equal to 25% of the cumulative energy that the battery pack is capable of delivering over 10 years of use.[108] This implies that the battery pack should supply thousands of cycles if used on an almost-daily basis. For example, lithium iron-phosphate cells produced by A123 Systems, Inc. can retain 94% of its original capacity after 1000 complete cycles.[109] In contrast, the vast majority of long-term cycling tests with Li–O_2 cells are limited to 100 cycles.[37,39,110–112] Because most long-term Li–O_2 cycling studies implement a capacity-limited cycling scheme, the degree of capacity fade for these tests is rarely quantified. At the time of this writing, the best reported capacity retention for a Li–O_2 cell undergoing 100 complete cycles is 98%, which was achieved using a TiC-based cathode.[113] Other notable cathode materials that can undergo long-term cycling without controlling the discharge capacity are Ru nanoparticles on indium tin oxide (ITO),[114] nanoporous gold,[115] and RuO_2 nanosheets.[116] Although these carbon-free cathodes are capable of stable long-term cycling, they are denser and more expensive to manufacture than carbonaceous cathodes. The higher density translates to a lower specific capacity, *e.g.* 850 mAh g^{-1} for RuO_2,[116] versus 4000 mAh g^{-1} for Super P in this study (both discharged at 200 mA g^{-1}).

Carbonaceous cathodes are known to experience severe capacity fading when cycled at full capacity. A study by Lim *et al.* shows that a cell using Ketjenblack carbon (Akzo Nobel N.V.) loses ~90% of its capacity in just eight full-capacity cycles, but when the capacity of each cycle is limited to 500 mAh g^{-1}, the cell could run for more than 50 cycles, leading

to a cumulative capacity more than twice as high as the cell that underwent complete cycles.[35] In general, the vast majority of cycling experiments reported in the literature that use carbonaceous cathodes are done by limiting each cycle to a fraction of the full capacity.[36–39] The reason why complete cycles are detrimental to carbon-based electrodes is not definitively known, but it is typically attributed to the electrochemical decomposition of carbon when the voltage is allowed to go beyond the plateaus. Differential electrode mass spectrometry (DEMS) studies show that cathode decomposition accounts for < 1% of losses during discharge, but up to 10% of losses during charge when the cell voltage exceeds 3.5 V.[117,118]

Two opportunities for improving the rechargeability of carbon cathodes can be identified from our current knowledge of cathode decomposition. First, the small electrochemical losses during discharge are insufficient to explain the rapid capacity fading during full-capacity cycling. In this chapter, we propose an alternative hypothesis in which the growth of Li_2O_2 during discharge strains the cathode structure and electronically isolates the constituent carbon particles. We test this by using electrochemical impedance spectroscopy (EIS) to measure the capacitance of the cathodes in the charged state after varying numbers of cycles. A cathode made from vapor grown carbon fibers (VGCF) is demonstrated to achieve a stable reversible capacity even with full-depth cycling due to its resilience towards electronic isolation. Second, electrochemical cathode decomposition, which accounts for at least 10% of capacity loss, can be significantly reduced if the cell potential is kept low during charging. One method to accomplish this is to use a soluble redox mediator to improve the kinetics of Li_2O_2 oxidation. In this chapter, we will present

some preliminary studies on redox mediators and provide a perspective for future studies.

5.1 Resilience Against Electronic Isolation

One potentially deal-breaking aspect of carbon cathodes in the Li–O_2 cell is how quickly they lose capacity when subjected to full-depth discharge. The rate of capacity loss is too great (up to 50% per cycle[35]) to be explained by chemical decomposition of the cathode alone (< 1% and ~10% for discharge and charge, respectively[117,118]). In this study, an alternative hypothesis, in which the physical strain caused by the growth of Li_2O_2 leads to the electronic isolation of carbon particles, is explored. This is similar to how repeated cycling of Li-ion batteries is known to strain and damage the crystal structure of intercalation compounds,[119] except Li_2O_2 growth causes breakage between particles in the cathode matrix rather within the particles themselves. If this is the case, the active surface area of the cathode should decrease during cycling as parts of the carbon become isolated from the conductive matrix. The active surface area of an cathode could be estimated from its double layer capacitance, which is proportional to the surface area for a given electrochemical system.[120] Furthermore, if portions of the cathode are indeed being electronically isolated by Li_2O_2, a more physically resilient cathode should help the cell retain its capacity.

5.1.1 Experimental

Two carbon cathode materials with different geometries, Super P and VGCF, were tested in Li–O_2 coin cells subjected to galvanostatic cycling. Super P particles are roughly spherical in shape with an average grain size of ~40 nm[101] Despite its common usage in Li–O_2 studies, Super P is known to rapidly fade in capacity when used as a cathode.

In contrast, VGCF particles are rod-like, averaging 10 μm to 20 μm in length,[102] which should allow VGCF to percolate and form a conductive matrix more readily. In epoxy resin composite conductivity tests, VGCF was found to percolate at 0.95% by weight while Super P percolated at 3.8% by weight.[121,122] We suspect the lower percolation threshold of VGCF will enable it to resist electronic isolation better than Super P, and thus retain its capacity when cycled.

The coin cells were prepared as described in appendix A.1-A.4, with 60 h of rest time before the start of the tests. Using a Neware BTS–5V1mA battery tester, the cells were discharged at a constant current of 0.2 mA to a lower voltage limit of 2.2 V, allowed to rest at open circuit for 30 min, then charged at a constant current of 0.2 mA to an upper voltage limit of 4.65 V. 30 min of rest at open circuit was allotted between each discharge-charge cycle. Cells were stopped in the charged state after 1, 2, 4, 8, and 35 cycles and removed for EIS measurement. Prior to EIS measurement, the cells were stored in an argon-filled glovebox for three days to degas the electrolyte of oxygen.

Coin cells were stored in an argon-filled test chamber (Figure B.1) during EIS measurements. Measurements were taken using a Model 1470E CellTest System (Solartron Analytical) over a frequency range of 100 mHz to 250 kHz and a signal amplitude of 10 mV. The bias potential was set equal to the open circuit voltage of the cell.

5.1.2 Results

Galvanostatic Cycling

The voltage curves of the Super P and VGCF cells are shown in Figure 5.1. Both cells experience a significant drop in capacity over the first few cycles. However, the VGCF cell

(a)

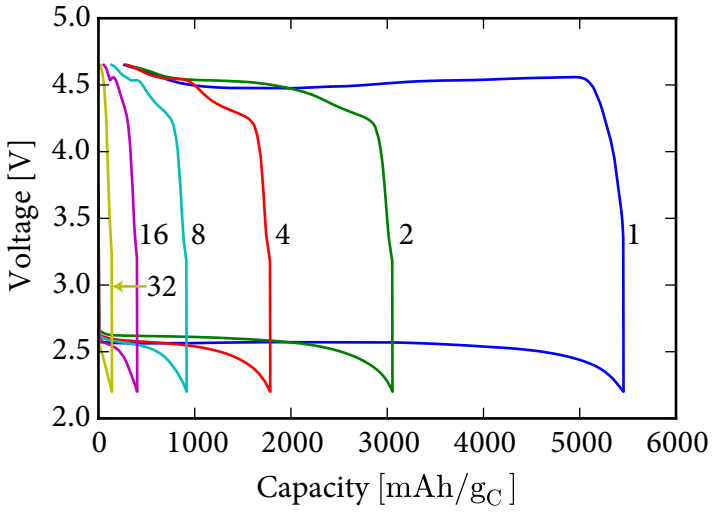

(b)

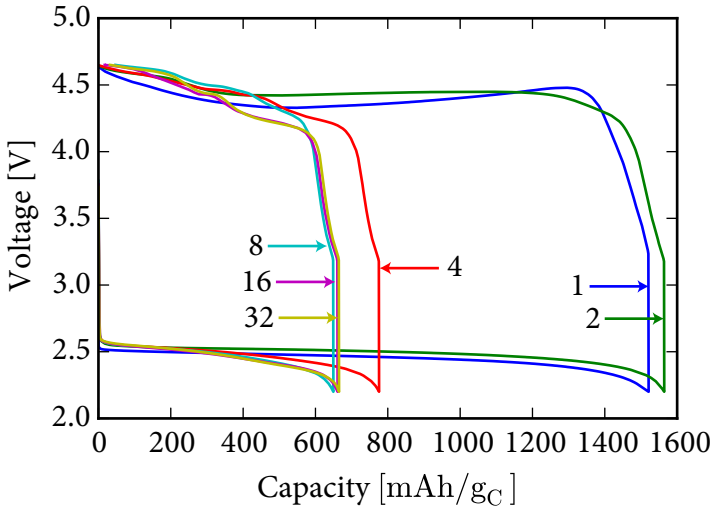

Figure 5.1: Voltage curves of selected cycles in long-term cycling test. (a) Super P cathode, (b) VGCF cathode.

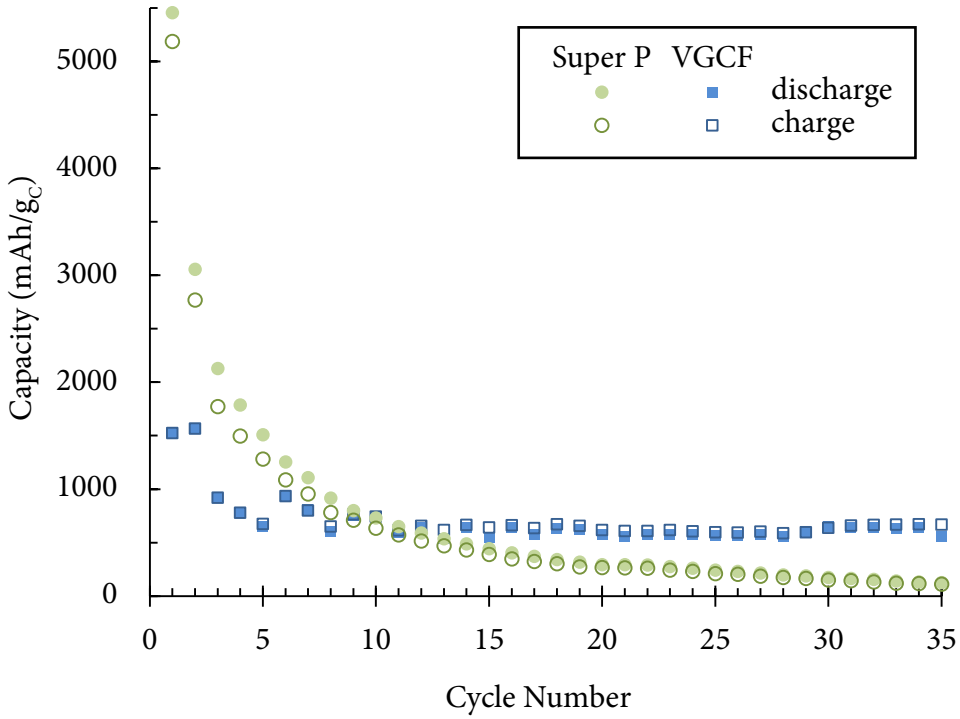

Figure 5.2: Capacity as a function of cycle number for cells with Super P and VGCF cathodes. The capacity of the VGCF cell stabilizes at 630 mAh g^{-1} while the Super P cell capacity continues to fall.

eventually reaches a state of constant capacity, whereas the capacity of the Super P cell continues to drop. In fact, the voltage curves of the VGCF cell for cycles 8–32 are nearly identical to one another. The difference in the trends is more readily seen in Figure 5.2, which plots the capacity of both cells as a function of cycle number. The cell with a VGCF cathode stabilizes to an average capacity of 630 mAh g^{-1} while the cell with a Super P cathode asymptotically fades to zero. The reversible capacity of VGCF is better than some of those achieved by carbon-free cathodes, such as nanoporous gold (300 mAh g^{-1}) and TiC (530 mAh g^{-1}).[110,113]

Electrochemical Impedance Analysis

The evolution of the impedance spectra can provide clues to the mechanism of capacity fade. Figure 5.3 shows the impedance spectra after the 1st, 8th and 35th cycles. While the impedance spectra of the Super P cells differed significantly with the number of cycles, those of the VGCF cells remained relatively unchanged. To extract capacitance values, the impedance spectra were analyzed with an equivalent circuit model. Following the method used by Højberg *et al.* for fitting impedance spectra of Li–O_2 cells,[123] we use an equivalent circuit consisting of three Voigt elements—each of which consists of a resistor and constant phase element (CPE) connected in parallel—and a series resistor, as shown in Figure 5.4. The impedance of an individual Voigt element is given by

$$Z_i(\omega) = \frac{R_i}{1 + (j\omega)^{n_i} Q_i R_i} \tag{5.1}$$

where R_i is the DC resistance, and Q_i and n_i are parameters of the CPE.[124] The CPE models the behavior of a non-deal capacitor, where a value of $n_i = 1$ is equivalent to an ideal capacitor. Thus, if n_i is high, *e.g.* between 0.7 and 1, the effective capacitance of a Voigt element can be calculated as[123,124]

$$C_i^* = Q_i^{1/n_i} R_i^{1-n_i} / n_i \tag{5.2}$$

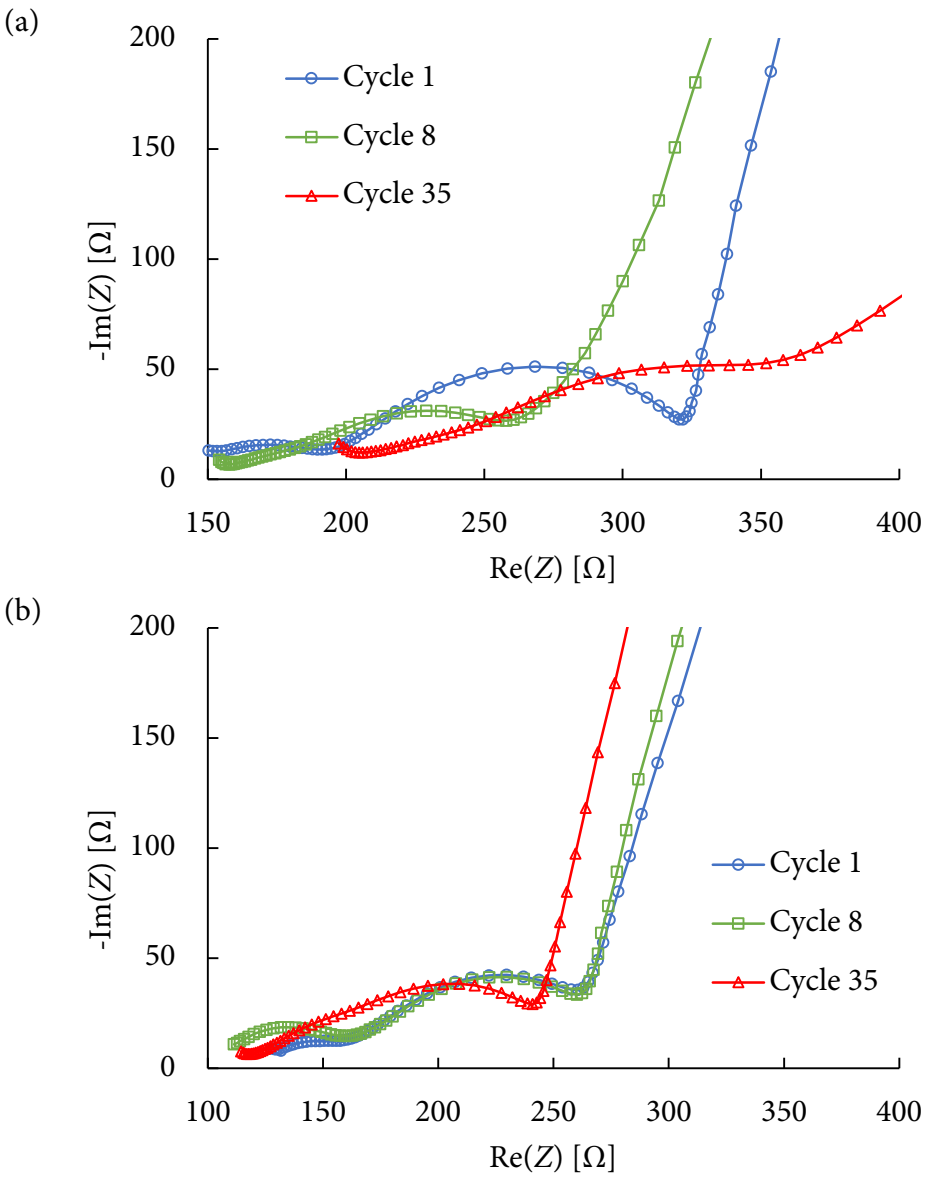

Figure 5.3: Impedance spectra of cells cycled 1, 8, and 35 times. (a) Super P cathode, (b) VGCF cathode.

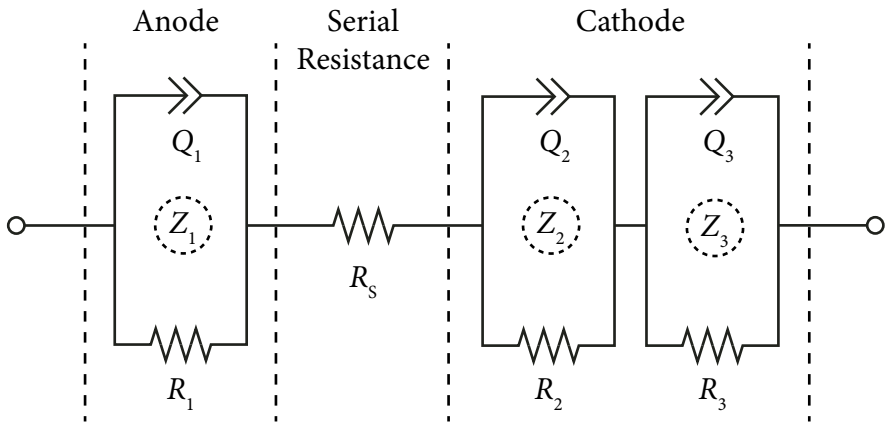

Figure 5.4: Equivalent circuit model for fitting Li–O_2 cell impedance spectra. Z_i $(i = 1, 2, 3)$ denotes the Voigt elements, which consist of a resistor (R_i) and a constant phase element (Q_i) in parallel. One Voigt element is assigned to the anode, two Voigt elements are assigned to the cathode, and the series impedances (such as the Ohmic resistance of the electrolyte) are grouped into a single resistor, R_S.

In this study, the Voigt element assigned to the cathode double layer had a typical n_i value of 0.89. Considering all elements of the equivalent circuit model, the total impedance is given by

$$Z(\omega) = R_S + \sum_{i=1,2,3} \frac{R_i}{1 + (j\omega)^{n_i} Q_i R_i} \tag{5.3}$$

which was fit to the experimental impedance spectra to minimize the difference between the modeled and experimentally measured impedances. An example of a fit is shown in a Nyquist plot in Figure B.9, with the dominant regions of each element highlighted. The Voigt elements had Q_i values on the order of 10^{-8}, 10^{-5}, and 10^{-3} F^{n_i} for Q_1, Q_2, and Q_3, respectively. Only n_3 was found to maintain a consistent value above 0.7 during cycling. Element Z_3 is also the only one whose effective capacitance is in the 1 mF to 100 mF range, which is consistent with those in previous EIS models of Li–O_2 cells that use a similar Voigt element approach to identify the part of the spectrum associated with the oxygen reduction reaction.[123,125,126] Thus, the third Voigt element, Z_3, was identified as the one most closely associated with the double layer of the carbon cathode.

The effective capacitance of the cathode was calculated for each of the impedance spectra using eq 5.2 and plotted against cycle number in Figure 5.5. Although the effective capacitance of a CPE is not well defined and should not be taken as equal to the real capacitance,[127] the values fall into the expected order of magnitude for ~1 mg of a porous carbon material, which typically have specific capacitances of 10 F g^{-1} to 100 F g^{-1}.[128] Furthermore, this method is still reliable for relative changes in capacitance for a given electrolyte/electrode interface, which this experiment aims to show. The effective capacitance of both cathode materials mirror the trend of the capacity. Both cell types experience a drop in capacity within the first few cycles, which coincides with a drop in the cathode's effective capacitance. While the effective capacitance of Super P diminishes to zero, the effective capacitance of VGCF stabilizes near 4 mF, mirroring how it reaches a stable reversible capacity by the eighth cycle. Since the effective capacitance is

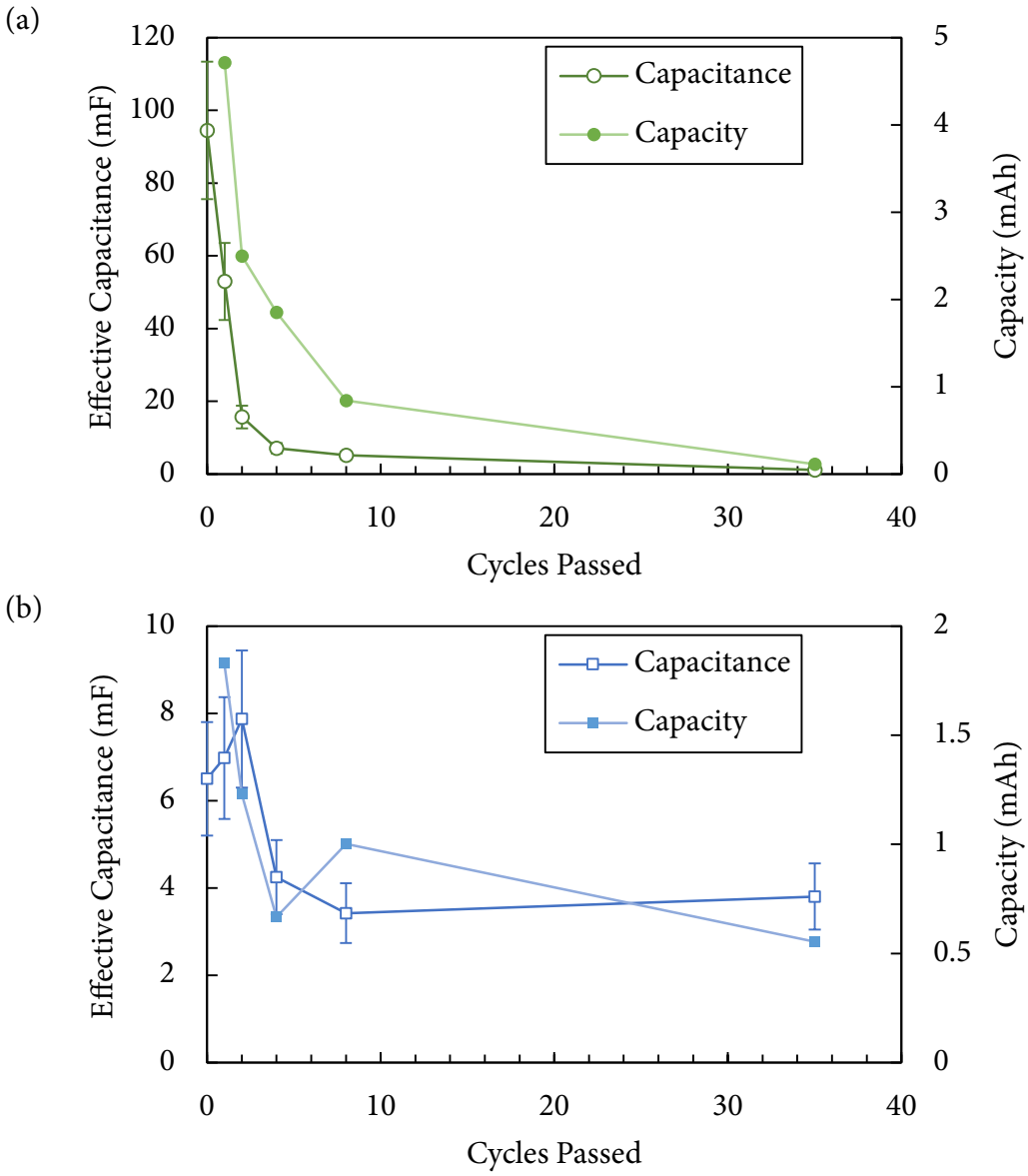

Figure 5.5: Effective capacitance of the carbon cathode and cell capacity as a function of cycles passed for (a) Super P cathode and (b) VGCF cathode. Error bars denote a 20% error on the capacitance estimate, which is typical for this technique.[120]

proportional to the cathode surface area, the decrease in the capacitance during cycling may be interpreted as the loss of surface area available for oxygen reduction.

5.1.3 Discussion

Considering that Super P and VGCF are both graphitic carbons, we believe the likeliest explanation for the irreversible loss in surface area is through a physical process rather than a chemical process. During discharge, the growth of electrically insulating Li_2O_2 particles can lead to isolation of carbon particles. Once a carbon particle is isolated from the rest of the cathode, electrons can no longer be transferred during charging to oxidize the Li_2O_2, making the isolation irreversible. The geometry of Super P is such that electronic isolation can easily occur: the carbon particles are often smaller than the Li_2O_2 particles that grow on them (see Figure B.3). Thus, it is quite reasonable that Super P particles could become entirely engulfed by Li_2O_2. VGCF, on the other hand, is 10 μm to 20 μm in length, which is longer than even the largest Li_2O_2 particles (4 μm, see Figure 4.5a). Thus, VGCF can accommodate the growth of Li_2O_2 particles while maintaining electrical contact with other fibers in the cathode.

The electronic isolation mechanism can also explain why limiting the discharge capacity, as practiced in many studies in the field, extends the cycle life of carbonaceous cathodes. In Chapter 3, we demonstrated that Li_2O_2 particles grow progressively larger during discharge until the entire cathode surface is covered (Figure 3.10). By limiting the discharge capacity, one effectively limits the size of the Li_2O_2 particles. Choosing a cutoff capacity in which Li_2O_2 is not permitted to grow to the point where it can electrically isolate the carbon particles can therefore significantly improve the reversibility of the cell. This cutoff capacity is usually 500 mAh g^{-1} to 1000 mAh g^{-1}, but is ultimately qualitatively chosen, as the choice of electrolyte and current density greatly influences the final size

of the Li_2O_2 particles.[50,69] Considering the high variability in Li_2O_2 growth morphology between specific Li–O_2 systems, implementing a capacity-limiting scheme is not a realistic technological solution to capacity fade. As demonstrated by this study, using carbon fibers to form a cathode resilient against electronic isolation can enable stable cycling of the Li–O_2 cell without the need to limit the capacity. This is a much more realistic solution to capacity fade, as it does not require the implementation of a predictive capacity-limiting cycling algorithm.

In summary, we have studied the mechanism behind capacity fade of two different carbon cathode materials, Super P and VGCF, during cycling of Li–O_2 cells. EIS analysis revealed that the decline in the cathodes' effective capacitance mirror the decline in the cells' capacity. The most probable explanation for the loss in capacitance is the irreversible physical detachment of carbon particles from the cathode matrix. We demonstrate that VGCF is capable of maintaining cathode interconnectivity for at least 35 cycles, as evidenced by the stable capacitance. Using VGCF as the cathode, a stable reversible capacity of 630 mAh g^{-1} was achieved, which is competitive with that of carbon-free cathodes. Considering that VGCF enables the long term cycling of the Li–O_2 cell without resorting to exotic materials or a capacity-limited cycling scheme, we propose the use of fibrous carbons to be a promising solution to capacity fade.

5.2 Redox Mediators

Thus far, Li_2O_2 resistivity has been discussed in detail in the context of how it limits the discharge capacity. However, given that the charging reaction also requires charge transfer, one would expect Li_2O_2 resistivity to limit rechargeability as well. Unlike the discharge reaction, Li_2O_2 is expected to decompose directly into O_2 and Li^+ during charging without

producing LiO_2 as an intermediate (eq 1.6): $Li_2O_2 \rightarrow O_2 + 2\,Li^+ + 2\,e^-$.[20] Recalling that charge transfer through Li_2O_2 by electron tunneling is limited to a 10 nm distance,[42] it follows that oxidation of Li_2O_2 should occur at the point of contact between Li_2O_2 and the cathode surface. *In situ* transmission electron microscopy (TEM) studies show that this is indeed the case: electrochemically formed Li_2O_2 particles on multiwall carbon nanotubes (MWCNTs) preferentially decompose near the carbon surface when a positive potential is applied.[129] The two main consequences of electronic resistivity are the large overpotential experienced during charging and the possibility of an incomplete recharge. The former has long been observed in galvanostatic cycling experiments, such as those shown in Section 5.1, and the latter could be quantified by chemical techniques. Hase *et al.* determined that 18% of the Li_2O_2 produced during discharge remain after charge by using an oxoammonium salt to chemically oxidize the remaining Li_2O_2.[130] Similarly, McCloskey *et al.* used an iodometric titration to determine that 10% of the Li_2O_2 remained after charge if TEGDME is used as the electrolyte solvent.[117] Incomplete electrochemical oxidation of Li_2O_2 is undesired because it leads to a lower cycleable capacity.

A promising strategy for circumventing Li_2O_2 resistivity during charge is to use a redox mediator. A redox mediator is a soluble intermediary species that can carry charge from the cathode surface to the Li_2O_2. This enables Li_2O_2 particles to be oxidized at the electrolyte-facing surfaces, even if they are no longer in electrical contact with the cathode. For a redox couple to be an effective redox mediator in the Li–O_2 cell, its oxidation potential must be greater than that of Li_2O_2, but less than the potential of the charging plateau. Even though direct Li_2O_2 oxidation is thermodynamically favored, it is kinetically easier to transfer a hole to the dissolved redox mediator, which then accepts an electron from Li_2O_2 to facilitate the oxygen evolution reaction. Bruce *et al.* first demonstrated the feasibility of this strategy by using tetrathiafulvalene (TTF) as a redox mediator in an electrolytic Li–O_2 cell with a $LiFePO_4$ anode.[86] However, this is only a proof of concept, as the $LiFePO_4$

anode was likely necessary due to the redox mediator's tendency to become parasitically reduced at the surface of a Li metal anode.[131] The next logical step in implementing this strategy is to make the redox mediators work reliably in galvanic Li–O_2 cells using Li metal anodes.

This section describes exploratory experiments aimed at improving the effectiveness of redox mediators in the Li–O_2 cell. First, TTF was tested as a redox mediator in a conventional Li–O_2 cell with a Li-metal anode to assess its mode of failure. The low-overpotential charge plateau of TTF was found to gradually diminish over many cycles, in which greater amounts of TTF added corresponds to more cycles of effective redox mediation. This suggests that shuttling of the redox mediator to the anode and its subsequent parasitic reduction may be the cause for its diminishing activity. To combat this process, I^- was tested as a redox mediator in combination with a negatively-charged ionomer membrane to block its diffusion to the anode. However, the I^- activity diminished even when a solid electrolyte was used as a barrier against I^- diffusion, implying that the mechanism for redox mediator deactivation may be occurring away from the anode surface.

5.2.1 TTF as a Redox Mediator

Coin cells were prepared with different amounts of TTF (Sigma Aldrich) to examine how the effects of a redox mediator diminish in the Li–O_2 cell. Cathodes (90% Super P and 10% PVDF) were prepared as described in Appendix A.1, and the electrolyte (1 M $LiNO_3$ in TEGDME) was prepared in a manner similar to that described in Appendix A.2, but with $LiNO_3$ in place of $LiCF_3SO_3$. A 0.25 M solution of TTF in acetone was prepared and 10 µL to 40 µL was dropped on the cathode and allowed to evaporate at room temperature. The TTF-impregnated cathodes were coated with 100 µL of lithiated Nafion dispersion in isopropanol (LITHion, Ion Power Inc.) and vacuum-dried overnight at room temperature.

The Nafion coating was intended to slow down the diffusion of TTF from the cathode to the anode. A TTF-spiked electrolyte was also prepared by adding 20.44 mg TTF per milliliter of electrolyte, which creates a 100 μM solution. Coin cells were assembled and prepared for testing on a Neware BTS–5V1mA battery tester as described in Appendix A.3-A.4. Cells were discharged at a constant current of 0.2 mA to a capacity of 0.6 mAh, followed by a 30 min rest at open-circuit, then charged at a constant current of 0.2 mA to zero capacity, followed by another 30 min rest at open-circuit. Since the goal of this study is to evaluate redox mediator activity, a capacity-limited scheme was chosen such that the effects of capacity fading do not interfere with redox mediator fading.

Figure 5.6a shows the voltage curves of the first seven discharge-charge cycles for a cell containing 6.0 mmol of TTF dissolved in the electrolyte. Initially, a charge plateau of 3.5 V (vs Li/Li^+) was achieved, which is equal the oxidation potential of TTF to TTF^+.[86] However, the low-voltage charge plateau quickly vanishes within the next three cycles, indicating that a decreasing amount of TTF is being oxidized with increasing cycle number. After seven cycles, the charge voltage becomes nearly indistinguishable from a cell without redox mediator. Although the $LiNO_3$-based electrolyte was originally intended to extend redox mediator activity by forming a stable solid-electrolyte interphase (SEI) on the Li-metal anode,[132] the effects of the redox mediator continue to diminish. This implies that the SEI is either reactive towards TTF/TTF^+ or is ineffective against preventing electrochemical TTF^+ reduction at the anode.

Plotting the charge plateau voltage as a function of cycle number allows us to compare how well redox mediation activity is sustained for a given amount of TTF (Figure 5.6b). With just 2.0 μmol of TTF, the redox mediator effects wear off by the third cycle. Increasing the amount of TTF nearly five-fold to 9.8 μmol only extends redox mediator activity by two additional cycles. In all cases, the charge voltage approaches a steady state value of

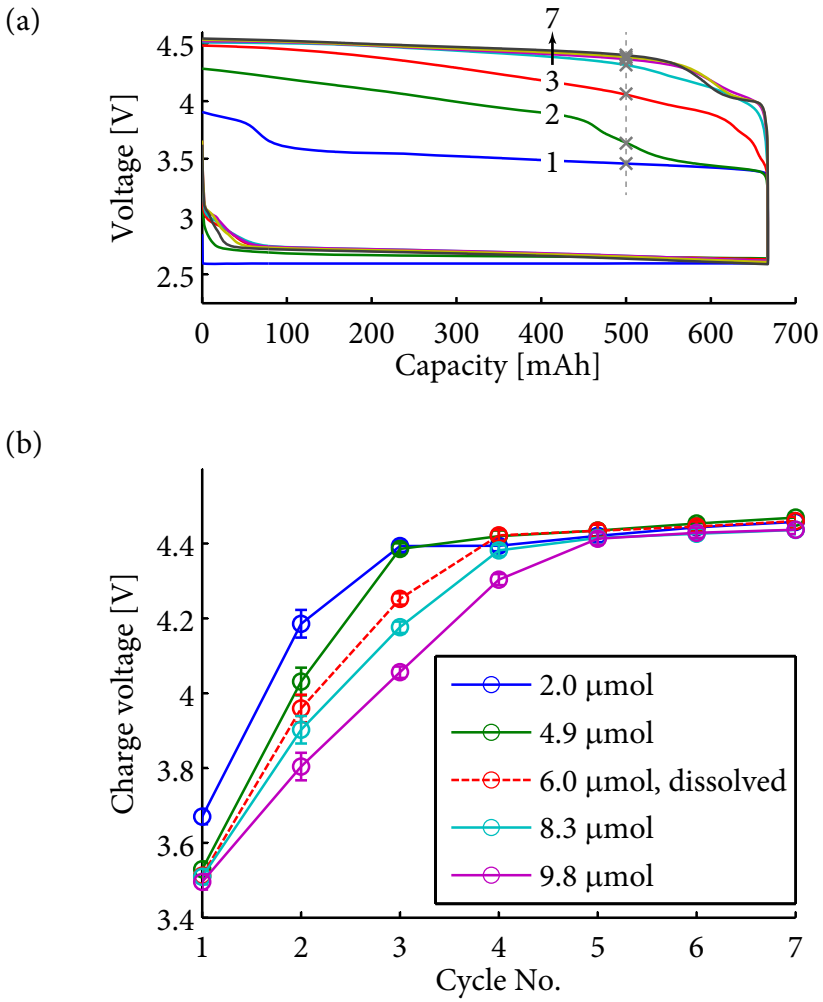

Figure 5.6: (a) Voltage curves of first seven discharge-charge cycles for a cell containing 6.0 µmol of TTF dissolved in the electrolyte. Dotted line indicates the capacity where the voltage was recorded for the charge voltage versus cycle number plots in b. (b) Charge plateau voltage as a function of cycle number for cells with different amounts of TTF added. TTF is impregnated into the cathode, except for the 6.0 mmol cell, which had TTF dissolved into the electrolyte. All cathodes were coated with lithiated Nafion. Error estimate given by the difference between duplicate 4.9 µmol test cases.

approximately 4.4 V by the fifth cycle, by which the redox mediator effects have diminished. No improvement in retention of redox mediator activity was achieved by impregnating the cathodes with TTF instead of pre-dissolving it into the electrolyte, indicating that the dissolution of TTF is not rate-limiting. The slight increase in activity retention brought forth by increased TTF suggests that the redox mediator activity diminishes through a parasitic mechanism. This follows from the logic that a greater amount of TTF in the cell will require more cycles or time to deplete. If the shuttling hypothesis holds true and the parasitic reaction occurs at the anode, keeping the redox mediator confined to the cathode side should help prolong its activity. Thus, we looked towards methods that can selectively block the redox mediator from shuttling to the anode.

5.2.2 LiI as a Redox Mediator

The I^-/I_3^- redox couple has been used for quite some time to transfer charge in dye-sensitized solar cells.[133] Its standard potential is 0.54 V versus the normal hydrogen electrode (NHE), which corresponds to 3.58 V versus Li/Li^+.[63] This makes it a favorable candidate as a redox mediator in the Li–O_2 cell because it is above the Li_2O_2 redox potential of 3.10 V, yet below the typical charge plateau voltage of the cell due to the high charging overpotential. The negative charge of the I^-/I_3^- redox couple also enables the use of a negatively charged ionomer film to act as a selective barrier against its crossover from the cathode to the anode.

To test whether a barrier would aid in prolonging redox mediator activity, coin cells were fabricated using two separators–one for the anode and one for the cathode–that are partitioned by a barrier. Super P cathodes and 1 M $LiCF_3SO_3$ in TEGDME electrolyte were prepared as described in Appendix A.1 and A.2. A LiI-spiked electrolyte was also prepared by dissolving 13.39 mg of LiI (anhydrous, beads, –10 mesh, Sigma-Aldrich) per milliliter

of electrolyte to create a 100 mM solution of LiI. Coin cells were constructed according to Appendix A.3, except the Whatman GF/D separator was replaced with a sandwiched separator consisting of Whatman GF/A on the anode side, a lithiated Nafion film in between, and Whatman 934-AH on the cathode side. These separators were selected because their thicknesses (260 μm and 435 μm for GF/A and 934-AH, respectively) add up approximately to the thickness of a GF/D separator (675 μm). 25 μL of the unspiked electrolyte was added to the GF/A separator, while 40 μL of the LiI-spiked electrolyte was added to the 934-AH separator. Control cases were also prepared, in which the Nafion film and/or LiI was omitted.

Nafion film (NRE–212) was lithiated following an ion-exchange procedure in an LiOH solution. First, the films were punched into 3/4-inch circles. The ion-exchange solution was 1 M LiOH in a 50:50 mixture of water and ethanol, heated to 80 °C. The Nafion circles was soaked into the LiOH solution for 12 h. Afterwards, the Nafion circles were rinsed in boiling deionized water, sandwiched between two Whatman GF/D separators to prevent curling, and dried in vacuum at 120 °C overnight. The dried lithiated Nafion films were used in coin cell assembly, as described above. The coin cells were prepared for testing according to Appendix A.4 and cycled at a constant current of 0.2 mA (0.1 mA cm^{-2}) with 30 min of rest after each discharge and charge step.

LiI was found to function appropriately as a redox mediator by lowering the charge plateau overpotential. Figure 5.7 compares the voltage curves of a cell with and a cell without LiI. The cell with LiI exhibited a first-cycle charge voltage of ∼3.75 V, which is approximately 0.55 V lower than that of the cell without LiI. However, similar to the case with TTF, the redox mediation effects of LiI diminished over several cycles. A Nafion barrier, unfortunately, yielded no significant improvement in prolonging redox mediator activity. As seen in Figure 5.8, the voltage curves of a cell with the Nafion barrier is

(a)

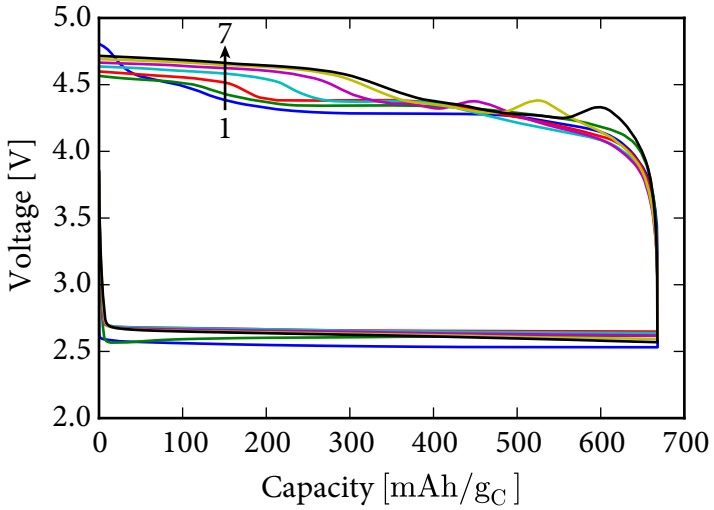

(b)

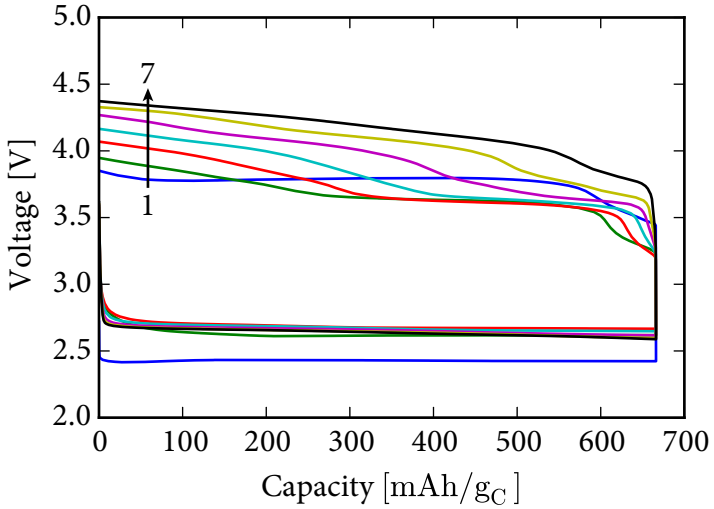

Figure 5.7: Voltage curves of cells without (a) and with (b) 40 µmol of LiI added.

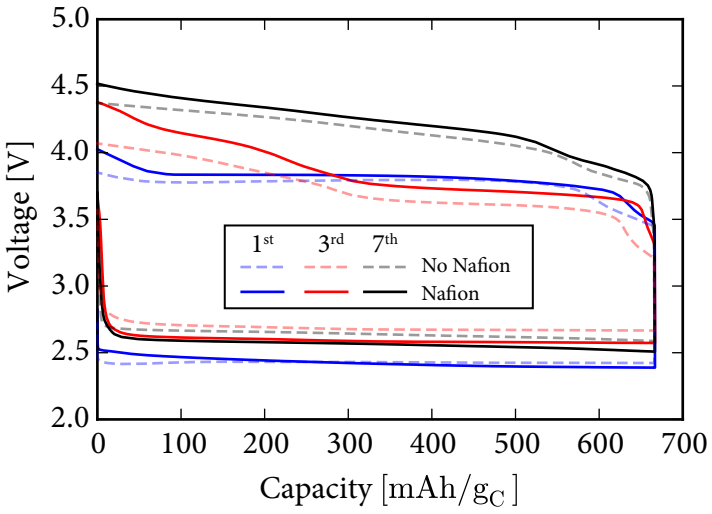

Figure 5.8: Voltage curves of cells with and without a Nafion separator, using 40 µmol of LiI as a redox mediator.

nearly identical to that of a cell without it. The only difference is a slight increase of the overpotential for both the discharge and charge plateaus, which is likely the result of extra ionic resistance introduced by the Nafion film. The ineffectiveness of Nafion in prolonging redox mediator activity can either be a result of the unsuccessful blocking of I^-/I_3^- shuttling or the presence of a depletion mechanism that does not require I^-/I_3^- to shuttle to the anode. In the Li–S cell, Nafion was previously shown to successfully suppress the shuttling of anionic polysulfide species to a limited extent.[134–137] Since I^-/I_3^- is not as large as the polysulfide anions, it is possible that diffusion is mainly suppressed by steric exclusion rather than charge repulsion. If this is the case, using a solid electrolyte to completely block the transport of I^-/I_3^- to the anode should yield an improvement in redox mediator activity.

To completely block the transport of I^-/I_3^- to the anode, the Nafion film was replaced with a lithium ion conducting glass ceramic (LICGC, Ohara Corporation). LICGC is a Li-replaceable NASICON-type solid electrolyte with an ionic conductivity of 1.0×10^{-4} S cm^{-1} at room temperature.[138] The LICGC separator had a negligble impact on the performance of the cell, as evidenced by the nearly identical voltage curves (Figure B.10). Unfortunately, the LICGC also does little in extending redox mediator activity in the cell, as shown in Figure 5.9. As a solid electrolyte, LICGC is expected to block the transport of all species except for Li^+ ions. The fact that the redox mediator activity still rapidly diminishes suggests that a mechanism other than shuttling is responsible for the depletion of LiI.

A *post mortem* inspection of the cell components revealed dark brown stains on the separators (Figure B.11). No color was observed during the preparation of the LiI-spiked electrolyte prior to cycling, which suggests that the colored deposits were generated during electrochemical testing. Indeed, it is well known that I_3^- has a brown to blue-black color

(a)

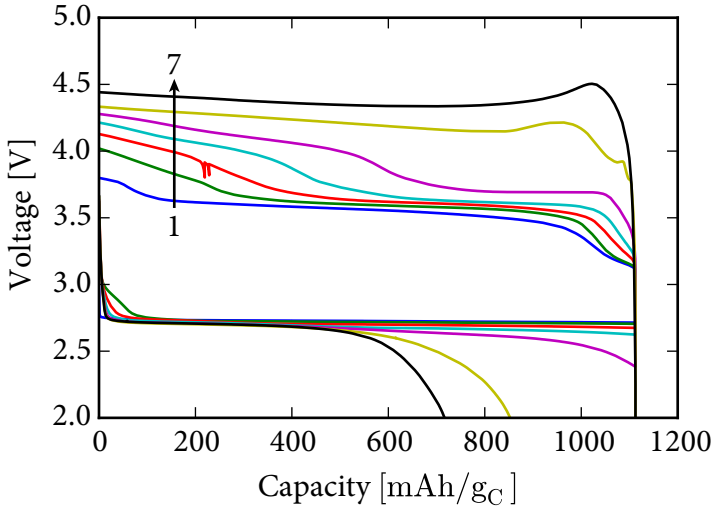

(b)

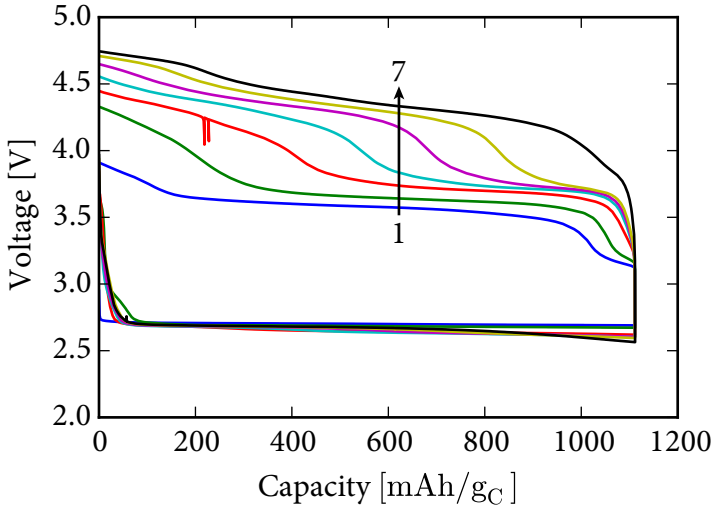

Figure 5.9: Voltage curves of cells without (a) and with (b) a LICGC separator, using 40 µmol of LiI as a redox mediator.

depending on the solvent and the species it may be complexed with.[139] During the charge step, the accumulation of I_3^- may drive its precipitation out of solution and onto the surfaces of the separator. Most of the brown staining occurs on the cathode-side separator, but a brown ring can also be seen on the anode-side. While LICGC itself is impermeable to I^-/I_3^-, some I_3^- appeared to have crept around the LICGC disk due to the incomplete coverage of the wetted area. Despite the incomplete blocking of I^-/I_3^-, better capacity retention was achieved with LICGC than without it, which could be seen in the discharge portion of the voltage curves in Figure 5.9. The rapid loss of discharge capacity of the cell without LICGC may be due to the deposition of I_3^- onto the surface of the anode, leading to its passivation. The cell with LICGC did not experience rapid capacity fade, possibly due to the slower transport of I_3^- to the anode.

5.3 Recommendations for Further Study

The experiments described in this chapter provide opportunities to improve the rechargeability of the Li–O_2 cell. However, many questions are still left unanswered, especially with regard to redox mediators. For instance, the mechanism of redox mediator depletion has yet to be definitively determined. Blocking the diffusion of LiI to the anode with Nafion or LICGC yielded no apparent improvement in prolonging redox mediator activity, suggesting that the mechanism of deactivation may not be occurring at the anode. If precipitation of the redox mediator turns out to be the primary mechanism of depletion, then the solid species should be detectable on the cathode or separator surfaces using spectroscopic techniques. Furthermore, the mechanism of capacity fade in the presence of LiI is not completely clear either. The LICGC's apparent ability to protect against capacity fade suggests it may be due to passivation at the anode, but the shape of the fading discharge curves are qualitatively similar to those due to cathode deterioration described in

Section 5.1. The problematic electrode can theoretically be identified by replacing it during cycling, which should restore the discharge capacity. Such a technique has previously been used to identify anodic corrosion as a limiting process in certain Li–O_2 and K–O_2 systems.[140,141] In addition, a structurally resilient cathode material, such as VGCF, can be used to rule out the effects of cathode deterioration. Using VGCF in place of Super P for redox mediator experiments would therefore allow for a more controlled study and show how the redox mediators behave when subjected to complete cycles.

The need for additional studies is driven by the lack of knowledge about side reactions involving the redox mediators. Recently, it was determined that high concentrations of LiI can change the dominant reaction product from Li_2O_2 to LiOH.[142,143] The mechanism of this reaction is not well understood. Sun *et al.* propose that it involves the decomposition of ether-based solvents,[142] while Grey *et al.* propose that trace water in the electrolyte supplies the H^+ necessary for LiOH formation.[143] Although LiI has been of particular interest due to its low cost, other candidates, including organosulfurs (*e.g.* TTF) and nitroxides (*e.g.* $TEMPO^+$), are worth investigating to compare their chemical stability and ability to remain active in solution. A suitable redox mediator, when combined with a robust cathode, can lead to a Li–O_2 cell that can cycle stably with a low charging overpotential. This type of cell, rather than one with a high first-cycle capacity but poor rechargeability, provides a better foundation for developing a practical Li–O_2 cell.

CHAPTER 6

CONCLUDING REMARKS

The Li–O_2 battery is an enticing energy storage platform due to its high theoretical specific energy, but has several problems that must be solved before it can transition from the research stage to commercial development. These problems affect all components of the cell—the anode, cathode, and electrolyte—and contribute to a battery that runs below the theoretical specific energy with limited rechargeability. Despite the wide variety challenges, one can prioritize them based on their fundamental applicability to the Li–O_2 cell reaction. In this thesis, we identified the intrinsic problems as those that stem from the formation of Li_2O_2. Through experimental characterization and theoretical modeling, we develop a mechanistic understanding of how Li_2O_2 formation limits Li–O_2 cell performance and demonstrate possible solutions based on these findings.

We started with a critical evaluation of O_2 diffusion in the cathode. Pulsed discharge experiments showed that the addition of rest periods to the discharge process does not improve the capacity. This contradicts the notion that the Li–O_2 cell capacity is O_2 transport limited, where rest periods should allow the oxygen concentration to replenish, thus enhancing the capacity. A quantitative analysis of the oxygen transport rate was accomplished by measuring the voltage response of the cell during the introduction of oxygen. Using a relationship derived from the Nernst equation and Fick's laws of diffusion, we find that the rate of oxygen transport is moderately reduced, corresponding to 57% of the available void volume filled. Again, this contradicts expectations for a transport-limited cathode, where 93% of the void volume need to be filled to stop discharge. From these experiments, we conclude that oxygen transport is not a limiting factor under the conditions in which we tested the cells.

However, it was clear that some other mechanism is still responsible for limiting the

discharge capacity based on the sudden drop in voltage at the end of the discharge curve. Next, we considered the effect of electrical resistivity of Li_2O_2. Simple models of electrical resistivity, *e.g.* Ohm's law, have failed to explain the shape of the discharge curve and the large size of the Li_2O_2 particles, which exceeds the length allowed by conduction through Li_2O_2. We suspect that this discrepancy between the models and experiments is due to the assumption that Li_2O_2 deposits as a uniform layer. Thus, we developed a new model to simulate a non-uniform layer, in which discrete Li_2O_2 particles nucleate and grow on the cathode surface. By doing so, the overpotential becomes dependent on the surface coverage of Li_2O_2 on the cathode, which closely fits the voltage curves from galvanostatic discharge experiments. A relationship between current density and discharge capacity is also demonstrated on the basis of particle nucleation: higher current density drives higher nucleation rate, which leads to faster crowding of Li_2O_2 particles on the cathode surface.

The findings from the nucleation and growth model suggest that one can maximize the capacity for a given amount of cathode surface area by minimizing the nucleation rate. We explored two possible strategies to kinetically reduce the nucleation rate: using electrolytes that chelate Li^+ and using an open cathode structure to provide a reservoir for LiO_2. A molecular dynamics simulation of superoxide deposition on a carbon cathode in a TEGDME electrolyte revealed that TEGDME molecules form a solvation barrier by coordinating with Li^+ ions adsorbed on the surface of the carbon. Interestingly, this barrier only exists when there is the carbon is negatively charged, corresponding to a negative overpotential, such as during discharge. To test the effects of an open cathode structure, we changed the carbon material from Super P to VGCF, which has continuous channels between the fibers rather than pore spaces between packed spherical particles. VGCF cathodes produced a higher capacity than expected for their low surface area. Unusually large ~4 μm particles of Li_2O_2 were also formed, suggesting a lower nucleation rate. A theoretical model demonstrated that an open cathode structure reduces the nucleation

rate through the diffusion and slow accumulation of LiO_2, whereas a closed structure results in a nearly immediate onset of nucleation because the LiO_2 concentration quickly rises to steady state.

The growth of Li_2O_2 particles also implies challenges to rechargeability. Carbon cathodes are traditionally seen to rapidly lose capacity when subjected to complete (voltage-limited) cycling in Li–O_2 cells. As such, the practice of capacity-limited cycling became widespread, while research efforts turned towards the development of carbon-free cathodes. However, we proposed that capacity fading is due to the physical separation of carbon particles from the conductive matrix and used EIS measurements of cycled to test this hypothesis. The effective capacitance of the cathode, which is proportional to its surface area, was found to decrease as a function of cycle number. This decrease in capacitance mirrors the decrease in capacity, suggesting that the disconnection of carbon particles from the cathode is responsible for the loss in capacity. For a cathode composed of small carbon particles, such as Super P, this mechanism eventually leads to a complete loss of cycle capacity. A VGCF cathode, however, was able to maintain a stable capacity of 630 mAh g^{-1}, which is competitive with those achieved by carbon-free cathodes. The high aspect ratio of VGCF likely improves its resilience against Li_2O_2 particle growth by lowering its electronic percolation threshold.

Another challenge invoked by the growth of large Li_2O_2 particles is being able to completely oxidize all of the Li_2O_2 during charging, especially when the particle size exceeds the electron transport length. Soluble redox mediators are recommended as a method to reach these out-of-contact Li_2O_2 fragments and achieve a complete charge. Preliminary experiments using TTF and LiI as a redox mediators show that the activity of the the mediator diminishes with each cycle, as shown by the shortening of the low-overpotential charge plateau. Suspecting that this is due to the crossover of the redox

mediator to the anode, we tested a Nafion ionomer barrier and a solid Li^+ conducting glass ceramic to keep I^-/I_3^- on the cathode side. However, the activity continued to diminish, even for the solid separator, which is impenetrable by I^-/I_3^-. The mechanism of redox mediator depletion therefore must occur on the cathode side. Images of the separator after cycling suggest that the precipitation of I_3^- may be depleting the activity of the redox couple in solution. This research is ongoing, and an inquisitive experimental approach should be adopted for future studies to identify how the redox mediator activity diminishes.

In conclusion, the formation of Li_2O_2 limits both the discharge capacity and the rechargeability of the Li–O_2 cell. A combined theoretical and experimental approach was essential in determining the underlying limiting mechanisms. Theoretical models provide a means of quantitative analysis of experimental data under the framework of a proposed hypothesis. Although the effects of oxygen transport and charge transport limitations can elicit qualitatively similar discharge curves, pairing the experiments with models allowed us to distinguish the effects of one from the other and determine that charge transport limits Li_2O_2 capacity by means of heterogeneous particle growth. This knowledge proved valuable in identifying strategies to improve the discharge capacity and rechargeability. Ultimately, a proposed solution must solve a problem that actually exists in the Li–O_2 cell for it to be useful. For this reason, fundamental research and characterization of failure mechanisms continue to be a vital part of Li–O_2 cell development. Even as trial-and-error studies in the field decline, systematic studies are becoming more prevalent. Thus, one can be hopeful that more efficient research efforts will lead to the development of a practical Li–O_2 cell sooner rather than later.

APPENDIX A

EXPERIMENTAL PROTOCOLS

This section describes protocols used by multiple experiments in this dissertation.

A.1 Carbon Electrode Preparation

A.1.1 Super P

A cathode slurry was prepared by mixing 90 wt% of Super P®Li carbon (Imerys Graphite & Carbon), with 10 wt% of polyvinylidene fluoride (PVDF, Sigma-Aldrich), then adding 900 mg of n-methyl-2-pyrrolidone (NMP, Sigma-Aldrich) for every 100 mg of combined solid weight. The slurry contents were mixed in a ball mill (Fritsch PULVERISETTE 23) at 50 Hz for at least 20 minutes. The slurry was coated on a sheet of carbon paper (Toray TGP-H-030) with a doctor blade set to a height of 80 µm. The coated carbon paper was dried at 100 °C under vacuum for 12 hours and transferred into an argon-filled glovebox (O_2 < 0.2 ppm, H_2O < 1.0 ppm; Innovative Technology) without exposure to air. 5/8-inch (15.88 mm) diameter disks were punched from the carbon paper to form the individual coin cell cathodes. The weight of the active layer (total weight minus carbon paper weight) averaged (1.0 ± 0.1) mg.

A.1.2 Vapor Grown Carbon Fiber

Vapor grown carbon fiber (VGCF) cathodes were prepared in a method similar to that of the Super P cathodes, but with less NMP per solid weight to maintain a similar consistency for spreading. A cathode slurry was prepared by mixing 90 wt% of VGCF-H (Showa

Denko K.K.), with 10 wt% of PVDF, then adding 900 mg of NMP for every 100 mg of combined solid weight. The slurry contents were mixed in a ball mill at 50 Hz for at least 20 minutes. The slurry was coated on a sheet of Toray carbon paper with a doctor blade set to a height of 80 µm. The coated carbon paper was dried at 100 °C under vacuum for 12 hours and transferred into an argon-filled glovebox (O_2 < 0.2 ppm, H_2O < 1.0 ppm) without exposure to air. 5/8-inch (15.88 mm) diameter disks were punched from the carbon paper to form the individual coin cell cathodes. The weight of the active layer (total weight minus carbon paper weight) averaged (1.0 ± 0.1) mg.

A.2 Electrolyte Preparation

Electrolyte components were dried for 24 hours and stored in the argon-filled glovebox prior to use. The salt, trifluoromethanesulfonate ($LiCF_3SO_3$; Sigma-Aldrich), was dried at 100 °C under vacuum and the solvent, tetraethylene glycol dimethyl ether (TEGDME; Sigma-Aldrich), was dried over 3 Å molecular sieves. The electrolyte, a 1.0 M $LiCF_3SO_3$ solution in TEGDME, was prepared by mixing with a Teflon-coated stir bar.

A.3 Coin Cell Assembly

A 1/2-inch (12.7 mm) diameter hole was punched in the top (cathode) side of each CR2032 case (Pred Materials). The following components were added in sequence:

1. Stainless steel wire cloth disk, 3/4-inch (19 mm) disk diameter, 0.0055-inch (0.140 mm) wire diameter (McMaster-Carr).
2. The cathode disk, prepared as described in appendix A.1.

3. Whatman GF/D glass fiber separator, 3/4-inch (19 mm) diameter.
4. Electrolyte, prepared as described in section 2.
5. Lithium metal, 0.77 mm thick (Alfa Aesar), punched to 1/2-inch (12.7 mm) diameter.
6. Stainless steel spacer disk, 15.5 mm diameter, 0.5 mm mm thick.
7. Stainless steel wave spring (MTI Corporation).

The polypropylene gasket and the bottom (anode) side of the CR2032 case were added to complete the assembly, which was crimped to a pressure of 14 MPa using a hydraulic coin cell crimper (BT Innovations). It should be noted that the electrolyte was dropped only at the center of the separator; we found that attempting to spread the electrolyte over the entire separator introduced inconsistencies in wetting. In addition, the electrolyte-facing side of the lithium metal foil was scraped with a spatula prior to use to remove surface oxides and impurities.

A.4 Testing Environment

Testing was performed in a custom-built hermetically sealed chamber, shown in Figure B.1. The cells were loaded into the main chamber while in the glovebox. The entire apparatus was purged with oxygen (99.999% purity, Airgas) for 15 minutes, then adjusted such that the main test chamber was regulated at a pressure of 1.3 atm. An external oxygen supply tank, initially at 250 psi (1724 kPa), ensured that the system was kept at positive pressure at all times. The cells were allowed to equilibrate for at least 3 hours prior to electrochemical testing. No significant drop in pressure was observed throughout the duration of the tests.

A.5 Scanning Electron Microscopy

Discharged cells were disassembled inside the glovebox, and the cathodes were removed and transported to the scanning electron microscope (Zeiss LEO 1550 Field Emission SEM) within an airtight container. The cathodes were loaded onto the stage in the presence of a nitrogen stream. Due to the tendency of Li_2O_2 to decompose under the electron beam, a low accelerating voltage of 2.0 kV was used, and an aperture size of 20 μm was used to reduce the beam current. Images were taken with a single pass after focusing on a nearby region.

A.6 X-ray Diffraction

Cathodes were mounted on a glass microscope slide inside an argon-filled glovebox and coated with paraffin oil to protect them from air during the x-ray diffraction (XRD) measurements. Measurements were done on a Bruker D8 Discover x-ray diffractometer employing Cu-Kα radiation (λ = 1.5406 Å) and fitted with a 2-dimensional detector. Frames were captured with an exposure time of 10 minutes, after which they were integrated along χ (the polar angle orthogonal to 2θ) to yield an intensity vs 2θ plot.

APPENDIX B

ADDITIONAL FIGURES

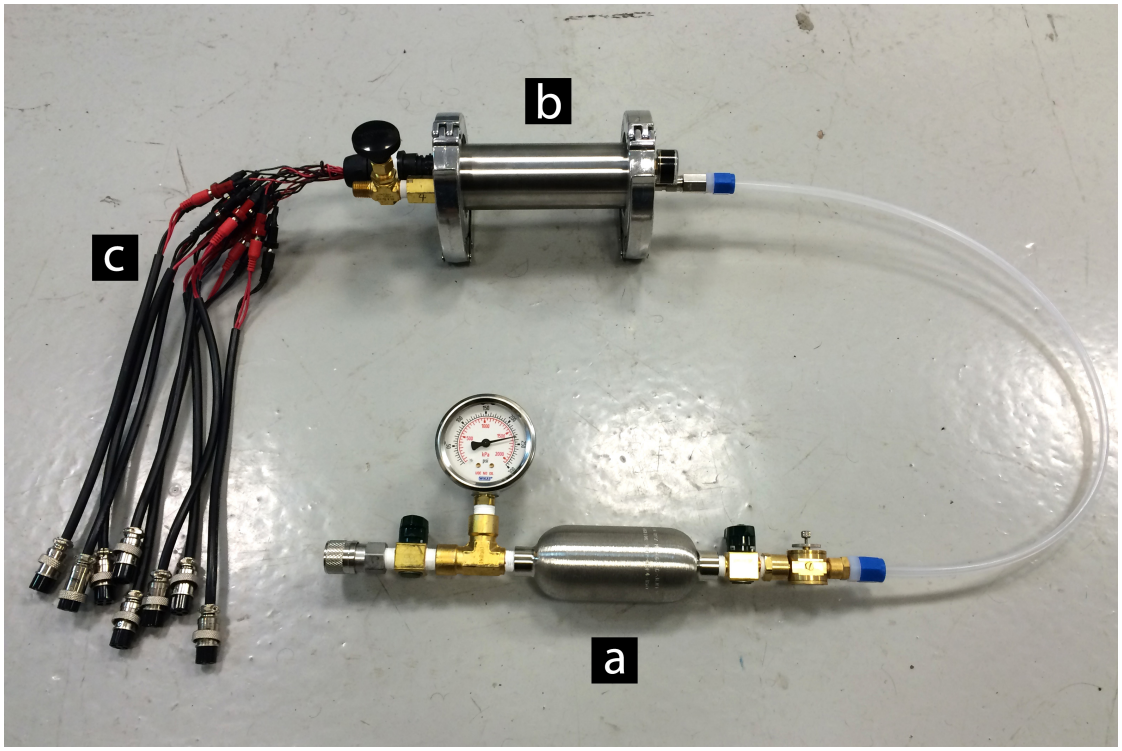

Figure B.1: Li–O_2 cell test chamber. (a) External oxygen tank. (b) Main chamber with coin cells. (c) Electrical connectors to battery test channels.

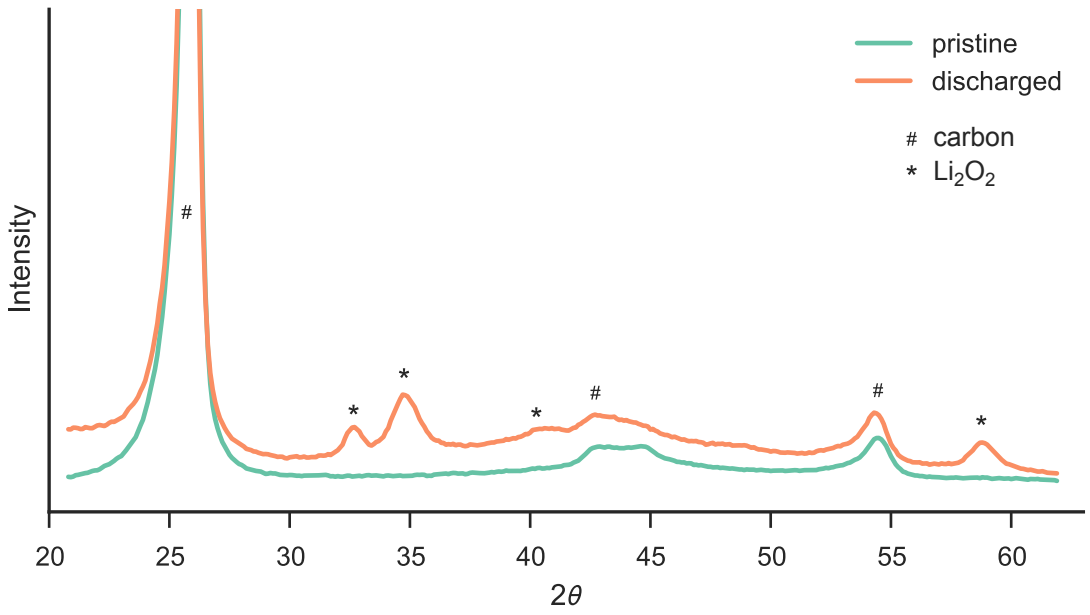

Figure B.2: XRD of cathode from discharged cell (i_{geo} = 10 µA cm^{-2}, 2.0 V cutoff). No significant peaks besides those for Li_2O_2 were observed.

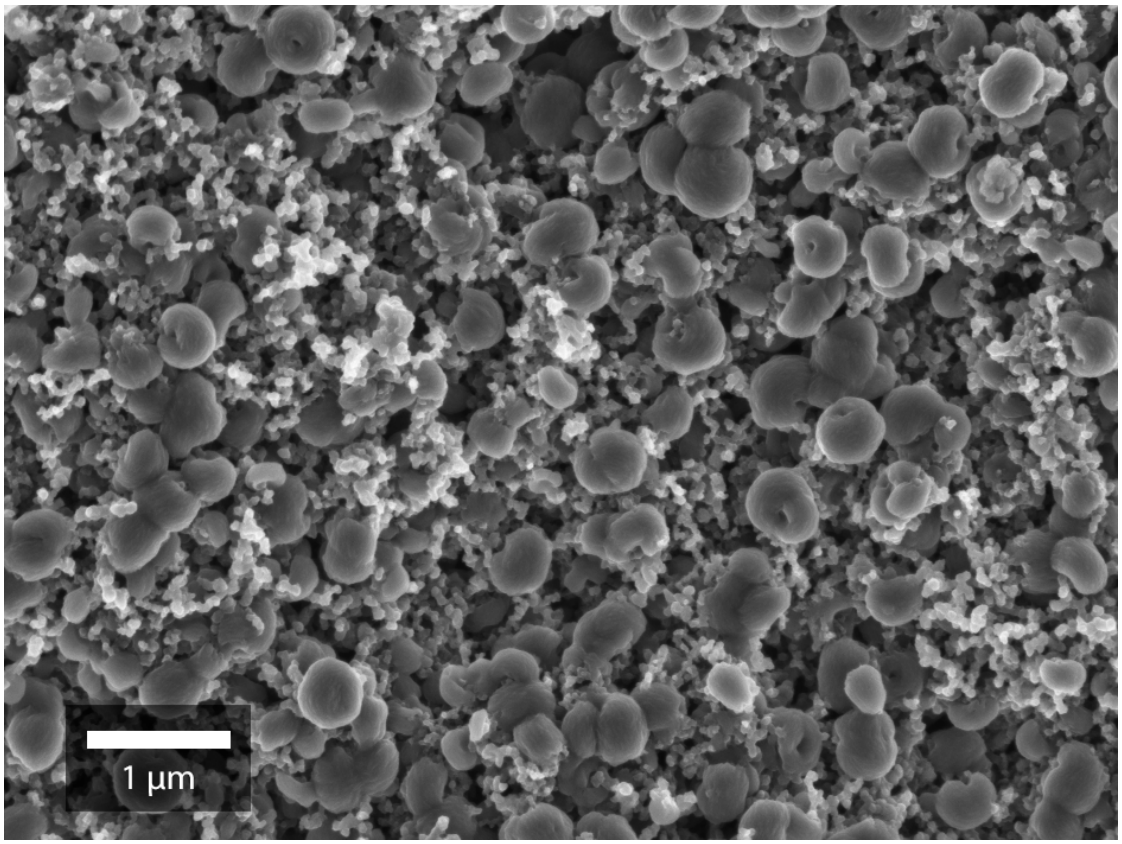

Figure B.3: SEM image of a cathode partially discharged at 2.5 µA cm^{-2}.

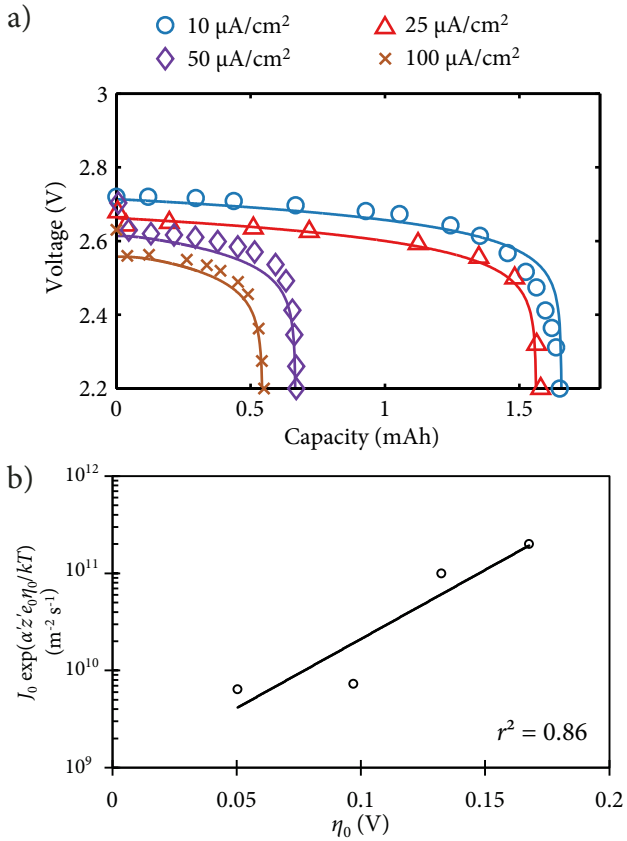

Figure B.4: (a) Simulated (lines) and experimental (symbols) discharge curves for a Li–O_2 cell with XC-72 cathode from Nazar *et al.*[50] (b) Plot to obtain J_0 and α'.

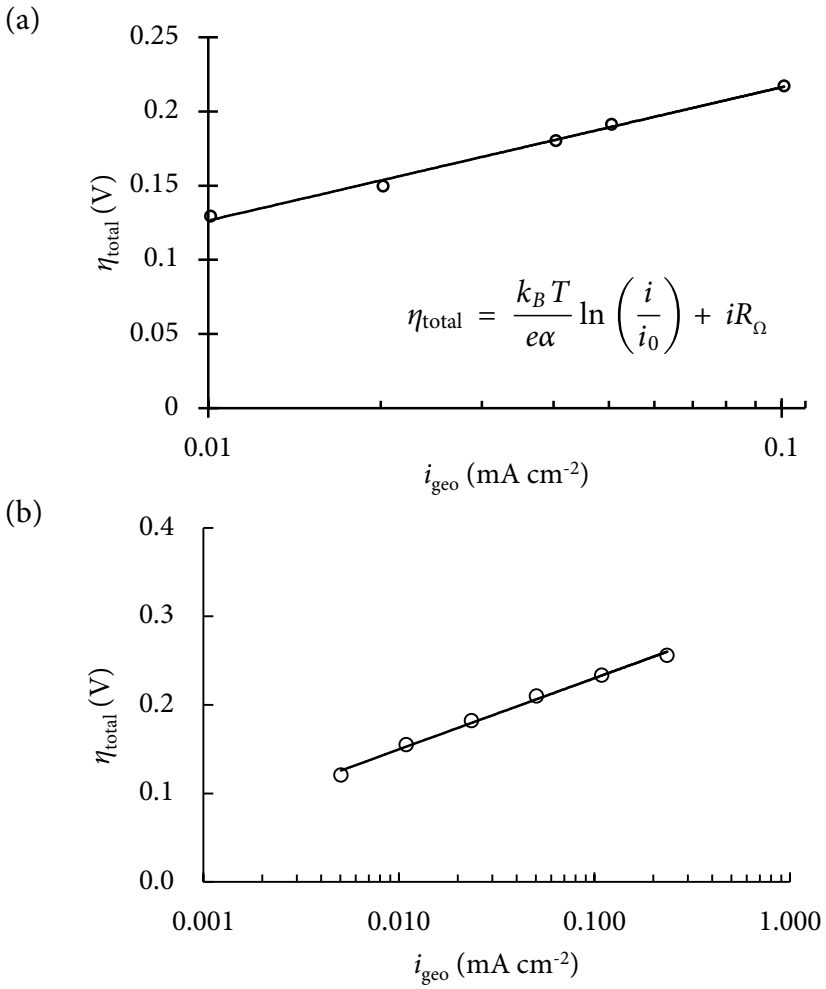

Figure B.5: Tafel plot of onset potentials and corresponding fit to *iR*-corrected Tafel equation. (a) Super P cathodes, $\alpha = 0.656$, $i_0 = 3.7 \times 10^{-4}$ mA cm$^{-2}_{\text{geo}}$, and $R_\Omega = 624\,\Omega\,\text{cm}^2$; (b) VGCF cathodes, $\alpha = 0.548$, $i_0 = 3.8 \times 10^{-5}$ mA cm$^{-2}_{\text{geo}}$, and $R_\Omega = 650\,\Omega\,\text{cm}^2$

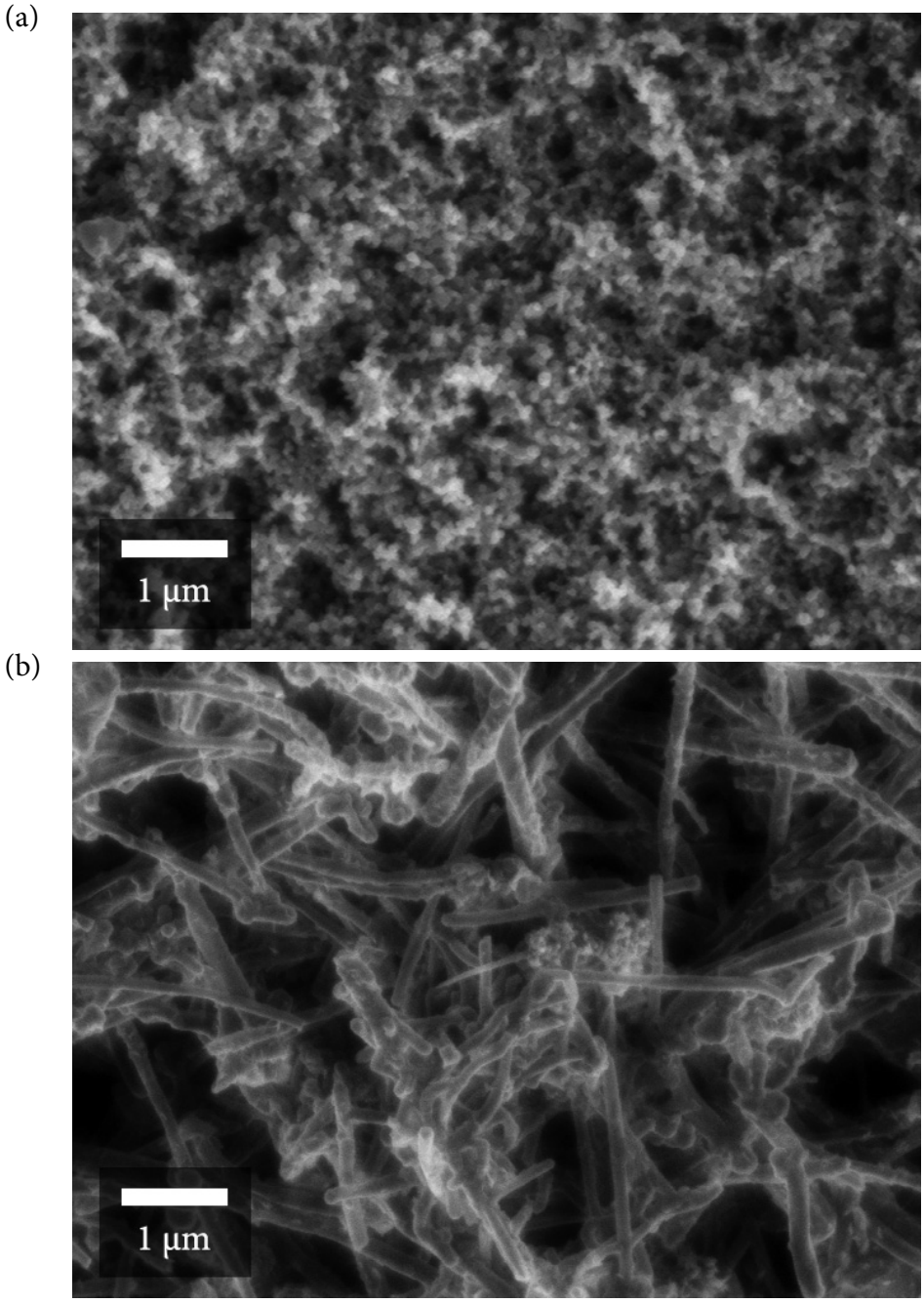

Figure B.6: SEM images of pristine (undischarged) cathodes: (a) Super P and (b) VGCF.

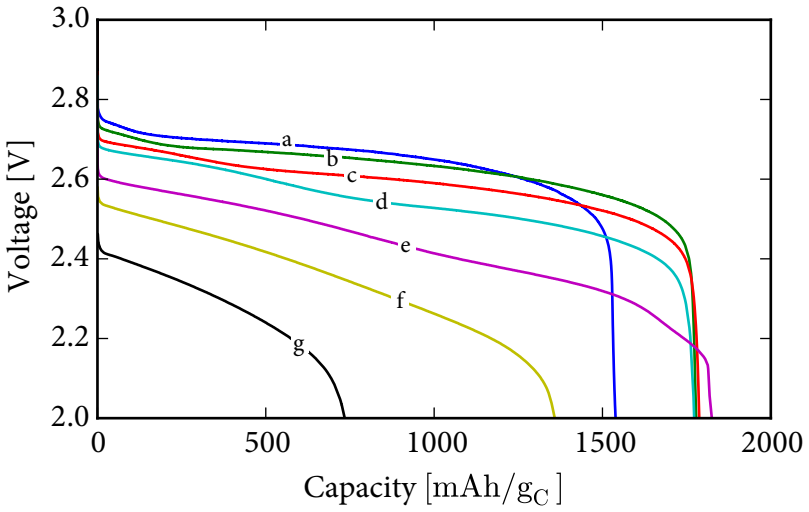

Figure B.7: Supplementary discharge curves of cells with VGCF cathodes discharged at geometric current densities of (a) 5.1 µA cm^{-2}, (b) 10.9 µA cm^{-2}, (c) 23.5 µA cm^{-2}, (d) 50.5 µA cm^{-2}, (e) 108.8 µA cm^{-2}, (f) 234.5 µA cm^{-2}, (g) 505.2 µA cm^{-2}.

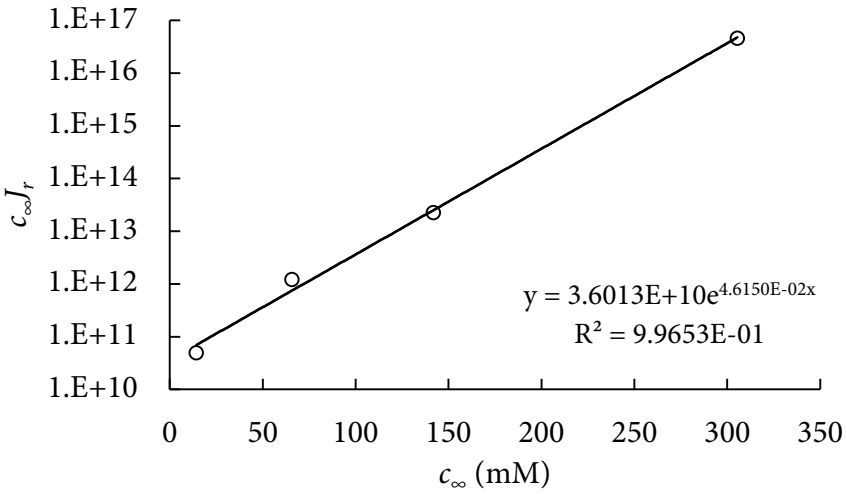

Figure B.8: Fit of residual nucleation rate to empirical supersaturation equation (eq 4.14).

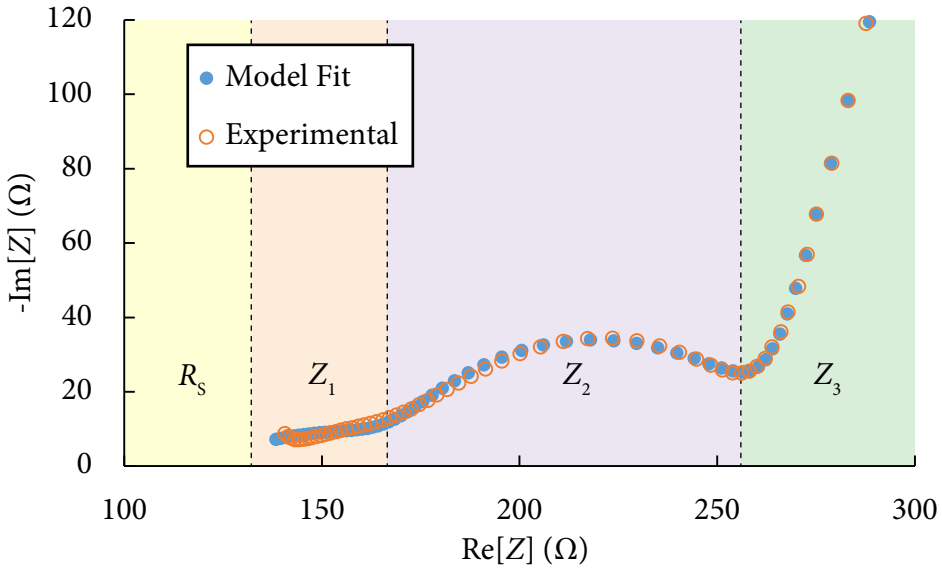

Figure B.9: Fit to impedance spectrum of a cell with a Super P cathode after four discharge/charge cycles.

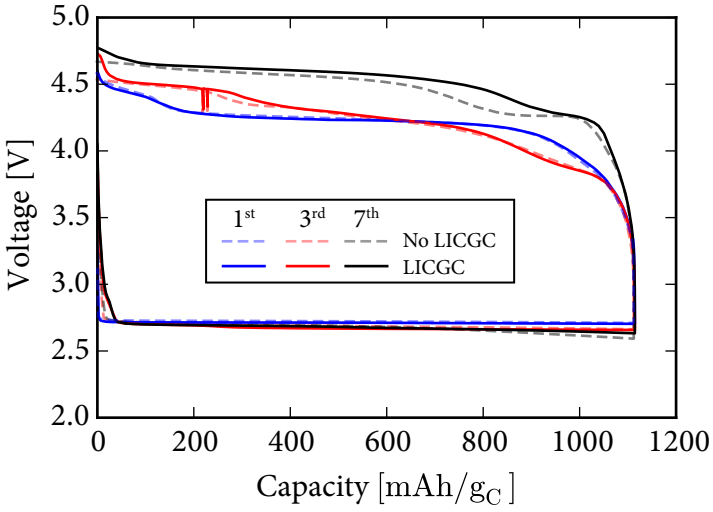

Figure B.10: Voltage curves of cells with and without a LICGC barrier.

Figure B.11: Separators for a cell with a LiI redox mediator and a LICGC barrier after 21 cycles.

BIBLIOGRAPHY

[1] Solomon, S.; Plattner, G.-K.; Knutti, R.; Friedlingstein, P. *Proceedings of the National Academy of Sciences* **2009**, *106*, 1704–1709.

[2] U.S. Energy Information Administration, *Primary Energy Consumption by Source and Sector*; 2012.

[3] IEA, *World Energy Outlook 2014*; World Energy Outlook; IEA, 2014.

[4] Whittingham, M. S. *Chemical Reviews* **2004**, *104*, 4271–4301.

[5] Etacheri, V.; Marom, R.; Elazari, R.; Salitra, G.; Aurbach, D. *Energy & Environmental Science* **2011**, *4*, 3243–3262.

[6] Totten, G. E., Westbrook, S. R., Shah, R. J., Eds. *Fuels and Lubricants Handbook: Technology, Properties, Performance, and Testing*; ASTM International, 2003.

[7] United States Environmental Protection Agency, Fueleconomy.gov. 2016; `http://www.fueleconomy.gov`.

[8] Kodjak, D. Consumer Acceptance of Electric Vehicles in the US. 2012.

[9] Liu, M.; Rong, Z.; Malik, R.; Canepa, P.; Jain, A.; Ceder, G.; Persson, K. A. *Energy & Environmental Science* **2015**, *8*, 964–974.

[10] Duracell, *Zinc–air Technical Bulletin*; 2004.

[11] Sun, Q.; Yang, Y.; Fu, Z.-W. *Electrochemistry Communications* **2012**, *16*, 22–25.

[12] Nazar, L. F.; Cuisinier, M.; Pang, Q. *MRS Bulletin* **2014**, *39*, 436–442.

[13] Abraham, K. M. *Journal of The Electrochemical Society* **1996**, *143*, 1.

[14] Chan, C. C. *Proceedings of the IEEE* **2007**, *95*, 704–718.

[15] USDOE Office of Energy Efficiency and Renewable Energy (EERE), *Improving Motor and Drive System Performance – A Sourcebook for Industry*; 2014.

[16] Thomas, J. *SAE International Journal of Passenger Cars - Mechanical Systems* **2014**, *7*, 1374–1384.

[17] Kowalczk, I.; Read, J.; Salomon, M. *Pure and Applied Chemistry* **2007**, *79*, 851–860.

[18] Hummelshøj, J. S.; Blomqvist, J.; Datta, S.; Vegge, T.; Rossmeisl, J.; Thygesen, K. S.; Luntz, a. C.; Jacobsen, K. W.; Nørskov, J. K. *The Journal of chemical physics* **2010**, *132*, 071101.

[19] Aurbach, D.; Daroux, M.; Faguy, P.; Yeager, E. *Journal of Electroanalytical Chemistry and Interfacial Electrochemistry* **1991**, *297*, 225–244.

[20] Peng, Z.; Freunberger, S. a.; Hardwick, L. J.; Chen, Y.; Giordani, V.; Bardé, F.; Novák, P.; Graham, D.; Tarascon, J.-M.; Bruce, P. G. *Angewandte Chemie (International ed. in English)* **2011**, *50*, 6351–5.

[21] Aurbach, D.; Zinigrad, E.; Cohen, Y.; Teller, H. *Solid State Ionics* **2002**, *148*, 405–416.

[22] Younesi, R.; Hahlin, M.; Roberts, M.; Edström, K. *Journal of Power Sources* **2012**,

[23] Xu, W.; Xu, K.; Viswanathan, V. V.; Towne, S. a.; Hardy, J. S.; Xiao, J.; Nie, Z.; Hu, D.; Wang, D.; Zhang, J. G. *Journal of Power Sources* **2011**, *196*, 9631–9639.

[24] Mccloskey, B. D.; Bethune, D. S.; Shelby, R. M.; Mori, T.; Scheffler, R.; Speidel, A.; Sherwood, M.; Luntz, A. C. *The Journal of Physical Chemistry Letters* **2012**, *3*, 3043–3047.

[25] Freunberger, S. a.; Chen, Y.; Peng, Z.; Griffin, J. M.; Hardwick, L. J.; Bardé, F.; Novák, P.; Bruce, P. G. *Journal of the American Chemical Society* **2011**, *133*, 8040–7.

[26] Laino, T.; Curioni, A. *Chemistry (Weinheim an der Bergstrasse, Germany)* **2012**, 3510–3520.

[27] Itkis, D. M.; Semenenko, D. A.; Kataev, E. Y.; Belova, A. I.; Neudachina, V. S.; Sirotina, A. P.; Hävecker, M.; Teschner, D.; Knop-gericke, A.; Dudin, P.; Barinov, A.; Goodilin, E. A.; Shao-Horn, Y.; Yashina, L. V.; Ha, M. *Nano Letters* **2013**, *13*, 4697–4701.

[28] Black, R.; Oh, S. H.; Lee, J.-H.; Yim, T.; Adams, B.; Nazar, L. F. *Journal of the American Chemical Society* **2012**, *134*, 2902–2905.

[29] Débart, A.; Paterson, A. J.; Bao, J.; Bruce, P. G. *Angewandte Chemie (International ed. in English)* **2008**, *47*, 4521–4524.

[30] Débart, A.; Bao, J.; Armstrong, G.; Bruce, P. G. *Journal of Power Sources* **2007**, *174*, 1177–1182.

[31] Lu, Y.-C.; Gasteiger, H. a.; Parent, M. C.; Chiloyan, V.; Shao-Horn, Y. *Electrochemical and Solid-State Letters* **2010**, *13*, A69.

[32] Lu, Y.-C.; Gasteiger, H. a.; Crumlin, E.; McGuire, R.; Shao-Horn, Y. *Journal of The Electrochemical Society* **2010**, *157*, A1016.

[33] Lu, Y.-C.; Xu, Z.; Gasteiger, H. a.; Chen, S.; Hamad-Schifferli, K.; Shao-Horn, Y. *Journal of the American Chemical Society* **2010**, *132*, 12170–1.

[34] McCloskey, B. D.; Scheffler, R.; Speidel, A.; Bethune, D. S.; Shelby, R. M.; Luntz, a. C. *Journal of the American Chemical Society* **2011**, *133*, 18038–41.

[35] Lim, H.-D.; Park, K.-Y.; Gwon, H.; Hong, J.; Kim, H.; Kang, K. *Chemical Communications* **2012**, *48*, 8374–8376.

[36] Mizuno, F.; Nakanishi, S.; Kotani, Y.; Yokoishi, S.; Iba, H. *Electrochemistry* **2010**, *78*, 403–405.

[37] Jung, H.-G.; Hassoun, J.; Park, J.-B.; Sun, Y.-K.; Scrosati, B. *Nature chemistry* **2012**, *4*, 579–85.

[38] Sun, B.; Munroe, P.; Wang, G. *Scientific reports* **2013**, *3*, 2247.

[39] Zhang, T.; Zhou, H. *Nature Communications* **2013**, *4*, 1817.

[40] Read, J. *Journal of The Electrochemical Society* **2002**, *149*, A1190–A1195.

[41] Sandhu, S.; Fellner, J.; Brutchen, G. *Journal of Power Sources* **2007**, *164*, 365–371.

[42] Viswanathan, V.; Thygesen, K. S.; Hummelshøj, J. S.; Nørskov, J. K.; Girishkumar, G.; McCloskey, B. D.; Luntz, a. C. *The Journal of chemical physics* **2011**, *135*, 214704.

[43] Albertus, P.; Girishkumar, G.; McCloskey, B.; Sanchez-Carrera, R. S.; Kozinsky, B.; Christensen, J.; Luntz, a. C. *Journal of The Electrochemical Society* **2011**, *158*, A343.

[44] Read, J.; Mutolo, K.; Ervin, M.; Behl, W.; Wolfenstine, J.; Driedger, A.; Foster, D. *Journal of The Electrochemical Society* **2003**, *150*, A1351.

[45] Sahapatsombut, U.; Cheng, H.; Scott, K. *Journal of Power Sources* **2013**, *227*, 243–253.

[46] Nimon, V. Y.; Visco, S. J.; De Jonghe, L. C.; Volfkovich, Y. M.; Bograchev, D. a. *ECS Electrochemistry Letters* **2013**, *2*, A33–A35.

[47] Yu, M.; Ren, X.; Ma, L.; Wu, Y. *Nature Communications* **2014**, *5*, 5111.

[48] Balasubramanian, P.; Marinaro, M.; Theil, S.; Wohlfahrt-Mehrens, M.; Jörissen, L. *Journal of Power Sources* **2015**, *278*, 156–162.

[49] Laoire, C. O.; Mukerjee, S.; Abraham, K. M.; Plichta, E. J.; Hendrickson, M. a. *The Journal of Physical Chemistry C* **2010**, *114*, 9178–9186.

[50] Adams, B. D.; Radtke, C.; Black, R.; Trudeau, M. L.; Zaghib, K.; Nazar, L. F. *Energy & Environmental Science* **2013**, *6*, 1772.

[51] Chervin, C. N.; Wattendorf, M. J.; Long, J. W.; Kucko, N. W.; Rolison, D. R. *Journal of the Electrochemical Society* **2013**, *160*, A1510–A1516.

[52] Lau, S.; Archer, L. A. *Nano Letters* **2015**, *15*, 5995–6002.

[53] Read, J. *Journal of The Electrochemical Society* **2006**, *153*, A96.

[54] Zhang, S. S.; Foster, D.; Read, J. *Journal of Power Sources* **2010**, *195*, 1235–1240.

[55] Yang, X.-h.; He, P.; Xia, Y.-y. *Electrochemistry Communications* **2009**, *11*, 1127–1130.

[56] Tran, C.; Yang, X.-Q.; Qu, D. *Journal of Power Sources* **2010**, *195*, 2057–2063.

[57] Mitchell, R. R.; Gallant, B. M.; Thompson, C. V.; Shao-Horn, Y. *Energy & Environmental Science* **2011**, *4*, 2952–2958.

[58] Xiao, J.; Mei, D.; Li, X.; Xu, W.; Wang, D.; Graff, G. L.; Bennett, W. D.; Nie, Z.; Saraf, L. V.; Aksay, I. a.; Liu, J.; Zhang, J.-G. *Nano Letters* **2011**, *11*, 5071–8.

[59] Mehta, M.; Bevara, V.; Andrei, P.; Zheng, J. Limitations and Potential Li-Air Batteries: a Simulation Prediction. The International Conference on Simulation of Semiconductor Processes and Devices. 2012; pp 241–244.

[60] Radin, M.; Rodriguez, J. Lithium Peroxide Surfaces and Point Defects: Relevance for Li-air Batteries. Proceedings of the Battery Congress. 2011; pp 6–12.

[61] Radin, M. D.; Rodriguez, J. F.; Tian, F.; Siegel, D. J. *Journal of the American Chemical Society* **2012**, *134*, 1093–103.

[62] Radin, M. D.; Siegel, D. J. *Energy & Environmental Science* **2013**, *6*, 2370.

[63] Haynes, W. M. *CRC handbook of chemistry and physics : a ready-reference book of chemical and physical data.*; 2015.

[64] Luntz, A. C.; Viswanathan, V.; Voss, J.; Varley, J. B.; Nørskov, J. K.; Scheffler, R.; Speidel, A. *The Journal of Physical Chemistry Letters* **2013**, *4*, 3494–3499.

[65] Zhang, Y.; Zhang, H.; Li, J.; Wang, M.; Nie, H.; Zhang, F. *Journal of Power Sources* **2013**, *240*, 390–396.

[66] Hossain, M.; Tryk, D.; Yeager, E. *Electrochimica acta* **1989**, 1733–1737.

[67] Lu, J.; Lei, Y.; Lau, K. C.; Luo, X.; Du, P.; Wen, J.; Assary, R. S.; Das, U.; Miller, D. J.; Elam, J. W.; Albishri, H. M.; El-Hady, D. A.; Sun, Y.-K.; Curtiss, L. a.; Amine, K. *Nature Communications* **2013**, *4*, 2383.

[68] Varley, J. B.; Viswanathan, V.; Nørskov, J. K.; Luntz, a. C. *Energy & Environmental Science* **2014**, *7*, 720–727.

[69] Johnson, L.; Li, C.; Liu, Z.; Chen, Y.; Freunberger, S. A.; Ashok, P. C.; Praveen, B. B.; Dholakia, K.; Tarascon, J.-M.; Bruce, P. G. *Nature Chemistry* **2014**, *6*, 1091–1099.

[70] Das, S. K.; Xu, S.; Emwas, A.-H.; Lu, Y. Y.; Srivastava, S.; Archer, L. a. *Energy & Environmental Science* **2012**, *5*, 8927.

[71] Meini, S.; Piana, M.; Tsiouvaras, N.; Garsuch, A.; Gasteiger, H. a. *Electrochemical and Solid-State Letters* **2012**, *15*, A45.

[72] Aetukuri, N. B.; McCloskey, B. D.; García, J. M.; Krupp, L. E.; Viswanathan, V.; Luntz, A. C. *Nature Chemistry* **2014**, *7*, 50–56.

[73] Lim, H. H.-D. H. H.-K.; Park, K.-Y.; Seo, D.-H.; Gwon, H.; Hong, J.; Goddard, W. A.; Kim, H.; Kang, K. *Journal of the American Chemical Society* **2013**, *135*, 9733–9742.

[74] Horstmann, B.; Gallant, B.; Mitchell, R.; Bessler, W. G.; Shao-Horn, Y.; Bazant, M. Z. *The Journal of Physical Chemistry Letters* **2013**, *4*, 4217–4222.

[75] Milchev, A.; Stoyanov, S.; Kaischev, R. *Thin Solid Films* **1974**, *22*, 255–265.

[76] Herranz, J.; Garsuch, A.; Gasteiger, H. a. *The Journal of Physical Chemistry C* **2012**, *116*, 19084–19094.

[77] Kolmogoroff, A. *Izv. Akad. Nauk SSSR Ser. Mat.* **1937**, *1*, 355–359.

[78] Miiller, S. *Journal of New Materials for Electrochemical Systems* **1999**, *232*, 227–232.

[79] TIMCAL Ltd, Carbon Additives for Advanced Lead Acid Batteries. 2013.

[80] Lu, J. et al. *Nature Communications* **2014**, *5*, 4895.

[81] Xia, C.; Waletzko, M.; Peppler, K.; Janek, J. *The Journal of Physical Chemistry C* **2013**, *117*, 19897–19904.

[82] Liu, W.-M.; Gao, T.-T.; Yang, Y.; Sun, Q.; Fu, Z.-W. *Physical Chemistry Chemical Physics* **2013**, 15806–15810.

[83] Cao, Y.; Wei, Z.; He, J.; Zang, J.; Zhang, Q.; Zheng, M.; Dong, Q. *Energy & Environmental Science* **2012**, *5*, 9765–9768.

[84] Sun, B.; Zhang, J.; Munroe, P.; Ahn, H.-J.; Wang, G. *Electrochemistry Communications* **2013**, *31*, 88–91.

[85] Tran, C.; Kafle, J.; Yang, X.-q.; Qu, D. *Carbon* **2010**, *49*, 1266–1271.

[86] Chen, Y.; Freunberger, S. A. S.; Peng, Z.; Fontaine, O.; Bruce, P. G. *Nature Chemistry* **2013**, *5*, 489–494.

[87] Lim, H.-D.; Song, H.; Kim, J.; Gwon, H.; Bae, Y.; Park, K.-Y.; Hong, J.; Kim, H.; Kim, T.; Kim, Y. H.; Lepró, X.; Ovalle-Robles, R.; Baughman, R. H.; Kang, K. *Angewandte Chemie (International ed. in English)* **2014**, 3926–3931.

[88] Tan, P.; Shyy, W.; Zhao, T.; Wei, Z.; An, L. *Journal of Power Sources* **2015**, *278*, 133–140.

[89] Freunberger, S. a.; Chen, Y.; Drewett, N. E.; Hardwick, L. J.; Bardé, F.; Bruce, P. G. *Angewandte Chemie (International ed. in English)* **2011**, *50*, 8609–13.

[90] Henderson, W. a.; Brooks, N. R.; Brennessel, W. W.; Young, V. G. *Chemistry of Materials* **2003**, *15*, 4679–4684.

[91] Shimizu, K.; Freitas, A. A.; Atkin, R.; Warr, G. G.; FitzGerald, P. A.; Doi, H.; Saito, S.; Ueno, K.; Umebayashi, Y.; Watanabe, M.; Canongia Lopes, J. N. *Physical Chemistry Chemical Physics* **2015**, *17*, 22321–22335.

[92] Plimpton, S. *Journal of Computational Physics* **1995**, *117*, 1–19.

[93] Hanwell, M. D.; Curtis, D. E.; Lonie, D. C.; Vandermeersch, T.; Zurek, E.; Hutchison, G. R. *Journal of Cheminformatics* **2012**, *4*, 17.

[94] Martínez, L.; Andrade, R.; Birgin, E. G.; Martínez, J. M. *Journal of Computational Chemistry* **2009**, *30*, 2157–2164.

[95] Popov, A. M.; Lebedeva, I. V.; Knizhnik, A. A.; Lozovik, Y. E.; Potapkin, B. V. *Chemical Physics Letters* **2012**, *536*, 82–86.

[96] Creighton, J. A.; Lippincott, E. R. *The Journal of Chemical Physics* **1964**, *40*, 1779.

[97] Profeta, G.; Calandra, M.; Mauri, F. *Nature Physics* **2012**, *8*, 131–134.

[98] Flyvbjerg, H.; Petersen, H. G. *The Journal of Chemical Physics* **1989**, *91*, 461.

[99] Khetan, A.; Luntz, A.; Viswanathan, V. *The Journal of Physical Chemistry Letters* **2015**, 1254–1259.

[100] Ding, N.; Chien, S. W.; Hor, T. S. A.; Lum, R.; Zong, Y.; Liu, Z. L. *Journal of Materials Chemistry A* **2014**, *2*, 12433–12441.

[101] Younesi, R.; Singh, N.; Urbonaite, S.; Edström, K.; Transactions, E. C. S.; Society, T. E. *ECS Transactions* **2010**, *25*, 121–127.

[102] Showa Denko K.K., *Vapor Grown Carbon Fiber*; 2012.

[103] Imerys Graphite & Carbon, *Specialty Carbons for the Positive Electrode of Lithium-Ion Batteries*; 2014.

[104] Laoire, C. O.; Mukerjee, S.; Abraham, K. M.; Plichta, E. J.; Hendrickson, M. A. *Journal of Physical Chemistry C* **2009**, *113*, 20127–20134.

[105] Andrews, L. *The Journal of Chemical Physics* **1969**, *50*, 4288.

[106] Andrews, L.; Smardzewski, R. R. *The Journal of Chemical Physics* **1973**, *58*, 2258–2261.

[107] Burke, C. M.; Pande, V.; Khetan, A.; Viswanathan, V.; McCloskey, B. D. *Proceedings of the National Academy of Sciences* **2015**, *112*, 201505728.

[108] United States Environmental Protection Agency, *Application of Life-Cycle Assessment to Nanoscale Technology: Lithium-ion Batteries for Electric Vehicles*; 2013.

[109] A123 Systems, *Nanophosphate Basics: An Overview of the Structure , Properties and Benefits of A123 Systems' Proprietary Lithium Ion Battery Technology*; 2013.

[110] Peng, Z.; Freunberger, S. a.; Chen, Y.; Bruce, P. G. *Science (New York, N.Y.)* **2012**, *337*, 563–6.

[111] Zhu, X.; Zhao, T. S.; Wei, Z.; Tan, P.; An, L. *Energy & Environmental Science* **2015**,

[112] Landa-Medrano, I.; Pinedo, R.; Ortiz-Vitoriano, N.; de Larramendi, I. R.; Rojo, T. *ChemSusChem* **2015**,

[113] Ottakam Thotiyl, M. M.; Freunberger, S. a.; Peng, Z.; Chen, Y.; Liu, Z.; Bruce, P. G. *Nature materials* **2013**, *12*, 1050–6.

[114] Li, F.; Tang, D. M.; Chen, Y.; Golberg, D.; Kitaura, H.; Zhang, T.; Yamada, A.; Zhou, H. *Nano Letters* **2013**, *13*, 4702–4707.

[115] Peng, Z.; Freunberger, S. A.; Chen, Y.; Bruce, P. G. *Science* **2012**,

[116] Liao, K.; Wang, X.; Sun, Y.; Tang, D.; Han, M.; He, P. *Energy & Environmental Science* **2015**, *8*, 1992–1997.

[117] McCloskey, B. D. B.; Valery, A.; Luntz, A. C.; Gowda, S. R.; Wallraff, G. M.; Garcia, J. M.; Mori, T.; Krupp, L. E. *The Journal of Physical Chemistry Letters* **2013**, *4*, 2989–2993.

[118] Ottakam Thotiyl, M. M.; Freunberger, S. a.; Peng, Z.; Bruce, P. G. *Journal of the American Chemical Society* **2013**, *135*, 494–500.

[119] Nie, A.; Gan, L. Y.; Cheng, Y.; Asayesh-Ardakani, H.; Li, Q.; Dong, C.; Tao, R.; Mashayek, F.; Wang, H. T.; Schwingenschlögl, U.; Klie, R. F.; Yassar, R. S. *ACS Nano* **2013**, *7*, 6203–6211.

[120] Trasatti, S.; Petrii, O. A. *Journal of Electroanalytical Chemistry* **1992**, *327*, 353–376.

[121] Hu, N.; Itoi, T.; Akagi, T.; Kojima, T.; Xue, J.; Yan, C.; Atobe, S.; Fukunaga, H.; Yuan, W.; Ning, H.; Surina,; Liu, Y.; Alamusi, *Carbon* **2013**, *51*, 202–212.

[122] Nanni, F.; Ruscito, G.; Puglia, D.; Terenzi, A.; Kenny, J. M.; Gusmano, G. *Composites Science and Technology* **2011**, *71*, 1–8.

[123] Højberg, J.; McCloskey, B. D.; Hjelm, J.; Vegge, T.; Johansen, K.; Norby, P.; Luntz, A. C. *ACS Applied Materials & Interfaces* **2015**, *7*, 4039–4047.

[124] Hirschorn, B.; Orazem, M. E.; Tribollet, B.; Vivier, V.; Frateur, I.; Musiani, M. *Electrochimica Acta* **2010**, *55*, 6218–6227.

[125] Adams, J.; Karulkar, M.; Anandan, V. *Journal of Power Sources* **2013**, *239*, 132–143.

[126] Landa-Medrano, I.; Ruiz De Larramendi, I.; Ortiz-Vitoriano, N.; Pinedo, R.; Ignacio Ruiz De Larramendi, J.; Rojo, T. *Journal of Power Sources* **2014**, *249*, 110–117.

[127] Zoltowski, P. *Journal of Electroanalytical Chemistry* **1998**, *443*, 149–154.

[128] Barbieri, O.; Hahn, M.; Herzog, a.; Kötz, R. *Carbon* **2005**, *43*, 1303–1310.

[129] Zhong, L.; Mitchell, R. R.; Liu, Y.; Gallant, B. M.; Thompson, C. V.; Huang, J. Y.; Mao, S. X.; Shao-Horn, Y. *Nano Letters* **2013**, *13*, 2209–14.

[130] Hase, Y.; Ito, E.; Shiga, T.; Mizuno, F.; Nishikoori, H.; Iba, H.; Takechi, K. *Chemical communications (Cambridge, England)* **2013**, 3–5.

[131] Bergner, B. J.; Schürmann, A.; Peppler, K.; Garsuch, A.; Janek, J. *Journal of the American Chemical Society* **2014**, *136*, 15054–15064.

[132] Uddin, J.; Bryantsev, V. S. V.; Giordani, V.; Walker, W.; Chase, G. V.; Addison, D. *The Journal of Physical Chemistry Letters* **2013**, *4*, 3760–3765.

[133] Boschloo, G.; Hagfeldt, A.; Spectus, C. O. N. *Accounts of Chemical Research* **2009**, *42*, 1819–1826.

[134] Jin, Z.; Xie, K.; Hong, X.; Hu, Z.; Liu, X. *Journal of Power Sources* **2012**, *218*, 163–167.

[135] Tang, Q.; Shan, Z.; Wang, L.; Qin, X.; Zhu, K.; Tian, J.; Liu, X. *Journal of Power Sources* **2014**, *246*, 253–259.

[136] Bauer, I.; Thieme, S.; Brückner, J.; Althues, H.; Kaskel, S. *Journal of Power Sources* **2014**, *251*, 417–422.

[137] Yu, X.; Joseph, J.; Manthiram, A. *Journal of Materials Chemistry A* **2015**, *00*, 1–9.

[138] OHARA Corporation, *Lithium-Ion Conducting Gass-Ceramic (LIC-GC)*; pp 1–2.

[139] Shakhashiri, B. Z. Chemical demonstrations. 1992.

[140] Oh, S. H.; Black, R.; Pomerantseva, E.; Lee, J.-H.; Nazar, L. F. *Nature Chemistry* **2012**, *4*, 1004–1010.

[141] Ren, X.; Lau, K. C.; Yu, M.; Bi, X.; Kreidler, E.; Curtiss, L. A.; Wu, Y. *ACS Applied Materials & Interfaces* **2014**,

[142] Kwak, W.-J.; Hirshberg, D.; Sharon, D.; Shin, H.-J.; Afri, M.; Park, J.-B.; Garsuch, A.; Chesneau, F. F.; Frimer, A. a.; Aurbach, D.; Sun, Y.-K. *J. Mater. Chem. A* **2015**, *3*, 8855–8864.

[143] Liu, T.; Leskes, M.; Yu, W.; Moore, A. J.; Zhou, L.; Bayley, P. M.; Kim, G.; Grey, C. P. *Science* **2015**, *350*, 530–533.